Photothermal effects, Optomechanics and Optical Levitation

Chenyue Gu

A thesis submitted for the degree of
Master of Philosophy in Physics
The Australian National University

November, 2022

Declaration

This thesis is an account of research undertaken between July 2021 and October 2022 at The Centre for Quantum Computation and Communication Technology (CQC^2T), in the Department of Quantum Science, Research School of Physics, The Australian National University, Canberra, Australia.

The research presented here was supervised at all stages by Prof. Ping Koy Lam, Dr. Jiayi Qin and Dr. Giovanni Guccione. Except where acknowledged in the customary manner, the material presented in this thesis is, to the best of my knowledge, original and has not been submitted in whole or part for a degree in any university.

Chenyue Gu

November, 2022

Acknowledgements

The past two years has been a very special experience to me. To study the amazing levitation cavity, to explore a new field of physics, and to know so many people who have passion for research, hunger for truth and entire devotion to science have enlightened me in so many moments when I feel perplexed.

Here, I give my special thanks to the best supervisors Prof. Ping Koy Lam, Dr. Jiayi Qin, and Dr. Giovanni Guccione, who provided all the guidance and help that I needed during the time when I was stuck in China and the time I spent in Australia. Ping Koy, without your support, I would never get the exemption from the travel restriction so early during the pandemic and successfully entered Australia to start my Master's. You were always able to inspire me when I could not see the way. You have provided as much as opportunities and guidance to me not only during my Master's but also during my PhD application. Jiayi, you always gave me in-time help and valuable suggestions in research and in life. Especially during the first year when I was entirely new to the project and couldn't do work in person, you were always patient with my questions and helped me relieve my anxiety during the "endless" online meetings. Giovanni, as your student, I was always impressed by how quickly you could understand my questions and confusions and how clearly you could explain the physical concepts to me. I will always remember the time you spent in the laboratory with me, teaching me how to work on optics and electronics from scratch. I am also thankful for your detailed and fun comments on my paper and thesis that made me laugh hard so many times during the stressful time of writing. As a friend, I appreciated the moments with you outside campus, especially my very first "meeting" with kangaroos and koalas.

I would like to extend my sincere gratitude to Amanda Haines and Siobhan Ryman, who were always willing to offer help when I needed it. Amanda, I could not imagine how much time I would have wasted on the tedious paperwork and documents without your help. I am also grateful for being included in the body balance organized by you, which has built up another connection between me and the group during my remote-working time in China. Siobhan, I appreciate all the guidance and suggestions that you have provided about my enrollment, the exemption of travel restrictions, and my graduation.

Many thanks also go to the full quantum optics group, for the time we spent together inside and outside the office. I am grateful for the help from Ruvi and Jinyong in my research. I will always treasure the weekends that I spent with Aaron, biking, bouldering, and hanging out with his lovely wife Meg, cute dog Luna and now "yummy" baby Mayuka. I have also enjoyed the office time with Ida and Angela, who had to "tolerate" my noise

but were always very friendly to me. I would also like to thank Lorcan who has proofread almost my entire thesis and has "wasted" lots of time on Rubik's cube with me, Biveen who has taken me around and shown me many good restaurants, Ozlem who has kept me company for coffee, Mikhael who walked me to McDonald's at midnight so many times, Anthony who "saved" my life in Tasmania. I would also like to express my gratitude to Ben, Assad, Oliver, Hao, who have helped me during my Master's. Moreover, I wish to express my appreciation for every sunset in this beautiful land, which was always able to cure my sadness and depression.

Most importantly, I would like to give my special thanks to my family who have always stood by my side and supported my choices. Without their support and love, I could not have reached the place I am and be the person I wish to be.

Abstract

The invention of lasers enabled strong and controllable interactions between light and small objects. Radiation pressure provides a unique tool for optomechanical control and manipulation of the quantum states of a mechanical oscillator. The high power density and photon flux of laser radiation lead to extremely high heating rates at surfaces, which induces measurement noise and is hence considered harmful in sensing systems. Optomechanical interaction can also be mediated by photothermal effects which, although frequently overlooked, may compete with radiation pressure interaction. A complete understanding of how these phenomena affect the coherent exchange of information between optical and mechanical degrees of freedom is yet undeveloped, particularly in mesoscale high-power systems where photothermal effects can fully dominate the interaction.

Here we investigate the photothermal effects in a unique optomechanical system: a cavity-enhanced setup for macroscopic optical levitation, where a free-standing mirror acts as the optomechanical oscillator. In this system, we observe the photothermally induced instability when the optical cavity is driven by a high-power laser. We show that the possible thermally induced parametric gain can be reduced and even cancelled out experimentally, by inserting windows into the optomechanical cavity to modify the photothermal properties of the system.

Theoretically, we report an effective model that can predict and successfully reconstruct the dynamics of this system. By decomposing the photothermal interaction into two opposing light-induced effects, photothermal expansion and thermo-optic effects, we reconstruct a heuristic model. It is based on the mutual interaction between the intracavity field and four position degrees of freedom, which offers refined predictions that provide a high agreement with the experimental results. We also provide a detailed discussion on the effectiveness of different models, and have concluded that two photothermal effects are necessary in the model for simulating the dynamics of the optomechanical levitation system studied.

Overall, the experimental and theoretical investigations presented in this thesis set essential groundwork for the characterisation and stabilisation of existing systems and provide a deeper understanding of photothermal effects in optomechanical systems. The methods that used in the investigation and cancellation of photothermal effects in this system can be easily applied to other similar optomechanical systems where high-intensity laser is used or high precision of the measurement is desired. This work facilitates the development of new and more precise optomechanical systems for integrated photonics and sensing, and also paves the way to fundamental studies in quantum mechanics.

Contents

Chapter 1

Introduction

Light, carrying momentum, produces radiation pressure force [1], which was predicted by Maxwell in 1873 [2] and was first demonstrated using a light mill configuration in 1901 [3, 4]. The capability of radiation pressure strongly affecting the dynamics of neutral particles has generated considerable interest since then, giving rise to the potential of making lasers a useful laboratory tool to move matter. Techniques using lasers have been developed to trap small particles [5, 6], cool them [7, 8, 9, 10], levitate them against gravity, manipulate them, and use them as sensitive probes for measurements. They have proved their practicality in experiments measuring optical, electric [11], magnetic, radiometric [12, 13], viscous drag [13], and gravitational forces, and have found applications in a wide variety of subjects where small particles play a role.

1.1 Optical levitation

Two key properties of lasers are their high degree of spatial coherence and spectral purity. The spatial coherence of lasers give rise to high optical intensity, which allows the radiation pressure to be concentrated on a single "point", resulting in large radiation forces. By imagining a laser beam focused to a spot size of about its wavelength, one can easily picture how large a force a laser produces. With a power of about 1 W, a laser beam can subject a transparent dielectric sphere with a diameter of 1 µm to an intensity on the order of 10^8 W cm^{-2}. Assuming the light is reflected from the sphere with an average reflectivity of only 10%, the sphere can achieve an acceleration of approximately $10^6 g$, where g is the acceleration of gravity [14].

The high spectral purity, that allows lasers to strongly interact with narrow atomic resonance lines, plays a rather important role for large forces to be exerted on atoms, which further leads to optically cooling and trapping neutral atoms. When absorbing or emitting one photon, the movement of an atom can be significantly affected by the momentum generated from the radiation, which allows velocity change of a few centimeters per second of the atom. Under strong excitation, an atom with a spontaneous emission lifetime of $\sim 10^{-8}$ s can absorb and spontaneously emit a maximum of $\sim 10^8$ photons per second. With resonant light, the absorption cross-section of atoms is very large and thus

requires an intensity of only about $10^{-2}\,\mathrm{W\,cm^{-1}}$ to achieve the saturation condition, i.e. that the maximum number of photons are absorbed or emitted [11].

Another feature of focused lasers is the existence of high-intensity gradients, which provides large gradient forces that make stable optical trapping and manipulation of particles possible. Experiments using lasers to levitate and trap microscopic particles were pioneered by Arthur Ashkin in the 1970s [15]. Stable optical trapping of individual particles was first observed with spheres in liquid using a pair of horizontally opposing focused beams, where viscosity is high and gravity plays a minor role. Particles that drifted near either beam were drawn in, accelerated to and stopped at the equilibrium point. When one beam was blocked, the spheres were driven by the light force produced by the other laser beam and were guided along the beam. This gave the first demonstration of radiation trapping.

In air and vacuum, stable levitation of small transparent glass spheres with a vertically directed laser beam was demonstrated experimentally soon afterwards [16]. The spheres were lifted and trapped to an equilibrium position where the radiation pressure balanced gravity. Moreover, the spheres could easily be moved anywhere by simply moving the beam. Later experiments showed that not only single spheres, but a dozen spheres, as well as charged and neutral liquid drops, could also be captured in a single vertical beam [17]. The levitated drops arranged themselves in order of size as an array, each of which was trapped at a local intensity maximum in the optical diffraction pattern of all particles located below it. The ability to manipulate and sensitively observe individual micro-sized liquid drops makes optical levitation a promising approach in cloud physics [18] and aerosol science [19]. Compared to other techniques in these fields, the advantages of optical levitation result from its depth of the optical trap, highly localised nature, and ease of moving particles with the beams in space.

Except for the characteristics of simple manipulation, easy observation, and high positional stability, other peculiarities of optical levitation were found in the following years. The advantages of the high acceleration and force sensitivity as well as the capability of isolation from the environment give rise to the applications in light scattering [20], atomic and molecular physics [21, 22], planetary physics [23], isotope separation [24], high-resolution spectroscopy [25, 11], and, last but not least, quantum optics [26, 27], which is the main point of interest for the system here presented.

1.2 Photothermal effects

Another property of laser radiation is the high power density and photon flux, which leads to the realisation of extremely high heating rates at surfaces, giving rise to a great interest in the research of dynamics of surface processes caused by optical or thermal excitation. Three laser-surface interactions are mainly discussed in general: photochemical effects which usually lead to laser-induced desorption and ablation, photoacoustic effects that

affect surface acoustic waves and hence thermal diffusion in the materials, and photothermal effects resulting in transient and localised heating processes as expansion, density gradients, and geometrical changes of the surface shape.

Among all the laser-surface interactions, photothermal effects have been a topic of fascination in last few decades, especially in the studies of the properties of thin films and the noise introduced into Fabry-Pérot cavities and interferometers. With exposure to any form of radiation, local heating can be caused on a sample via absorption and subsequent thermalisation of energy [28]. In spectroscopy of thin films, photothermal analysis plays an exceedingly important role [29]. It is advantageous due to its contactless generation of a well-defined heat source at the surface, the purer detected signal that only comes from the energy absorbed in the sample, and the real-time detection of transient temperatures with high-time resolution schemes. These make photothermal analysis a good candidate for studying the thermal and temperature dependent physical properties of samples, as phase transitions and charge distributions [30].

Photothermal imaging is an emerging topic, providing a powerful tool in different imaging systems, such as ultrasonic imaging of thin films, imaging of molecules in living cells [31], and chemical imaging of small crystals and polymer coating on microelectromechanical systems [32]. In some recent publications, photothermal effects have also been proposed as a control and stabilisation tool [33] as well as as a dissipation engineering tool [34].

However, photothermal effects in optical systems, where optical absorption often causes thermal expansion and refractive index changes and induces noise into the systems, are considered harmful. It was observed in the Laser Interferometer Gravitational-Wave Observatory (LIGO) system that thermal effects in the test-masses cause optical wavefront distortion from thermal lensing [35] and surface deformation [36], which deteriorate control signals and decrease interferometer sensitivity. These effects are induced by the high operating laser powers that are required for the detection of gravitational waves from high-frequency emitters, of which a small amount of light absorbed by the test masses' dielectric coatings are converted into heat and then diffused through the mirror. [37, 38, 39]. The development of new and more extreme cavity photomechanical systems at various scales, with increased optical densities and reduced mechanical oscillator sizes, has brought increasing attention to photothermal effects because they are no longer negligible in such systems.

1.3 Motivation

This thesis investigates the photothermal effects in an optomechanics-based optical levitation setup, where a free-standing mirror is acting as one of the end mirrors of an optical cavity, which is expected to be optically lifted by the radiation pressure force exerted by the optical field inside the cavity. The mirror behaves as an oscillator whose large

mass and high density provide high inertial sensitivity to the system, which results in lower tolerance to noise and other optically induced effects. Photothermal effects mediate exchanges between optical and mechanical degrees of freedom, and in doing so they compete with — and can even dominate over — radiation pressure force. In the presence of parasitic mechanical modes, photothermal interaction causes parametric instabilities that inevitably affect the performance of the instrument.

In this system, we observe the photothermally induced instability when the optical cavity is driven by a high-power laser, where the realisation of a stable levitation is unattainable and the existing model for the dynamics of the system becomes less reliable [40]. In this work, we show that the possible thermally induced parametric gain can be reduced and even cancelled out with a modification to the photothermal properties of an optomechanical cavity experimentally. By inserting windows into the cavity, we switch the sign of photothermal interaction, allowing cooperation with the radiation pressure, and then achieve control of the system's dynamics to be fully balanced to its equilibrium point. This passive stabilisation technique can be adapted and used in other macroscopic and high-power optomechanical systems that are particularly susceptible to parasitic photothermal effects, revealing its particular advantage in optical control and precise metrological applications, which also paves a way to quantum optomechanics.

Moreover, we present a more complete model with multi-photothermal effects, and later discuss about the effectiveness of a possible model with nonlinear photothermal effects. By decomposing the photothermal interaction into opposing light-induced effects, we show that the refined model can be used as a simple mathematical tool to build an intuitive yet faithful picture of the complex dynamics in a high-power optomechanical setup. Furthermore, to better understand how the oscillator responds to the optical field, we undertake a detailed analysis of the mirror's reaction to the thermal energy absorbed from the optical field. Based on this we show that separating the photothermal effects into two independent terms is necessary. We then present the second possible model with nonlinear photothermal effects. We give a thorough analysis of the errors and prove that adding only a nonlinear term into the photothermal effect is not sufficient enough for the simulation when the intracavity power is high. This sets essential groundwork for the stabilisation of existing systems, and facilitates the development of new and more precise optomechanical systems for integrated photonics, sensing, and fundamental studies in quantum mechanics.

In this work, the associated theoretical background and experimental setups are covered in Chapter 2-3, including the existing model for the system. The passive stabilisation technique with a laser window for photothermal cancellation is discussed in Chapter 4. The refined models are presented in Chapter 5, with the inclusion of an investigation of photothermal effects and the detailed error analysis of the models.

1.4 Publications

The researches presented in this thesis have been featured in the following papers:

1. Jiayi Qin, Giovanni Guccione, Jinyong Ma, Chenyue Gu, Ruvi Lecamwasam, Ben C. Buchler, and Ping Koy Lam. "Cancellation of photothermally induced instability in an optical resonator". *Optica*, 9(8):924–932, 2022.

2. Chenyue Gu, Jiayi Qin, Giovanni Guccione, Jinyong Ma, Ruvi Lecamwasam, and Ping Koy Lam. "Modeling Photothermal Effects in High Power Optical Resonators used for Coherent Levitation". New J. Phys. 25 123051.

Chapter 2

Background to Optomechanics

The interacting of a mechanical oscillator with an electromagnetic field was pioneered in 1970s [41]. The dynamical influence of radiation pressure on a harmonically suspended end mirror of a cavity, giving either damping or antidamping of mechanical motion, was later observed in a microwave cavity [42]. Similar phenomena were subsequently shown in microwave-coupled kg-scale mechanical resonators [43]. In the optical domain, the first experimental observation of radiation-pressure bistability and optical mirror confinement in a cavity-optomechanical system with a macroscopic end mirror was realised as early as 1983 [44]. All of these achievements combined contributed to the rise of "(cavity) optomechanics", which became very important in the last two decades as a meaningful tool to observe and manipulate mechanical oscillators in the quantum regime.

2.1 Optomechanics

Optomechanics, coupling light fields and mechanical systems via radiation pressure interaction, provides unique tools for applications where a highly sensitive measurement of small displacements, forces, masses, or accelerations is desired, such as gravitational wave detection [45, 46], or high-precision sensors for atomic force microscopy [47]. The ability to cool a mechanical oscillator to its quantum ground state [48] offers a route to control and manipulate the quantum state of truly macroscopic objects, and to conduct measurements at or beyond the standard quantum limit [49, 50]. At a fundamental level, this may lead to a more profound understanding of quantum mechanics and even to tests of quantum theory itself that are in play here [51]. On the practical side, new quantum optomechanical techniques in both the optical and microwave regime have emerged, which provide motion and force detection near the fundamental limit imposed by quantum mechanics, facilitating the potential applications in new metrology tools [52] and even new functions on semiconductor chips [53].

Recent research has explored different physical realisations of cavity optomechanical systems employing cantilevers [54, 55], micro-mirrors [56, 57], micro-cavities [58, 59], nanomembranes [60], and macroscopic mirrors [61]. The dynamics of the coupling of optical and mechanical degrees of freedom in any of these geometries can be understood by con-

sidering the schematic of an optically driven Fabry-Pérot cavity resonator, with one end mirror fixed and the other functioning as a mass-on-a-spring. The incident field that is resonant with the cavity modes creates a large circulating power within the cavity, which exerts a force upon the "movable" mirror, drives it, changes the cavity length, and hence changes the intracavity light field intensity and phase, resulting in a new static equilibrium condition of the system.

Optical spring effect, including both the effects on natural frequency (the spring) and on damping (so called the viscous effect), behaves differently depending on the detuning of the cavity. On the blue side of resonance (higher-frequency detuning), the effect manifests as a restoring force, increasing the frequency of the oscillator. Accompanied with an anti-damping force due to the delay in the cavity response time, it can produce a significant stiffness in the oscillation frequency of the mirror. In contrast, on the red side of resonance (lower-frequency detuning), an anti-restoring force decreases the natural oscillation frequency. Viscous damping, or "cold damping", also occurs in this regime where the optical field can damp the mirror movement and cool its center-of-mass motion [62, 61, 63]. With the ability of changing both the dispersive and dissipative qualities of a mechanical oscillator, the optical spring is advantageous in its tunability, robustness to mechanical loss via a physical connection to an optical zero-temperature thermal bath, and versatility for simultaneous optical readouts. It offers new opportunities for research and applications in optomechanical cooling [55, 64], interferometric gravitational wave detectors [65], and optical control and manipulation of the mechanical quantum state of a mechanical oscillator [66, 67].

In this chapter, a detailed investigation, mathematical description of an optomechanical cavity, and its optical properties, are given, which will further lead to a discussion of optical levitation systems. To lay the foundation for an in-depth study in this field, I will start from the theory of optical and mechanical resonators.

2.2 Optical resonators

An optical resonator or optical cavity refers to an arrangement of mirrors that form a standing wave cavity resonator for light waves, which can be experimentally realised in a multitude of schemes. Here, I present the simplest cavity interacting with a single monochromatic beam to discuss the unifying optical properties and the dynamical features of optical resonators.

2.2.1 Basic properties of an optical cavity

In a simple Fabry-Pérot resonator, as shown in Fig. 2.1, two highly reflective mirrors are placed along the z axis separated by a distance of L. The resonances can be easily derived from the boundary condition of the electromagnetic field of the laser beam circulating

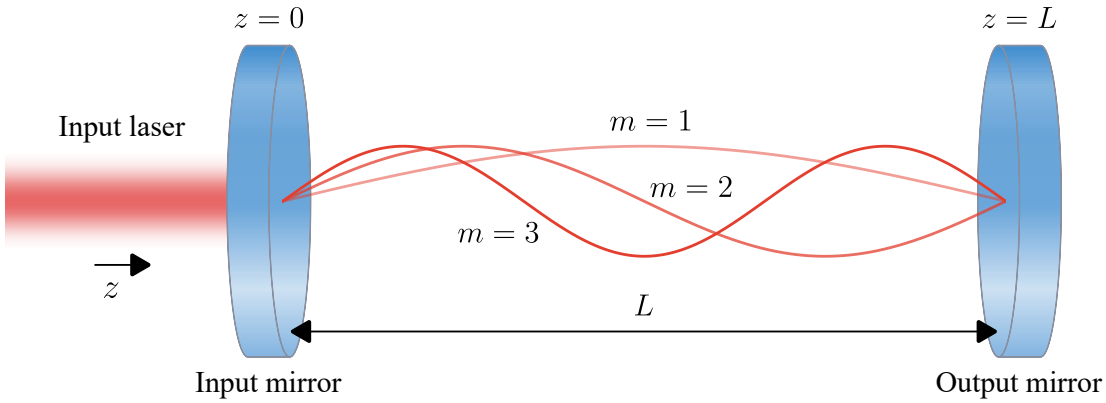

Figure 2.1: Schematic of a Fabry-Pérot cavity with a cavity length of L. A laser beam couples into the cavity via the input mirror and interacts with the optical resonator. The wavelength of the optical modes satisfy $\lambda = 2L/m$, where $m = 1, 2, 3, ...$ The first three eigen-modes of the cavity are illustrated.

between the two mirrors.

The electric ($\mathbf{E}$) and magnetic ($\mathbf{B}$) components of the optical field satisfy Maxwell's equations:

$$\begin{aligned} \nabla \cdot \mathbf{E} = 0, \quad \nabla \times \mathbf{E} = -\frac{\partial \mathbf{B}}{\partial t}, \\ \nabla \cdot \mathbf{B} = 0, \quad \nabla \times \mathbf{B} = \mu_0 \varepsilon_0 \frac{\partial \mathbf{E}}{\partial t}, \end{aligned} \tag{2.1}$$

where μ_0 and ε_0 are the permeability and permittivity of free space respectively, and $c = 1/\sqrt{\mu_0 \varepsilon_0}$ denotes the speed of light. Assuming that the electric field of the beam is linearly polarised along the x axis, a general solution of it from Eq. (2.1) can be written as

$$E_x(z,t) = a e^{i(\omega t + k_m z)} + b e^{i(\omega t - k_m z)}, \tag{2.2}$$

where a and b are dependent on initial condition of the electric field, ω is the angular frequency of the laser beam, and k_m is the wavenumber. The resonance occurs when the boundary condition at the surfaces of the two mirrors meets

$$E_x(z = 0, t) = E_x(z = L, t) = 0, \tag{2.3}$$

which yields $a = -b$ and $k_m = m\pi/L$, with m as an integer mode number. This implies that a cavity with a cavity length of L contains a series of resonances given by the angular frequencies $\omega_{\text{cav},m} = m \cdot \pi c/L$. The separation of two longitudinal resonances is commonly defined as the free spectral range (FSR) of the cavity:

$$\Delta\omega_{\text{FSR}} = \pi \frac{c}{L}. \tag{2.4}$$

A finite photon cavity decay rate, or the total cavity loss, κ, results from finite mirror transparencies, internal absorption, and the possible scattering out of the cavity. Thus, in

our example of the cavity, the total loss can be further split into three different contributions [1]:

$$\kappa = \kappa_{\text{in}} + \kappa_{\text{out}} + \kappa_0, \tag{2.5}$$

where κ_{in} and κ_{out} denote the loss rate associated with the input and output coupling respectively and κ_0 refers to the remaining loss rate. Here we define a useful quantity, optical finesse $\mathcal{F}$,

$$\mathcal{F} \equiv \frac{\Delta\omega_{\text{FSR}}}{\kappa}, \tag{2.6}$$

as it gives the average number of round-trips before a photon leaves the cavity via the loss channel mentioned above. In other words, the finesses of a cavity indicates the amplification of the circulating power over the power coupled into the resonator. Alternatively, giving the photon lifetime inside the cavity as $\tau = \kappa^{-1}$, we introduce the quality factor of the optical resonator to characterise the damping rate,

$$Q_{\text{opt}} = \omega_{\text{cav}}\tau. \tag{2.7}$$

Note that we use κ for the photon decay rate, such that the amplitude decay rate is referred as $\kappa/2$. To simplify the discussion, we will focus on a single optical mode ω_{cav} for the cavity (then the wavenumber is denoted by k), which is almost always the case of the systems investigated in this thesis.

2.2.2 Input-output formalism

A framework known as input-output theory was first presented in 1984, which gives a quantum mechanical description for a light field interacting with a cavity [68, 69], playing a crucial role in the study of classical and quantum optics. Input-output theory allows the modeling of quantum fluctuations injected from any coupling port into the cavity, such as the enhanced coupling between the cavity modes and the external light fields as well as any medium inside the cavity. It overcomes the deficiency of simply using the standard master-equation technique to describe the light field inside a cavity, which treats the external field only as a heat bath and contains no prescription for calculating the properties of the light emitted from the cavity. Thus, input-output theory provides an approach whereby the internal field is linked with the input by identification of the "noise" with the incoming field, and the output is then calculated using the boundary conditions at the cavity mirrors.

Before conducting a deeper discussion into the dynamics of the optical resonator via input-output theory, we give the further simplified solution of the electric field from Eq. (2.2) as

$$E_x(z,t) = Ae^{i(\omega_{\text{cav}}t+\pi/2)}\sin(kz), \tag{2.8}$$

where the amplitude $A = \sqrt{2\omega_{\rm cav}^2/\varepsilon_0 V}$ is obtained by using the normalisation condition of the spatial mode, and V is the volume of the cavity. Substituting Eq. (2.8) into Eq. (2.1), we have the magnetic component of the optical field which is along the y axis,

$$B_y(z,t) = \sqrt{\mu_0\varepsilon_0}Ae^{i(\omega_{\rm cav}t)}\cos(kz). \tag{2.9}$$

Thus, the classical Hamiltonian for the optical field of a single mode cavity is described as

$$\begin{aligned}\mathcal{H}_{\rm O} &= \frac{1}{2}\int dV\left[\varepsilon_0 E_x^2(z,t) + \frac{1}{\mu_0}B_y^2(z,t)\right] \\ &= \frac{1}{2}\left(\omega_{\rm cav}^2 x^2 + (-i\hbar\frac{\partial}{\partial x})^2\right) \\ &= \frac{1}{2}\left(\omega_{\rm cav}^2 x^2 + p^2\right), \end{aligned} \tag{2.10}$$

where $p = -i\hbar\partial/\partial x$, along with x are equivalent to the two canonical variables of a harmonic oscillator. We can quantise Eq. (2.10) by identifying the canonical position x and canonical momentum p as operators $\hat{x}$ and $\hat{p}$, which follow the commutation relations

$$[\hat{x},\hat{x}] = [\hat{p},\hat{p}] = 0 \quad , \quad [\hat{x},\hat{p}] = i\hbar. \tag{2.11}$$

We write the Hamiltonian in terms of the creation ($\hat{a}^\dagger$) and annihilation ($\hat{a}$) operators with the expression as

$$\hat{\mathcal{H}}_{\rm O} = \hbar\omega_{\rm cav}\left(\hat{a}^\dagger\hat{a} + \frac{1}{2}\right), \tag{2.12}$$

where the canonical transformations are given by

$$\begin{aligned}\hat{a}^\dagger &= \frac{1}{\sqrt{2\hbar\omega_{\rm cav}}}\left(\omega_{\rm cav}\hat{x} - i\hat{p}\right), \\ \hat{a} &= \frac{1}{\sqrt{2\hbar\omega_{\rm cav}}}\left(\omega_{\rm cav}\hat{x} + i\hat{p}\right). \end{aligned} \tag{2.13}$$

The commutation relations of the operators will then be

$$[\hat{a},\hat{a}] = [\hat{a}^\dagger,\hat{a}^\dagger] = 0 \quad , \quad [\hat{a},\hat{a}^\dagger] = 1. \tag{2.14}$$

The behavior of the internal mode of a single-mode cavity then can be calculated by the master-equation method, and the quantum Langevin equations become [68]:

$$\frac{{\rm d}\hat{a}}{{\rm d}t} = -\frac{i}{\hbar}[\hat{a},\hat{\mathcal{H}}_{\rm O}] - \frac{\kappa}{2}\hat{a} + \hat{\Gamma}, \tag{2.15}$$

where $\hat{\Gamma}$ is the noise operator. For a single-ended cavity, there is no coupling of the extrinsic laser field via the output mirror (which refers to another end mirror of a cavity), then the

effects of that mirror can be grouped into the decay κ_0 and the Eq. (2.5) turns to

$$\kappa = \kappa_{\rm in} + \kappa_0. \tag{2.16}$$

The noise $\hat{\Gamma}$ of this simplest case can be ascribed to the incoming part of the radiation field outside the mirror plus the "unwanted" noise channel $\hat{f}_{\rm in}$ associated with the loss rate κ_0, written as

$$\hat{\Gamma} = \sqrt{\kappa_{\rm in}}\hat{a}_{\rm in} + \sqrt{\kappa_0}\hat{f}_{\rm in}, \tag{2.17}$$

with which the Heisenberg equation of the motion can be given to describe the time evolution of the intracavity field amplitude $\hat{a}$,

$$\dot{\hat{a}} = -\frac{\kappa}{2}\hat{a} + i\Delta\hat{a} + \sqrt{\kappa_{\rm in}}\hat{a}_{\rm in} + \sqrt{\kappa_0}\hat{f}_{\rm in}. \tag{2.18}$$

Here we present the equations in a rotating frame with the laser frequency $\omega_{\rm l}$, and introduce the laser detuning $\Delta = \omega_{\rm l} - \omega_{\rm cav}$ with respect to the cavity mode. The input field coupling into the cavity at time t is denoted by $\hat{a}_{\rm in}(t)$. The input power launched into the cavity reads

$$P_{\rm in} = \hbar\omega_{\rm l}\langle\hat{a}_{\rm in}^{\dagger}\hat{a}_{\rm in}\rangle. \tag{2.19}$$

Given from a quantum perspective, $\langle\hat{a}_{\rm in}^{\dagger}\hat{a}_{\rm in}\rangle$ is the rate of photons arriving at the cavity. According to the input-output theory of open quantum systems, a boundary condition at the input mirror of a Fabry-Pérot resonator is given by

$$\sqrt{\kappa_{\rm in}}\hat{a} = \hat{a}_{\rm in} + \hat{a}_{\rm out}. \tag{2.20}$$

Taking the average of Eq. (2.18) and Eq. (2.20), we can solve them with the condition of $\langle\dot{\hat{a}}\rangle = 0$ and obtain the amplitude of the steady-state intracavity and output fields:

$$\langle\hat{a}\rangle = \frac{\sqrt{\kappa_{\rm in}}\langle\hat{a}_{\rm in}\rangle}{\kappa/2 - i\Delta}, \tag{2.21}$$

$$\langle\hat{a}_{\rm out}\rangle = \frac{(\kappa_{\rm in} - \kappa/2 + i\Delta)\,\langle\hat{a}_{\rm in}\rangle}{\kappa/2 - i\Delta}, \tag{2.22}$$

where we have used the fact that $\langle\hat{f}_{\rm in}\rangle = 0$. The optical susceptibility which links the input field to the intracavity field, is defined as

$$\chi_{\rm opt}(\omega) \equiv \frac{1}{-i\,(\omega + \Delta) + \kappa/2}, \tag{2.23}$$

where ω denotes the Fourier frequency of the fluctuations of the input field around its laser frequency $\omega_{\rm l}$. Inserting Eq. (2.16) into Eq. (2.21)-(2.22) and dividing the energy of photons in the cavity by the time scale of the cavity, we obtain the intracavity power

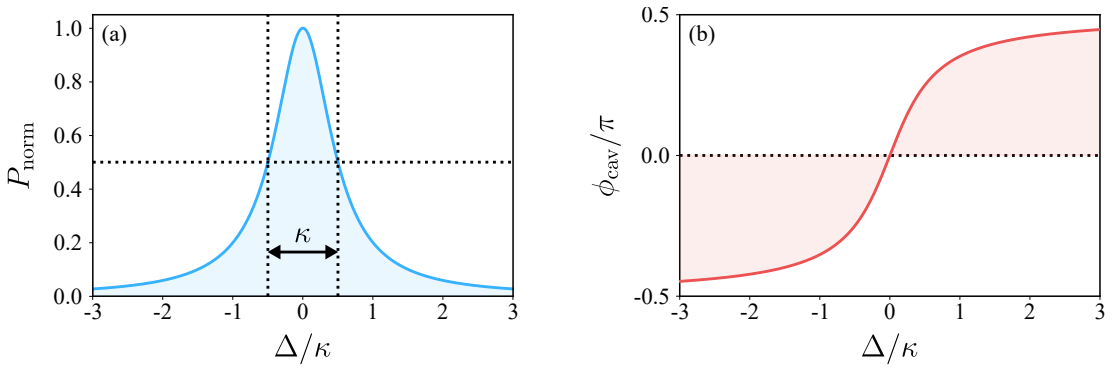

Figure 2.2: Steady-state cavity response to a varying detuning. (a) Normalised intracavity power varying with cavity detuning, the detuning of the cavity is in the unit of cavity loss κ. (b) Phase response of the intracavity field as a function of detuning.

($\tau_{\text{cav}} = 2L/c$):

$$P_{\text{cav}} = \hbar\omega_{\text{l}} \left|\langle\hat{a}\rangle\right|^2 / \tau_{\text{cav}} = \frac{\kappa_{\text{in}}/\tau_{\text{cav}}}{\left(\kappa_{\text{in}} + \kappa_0\right)^2/4 + \Delta^2} P_{\text{in}}. \tag{2.24}$$

The intracavity power is maximised at the resonant condition when $\Delta = 0$. By introducing a parameter $\alpha = \kappa_{\text{in}}/\kappa$ to denote the ratio of the loss at the input mirror to the total loss, the cavity power at resonance can be then written in terms of cavity finesse as

$$P_{\text{resonance}} = \frac{2\alpha}{\pi} \mathcal{F} P_{\text{in}}. \tag{2.25}$$

It indicates that the resonant intracavity power is proportional to the cavity finesse and the input power, which explains why the finesse is of great importance in the experiments where very high intracavity power needs to be obtained.

We now investigate how the normalised power and phase of the intracavity field responds to the change of the laser detuning with the expression:

$$P_{\text{norm}} = \frac{1}{1 + (2\Delta/\kappa)^2}, \tag{2.26}$$

$$\phi_{\text{cav}} = \arctan\left(\frac{2\Delta}{\kappa}\right), \tag{2.27}$$

which are presented in Fig. 2.2. As shown in Fig. 2.2(a), the plot of normalised intracavity power shows a Lorentzian profile, where the full width at half-maximum of the power is equal to the total decay of the cavity. Given this property, κ is also commonly called the linewidth of a cavity. The plot of the phase response, shown in Fig. 2.2(b), suggests that the phase of the intracavity field is approximately linear in the cavity detuning around the cavity resonance.

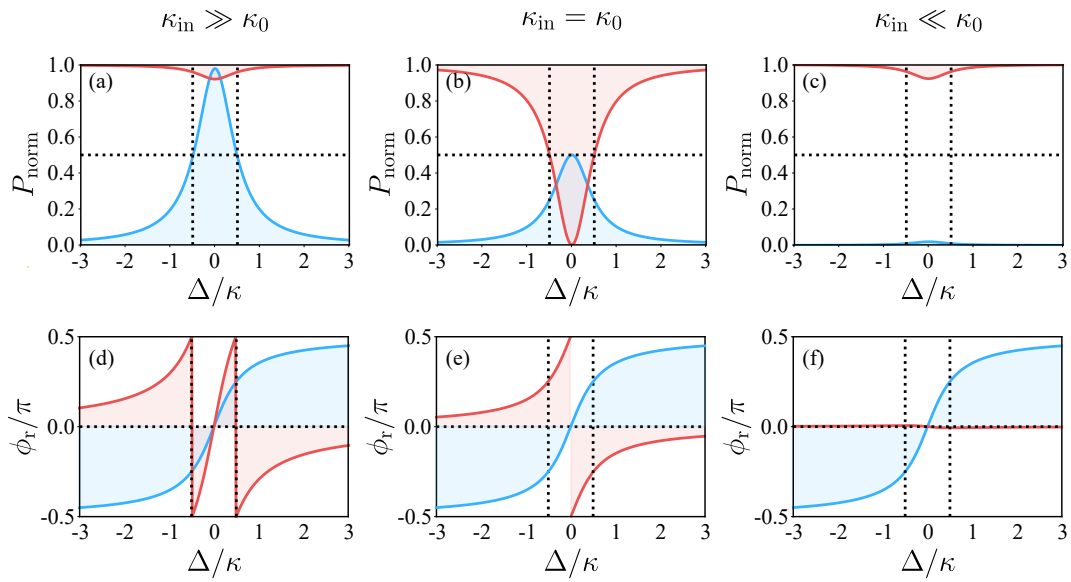

Figure 2.3: Light power of the intracavity field (blue) and the reflection (red) of a Fabry-Pérot cavity where only one end mirror coupling is of interest. (a)-(c) Reflection $|\mathcal{R}|^2$ and normalised intracavity power $P_{\text{cav, norm}}$ under the three typical situations of losses. In the case of (a) where the input coupling dominates the cavity loss ($\kappa_{\text{in}} = 0.98\kappa$), the cavity is "overcoupled". When the external coupling is equal to the internal loss ($\kappa_{\text{in}} = \kappa_0 = 0.5\kappa$) as shown in (b), the cavity experiences the situation of "critical coupling". When the input coupling is negligible compared to the intrinsic loss ($\kappa_{\text{in}} = 0.02\kappa$), the cavity enters to an "undercoupling" regime. (d)-(f) give the phase responses correspond to the three different situations when the input couplings are 98%, 50% and 2% of the total loss respectively.

Moreover, the reflection amplitude $\mathcal{R}$ can be calculated from Eq. (2.22),

$$\mathcal{R} = \frac{\langle \hat{a}_{\text{out}} \rangle}{\langle \hat{a}_{\text{in}} \rangle} = \frac{(\kappa_{\text{in}} - \kappa_0)/2 + i\Delta}{(\kappa_{\text{in}} + \kappa_0)/2 - i\Delta}. \tag{2.28}$$

Thus, $|\mathcal{R}|^2$ gives the probability of reflection from the cavity.

Three typical regimes that a cavity might experience with three different situations for the losses are given in Fig. 2.3. When the input coupling κ_{in} dominates the cavity loss where $\kappa_{\text{in}} \gg \kappa_0$, the cavity is called "overcoupled". We can read from the panel (a) that the reflection of the cavity is almost equal to 1, and the intracavity power reaches its highest at resonance compared to the other two scenarios. That's because in this case, most of the photons sent into the cavity are reflected back from the second mirror and travel back via the input mirror without any other losses (scattering inside the cavity for example). If the external coupling is equal to other internal losses ($\kappa_{\text{in}} = \kappa_0$), the cavity enters into the regime of "critical coupling", where the reflection $\mathcal{R} = 0$ at resonance, presented in panel (b). This implies that the light is fully dissipated within the resonator or transmitted through the other mirror (note that in the cavity of one end mirror, the transmission is not a term that is of interest). In the case of "undercoupling" where $\kappa_{\text{in}} \ll \kappa_0$ (seen in panel (c)), the loss of the cavity is dominated by intrinsic losses. Most

of the light is directly reflected back from the input mirror, so that the intracavity power is close to 0 at any value of detuning. This coupling condition is not advantageous for many experiments as it causes effective information loss.

In a more common scenario, we will also be interested in the transmission via the other end mirror (the output mirror in Fig. 2.1), noting that there won't be a 100 % reflecting mirror in practical experiments. Therefore, considering the case of a two-sided cavity is sometimes necessary. Later after introducing the transmission of the cavity we will further show that using transmission of the cavity to monitor the intracavity field is more intuitive and convenient. We can insert an additional term for the external coupling via the output mirror $\sqrt{\kappa_{\text{out}}}\hat{a}_{\text{in}}^{(2)}$ in Eq. (2.18) and replace $\hat{a}_{\text{in}}$ to $\hat{a}_{\text{in}}^{(1)}$ for a clearer notation of the field going in and out of the input mirror. The cavity loss is thus expressed by Eq. (2.5), and an equation analogous to Eq. (2.20) will hold for the output field $\hat{a}_{\text{out}}^{(2)}$ at the output mirror. This gives

$$\dot{\hat{a}} = -\frac{\kappa}{2}\hat{a} + i\Delta\hat{a} + \sqrt{\kappa_{\text{in}}}\hat{a}_{\text{in}}^{(1)} + \sqrt{\kappa_{\text{out}}}\hat{a}_{\text{in}}^{(2)} + \sqrt{\kappa_0}\hat{f}_{\text{in}}, \tag{2.29}$$

$$\hat{a} = \frac{1}{\sqrt{\kappa_{\text{out}}}}\left(\hat{a}_{\text{in}}^{(2)} + \hat{a}_{\text{out}}^{(2)}\right). \tag{2.30}$$

Because the input laser is only introduced into the cavity via the input mirror, we have $\langle\hat{a}_{\text{in}}^{(2)}\rangle = 0$. With a similar calculation as was applied to the one-sided cavity, from Eq. (2.29), Eq. (2.20) and Eq. (2.30), we obtain the amplitude of the intracavity $\langle\hat{a}\rangle$ and output $\langle\hat{a}_{\text{out}}^{(1)}\rangle$ fields via the input mirror with the same expression as Eq. (2.21) and Eq. (2.22) respectively. Furthermore, we also get the amplitude of the output field via the output mirror as

$$\langle\hat{a}_{\text{out}}^{(2)}\rangle = \sqrt{\kappa_{\text{out}}}\langle\hat{a}\rangle = \frac{\sqrt{\kappa_{\text{out}}\kappa_{\text{in}}}\langle\hat{a}_{\text{in}}^{(1)}\rangle}{\left(\kappa_{\text{in}} + \kappa_{\text{out}} + \kappa_0\right)/2 - i\Delta}, \tag{2.31}$$

where the reflection $\mathcal{R}$ and transmission $\mathcal{T}$ of the cavity are obtained

$$\mathcal{R} = \frac{\langle\hat{a}_{\text{out}}^{(1)}\rangle}{\langle\hat{a}_{\text{in}}^{(1)}\rangle} = \frac{\left(\kappa_{\text{in}} - \kappa_{\text{out}} - \kappa_0\right)/2 + i\Delta}{\left(\kappa_{\text{in}} + \kappa_{\text{out}} + \kappa_0\right)/2 - i\Delta}, \tag{2.32}$$

$$\mathcal{T} = \frac{\langle\hat{a}_{\text{out}}^{(2)}\rangle}{\langle\hat{a}_{\text{in}}^{(1)}\rangle} = \frac{\sqrt{\kappa_{\text{out}}\kappa_{\text{in}}}}{\left(\kappa_{\text{in}} + \kappa_{\text{out}} + \kappa_0\right)/2 - i\Delta}, \tag{2.33}$$

and the amplitude of the intracavity field can be written as

$$\langle\hat{a}\rangle = \frac{\sqrt{\kappa_{\text{in}}}\langle\hat{a}_{\text{in}}^{(1)}\rangle}{\left(\kappa_{\text{in}} + \kappa_{\text{out}} + \kappa_0\right)/2 - i\Delta}. \tag{2.34}$$

With Eq. (2.31) and (2.34), it is obvious that the amplitude of the transmitted field is proportional to the intracavity field with a factor of $\sqrt{\kappa_{\text{out}}}$, while the phase of the transmission and the intracavity field stays the same. Therefore using the transmission to

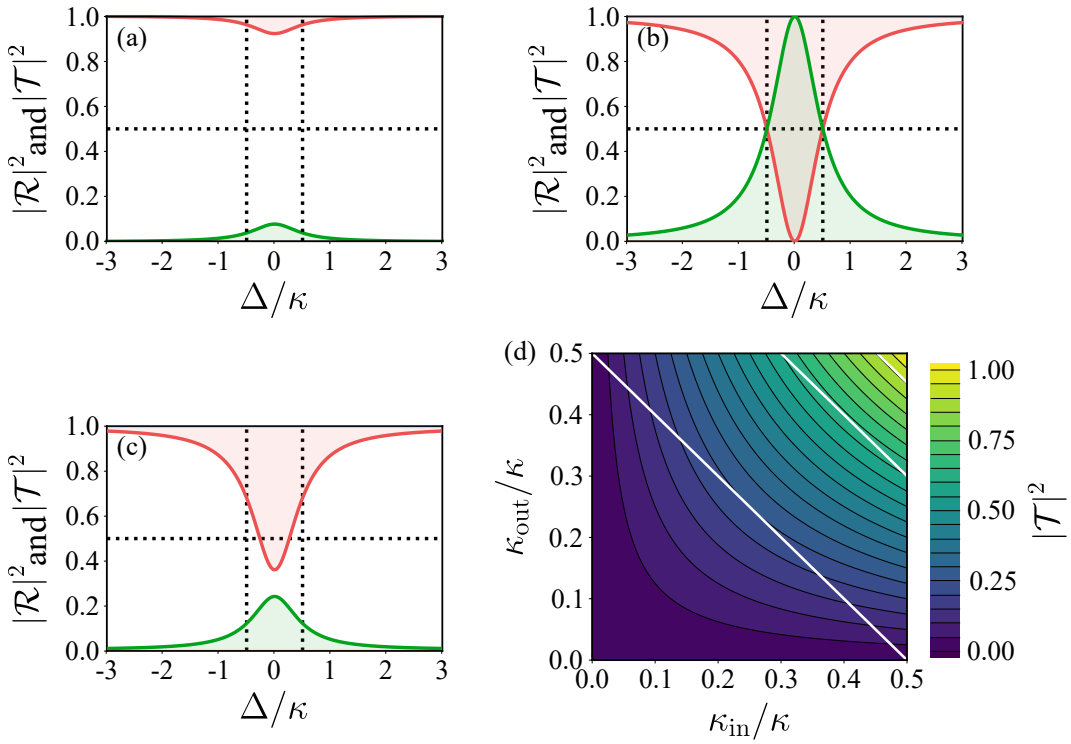

Figure 2.4: Impedance matching of a Fabry-Pérot cavity. (a), (b) and (d) are plotted under the assumption that the cavity intrinsic loss $\kappa_0 = 0$, giving the reflected (red) and transmitted (green) fields during a scan across resonance. When the cavity is overcoupled ($\kappa_{\rm in} = 0.98\kappa, \kappa_{\rm out} = 0.02\kappa$), as shown in (a) most of the light is reflected whereas very little light is transmitted, even though the optical field inside the cavity has a high power. (b) gives the cavity response under the losses case where $\kappa_{\rm in} = \kappa_{\rm out} = 0.5\kappa$. On resonance no reflection is presented and the field is fully transmitted, implying optimal (100%) impedance matching for the cavity. (c) Reflection and transmission with an intrinsic cavity loss $\kappa_0 = 0.5\kappa$ and different losses induced by the two mirrors ($\kappa_{\rm in} = 0.2\kappa$ and $\kappa_{\rm out} = 0.3\kappa$). (d) Impedance matching as a function of losses via input and output mirrors. The three white lines, from up-right to down-left, are the possible values of $\kappa_{\rm in}$ and $\kappa_{\rm out}$ when $\kappa_0 = 0.1\kappa,\ 0.2\kappa,\ 0.5\kappa$ respectively.

monitor the intracavity field is convenient. Another benefit of using transmission is that when there is no light sent into the cavity via the output mirror, the transmission will not interfere with other light fields, while the interference has to be considered when using reflection as the monitoring approach.

The reflection, transmission, and intracavity fields are determined by the intrinsic cavity loss and the losses induced by the two mirrors, which can be seen in Eq. (2.32)-(2.34). Thus by selecting the values for the loss rates of the two mirrors, a desired cavity response can be achieved. This practice is known in resonator optics as impedance matching. Examples of different impedance matching scenarios are presented in Fig. 2.4. The first example is given when the intrinsic loss of the cavity is not considered and decay rate of the input mirror is dominant. From Fig. 2.3(a), we have already seen that the intracavity field is strongest among the different cases, but Fig. 2.4(a) tells us that the transmission is very low, which is in agreement with the situation that the output loss $\kappa_{\rm out}$ does not contribute.

If we investigate the cavity where the two mirrors have same losses (Fig. 2.4(b)), however, we will find the intracavity light is all transmitted and no light is reflected on the resonance. Another example is illustrated with a finite loss inside the cavity, photons then have another channel to escape from the cavity (scattering, etc.), so that the sum of transmission and the reflection is smaller than 1 (Fig. 2.4(c)). The level of impedance matching is determined by the proportion of the input field being transmitted. The cavity transmission under the cases with possible values of losses shown in Fig. 2.4(d) indicates that the perfect impedance matching conditions are achieved when $\kappa_{\text{in}} = \kappa_{\text{out}}$.

2.2.3 Cavity dynamics

Now we investigate the time evolution of a cavity. In the semiclassical regime where a sufficiently large number of photons is considered, we use the mean response of the operators to describe the system and ignore the quantum noise. Denoting the mean value of the amplitude of the light field as $\langle \hat{a}(t) \rangle \to a$ and $\langle \hat{a}_{\text{in}}(t) \rangle \to a_{\text{in}}$, the cavity can be described by a classical equation as follows:

$$\dot{a} = -\frac{\kappa}{2} a + i\Delta a + \sqrt{\kappa_{\text{in}}} a_{\text{in}}. \tag{2.35}$$

From this we get the analytical solution, which allows us to analyse the dynamics of the cavity with the initial condition $a|_{t=0} = 0$,

$$a = \frac{\sqrt{\kappa_{\text{in}}} a_{\text{in}}}{\kappa/2 - i\Delta} \left[1 - e^{-(\kappa/2 - i\Delta)t} \right]. \tag{2.36}$$

The time evolution of a cavity transmission rate ($a_{\text{out}}/a_{\text{in}}$) under different cavity detuning is presented in Fig. 2.5(a), which, as we mentioned earlier, equivalently shows the behaviour of the intracavity field. When an impedance matched cavity is driven by a laser with a resonant frequency ($\Delta = 0$), the light field inside the cavity gradually builds up with a decay rate of κ, and then reaches the equilibrium state that corresponds to the steady-state solution described by Eq. (2.33) and (2.34). With cavity detuning, optical oscillations are shown in the time evolution, which is analogous to the dynamics of an under-damped mechanical oscillator. Here the plots show that a higher detuning leads to a more obvious oscillation before the cavity reaches the equilibrium state.

In experiments, we usually investigate the cavity behaviour by scanning the cavity detuning (laser frequency or cavity length). Here we discuss the case that the cavity length is changing linearly in time as $L(t) = L_0 + vt$ with one end mirror moving at speed v. Therefore we have

$$\Delta(t) = \frac{k \cdot 2L(t)}{\tau_{\text{cav}}} = 2k \frac{L_0 + v \cdot t}{\tau_{\text{cav}}} = \Delta_0 + \frac{2kv \cdot t}{\tau_{\text{cav}}}, \tag{2.37}$$

where L_0 and Δ_0 are the initial cavity length and detuning respectively. Eq. (2.35) is then

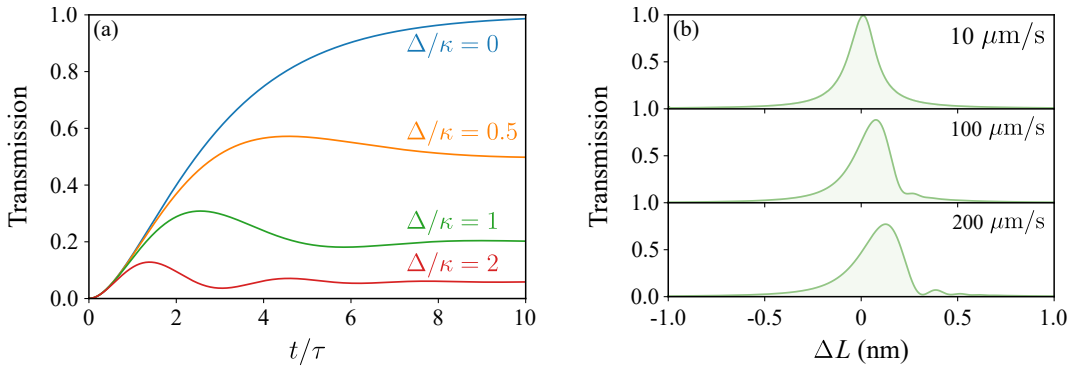

Figure 2.5: Time evolution of a cavity with and without a scan of cavity detuning. The transmissions of a cavity responding to a driving laser with different frequencies are presented in (a). For simplicity, the cavity is set in the "critical coupling" regime ($\kappa_{\text{in}} = \kappa_{\text{out}} = 0.5\kappa$) and no intrinsic loss is included ($\kappa_0 = 0$). Time is plotted in a unit of photon life time $\tau = \kappa^{-1}$. (b) Cavity response with different scan speeds. The transmission is normalised to that of a cavity on resonance. In this simulation we use the following parameters: $k = 2\pi/\lambda, \lambda = 1050\,\text{nm}, \tau_{\text{cav}} = 2L_0/c, L_0 = 0.08\,\text{m}, \kappa_{\text{in}} = \kappa_{\text{out}} = \kappa/2 = 2\pi \times 0.3\,\text{MHz}$. The scan speeds of the plots from top to bottom are $10\,\mu\text{m}\,\text{s}^{-1}$, $100\,\mu\text{m}\,\text{s}^{-1}$, and $200\,\mu\text{m}\,\text{s}^{-1}$ respectively.

modified with the time-dependent detuning, as

$$\dot{a} = -\frac{\kappa}{2}a + i\left(\Delta_0 + \frac{2kv \cdot t}{\tau_{\text{cav}}}\right)a + \sqrt{\kappa_{\text{in}}}a_{\text{in}}. \tag{2.38}$$

The numerical solutions of the cavity transmission as a function of cavity length change for different scan speeds are shown in Fig. 2.5(b). Compared to the Lorentzian plot with low scan speed (top), when the end mirror moves in a particular direction, the solutions show signs of asymmetry. With a faster scan on detuning, the peaks start showing stronger additional ripples after the cavity passes the resonance. Moreover, a lower peak power and a shift of the maximum point are also observed at a higher scan speed. Because, with a fast scan, the cavity is not able to reach the steady state before the cavity length changes to the next step which changes the resonance condition. With a slower scan, each point can be considered as a steady-state solution, so the response shows a Lorentzian profile.

2.3 Mechanical resonators

After giving an exhaustive description of the "optical" part of the term optomechanics, now we start to investigate the "mechanical" part of it. In order to understand the dynamics behind a moving mirror, we will outline the classical and quantum theory of mechanical resonators.

2.3.1 Equation of motion

The vibrational modes of an object can be obtained by imagining the simple harmonic motion of a body that is attached to a spring with one end fixed. Considering the body moves along the center axis of the spring, the equation of motion for the body is described as

$$m\ddot{x} = F_{\mathrm{r}} + F_{\mathrm{f}} + F_{\mathrm{ex}}, \tag{2.39}$$

where x is the displacement of the body from the equilibrium position. The force acting on this resonator includes the restoring force (F_{r}) exerted by the tension of the spring, the resistance force from the environment (F_{f}), and an external driving force (F_{ex}). Hooke's law gives a linear correspondence between the restoring force and the mechanical displacement with the spring constant (or stiffness) denoted by k:

$$F_{\mathrm{r}} = -kx. \tag{2.40}$$

Additionally, the resistance can be considered linear with the velocity of the body for the slow viscous flow, thus the expression for the resistance force is written as

$$F_{\mathrm{f}} = -\alpha\dot{x}, \tag{2.41}$$

where α is the resistance constant. By substituting Eq. (2.40) and (2.41) into Eq. (2.39), a differential equation to describe the motion is given as

$$m\ddot{x} + m\gamma\dot{x} + kx = F_{\mathrm{ex}}, \tag{2.42}$$

where $\gamma = \alpha/m$ is defined as the damping rate of the motion.

Solving the Eq. (2.42) under an assumption that no external driving forces is involved, we have the general equation as the solution of the oscillator's motion

$$x(t) = e^{-\frac{\gamma}{2}t}\left(A_1 e^{t\sqrt{\gamma^2/4-\omega_{\mathrm{m}}^2}} + A_2 e^{-t\sqrt{\gamma^2/4-\omega_{\mathrm{m}}^2}}\right), \tag{2.43}$$

with its characteristic frequency $\omega_m = \sqrt{k/m}$, where the parameters A_1 and A_2 are given by the initial condition of the system. If there is no damping in the system ($\gamma = 0$), the general solution gives the expression of a harmonic oscillator,

$$x(t) = A_0 \cos(\omega_{\mathrm{m}} t + \phi_0), \tag{2.44}$$

of which the amplitude A_0 and the phase ϕ_0 are determined by the initial condition. Moreover, the value of $\gamma^2/4 - \omega_{\mathrm{m}}^2$ determines the dynamics of the oscillator, giving three different situations — under damping ($\gamma/2 < \omega_{\mathrm{m}}$), critical damping ($\gamma/2 = \omega_{\mathrm{m}}$), and over damping ($\gamma/2 > \omega_{\mathrm{m}}$). In the case that the oscillator is under damped, it oscillates with a frequency of $\sqrt{\gamma^2/4 - \omega_{\mathrm{m}}^2}$ and an amplitude damping rate of $\gamma/2$. A dimensionless

quantity known as quality factor or Q factor can be used to describe how underdamped an oscillator or resonator is, as a higher Q indicates a lower energy loss rate. The Q factor reads

$$Q = \frac{\omega_{\mathrm{m}}}{\gamma}. \tag{2.45}$$

The vibrational modes of any object can be described as a harmonic oscillation with damping. The normal modes of the object correspond to their eigenfrequencies $\Omega_{(\mathrm{n})}$. In the following discussion, we mostly focus on a single normal mode of vibration, replacing the physical mass with the effective mass m_{eff} of the oscillator, with the frequency denoted as Ω_{m}. The loss of the mechanical energy is described by the damping rate Γ_{m}. The temporal evolution of the amplitude of the motion in Eq. (2.42) thus becomes as

$$m_{\mathrm{eff}}\left(\ddot{x} + \Gamma_{\mathrm{m}}\dot{x} + \Omega_{\mathrm{m}}^2 x\right) = F_{\mathrm{ex}}(t). \tag{2.46}$$

Here $F_{\mathrm{ex}}(t)$ denotes the sum of all forces that are acting on the mechanical oscillator. By introducing the Fourier transform via

$$\tilde{x}(\omega) = \int_{-\infty}^{\infty} x(t)e^{i\omega t}\,dt \tag{2.47}$$

$$\tilde{F}_{\mathrm{ex}}(\omega) = \int_{-\infty}^{\infty} F_{\mathrm{ex}}(t)e^{i\omega t}\,dt, \tag{2.48}$$

we obtain the equation of motion in the frequency domain

$$\tilde{x}(\omega) = \chi_{\mathrm{m}}(\omega)\tilde{F}_{\mathrm{ex}}(\omega) \quad \text{with} \quad \chi_{\mathrm{m}}(\omega) = \frac{1}{m_{\mathrm{eff}}\left(\Omega_{\mathrm{m}}^2 - \omega^2\right) - i m_{\mathrm{eff}}\Gamma_{\mathrm{m}}\omega}. \tag{2.49}$$

The mechanical susceptibility χ_{m} defined above characterises the dynamical response of an oscillator to an external driving force.

2.3.2 Displacement spectral density

In experiments, the mechanical motion is often measured in frequency space rather than in real time, to allow a separation of the contributions of different normal modes. The spectral density of the measured displacement is defined by the Fourier transform $S_{\mathrm{xx}}(\omega)$ of the autocorrelation function:

$$S_{\mathrm{xx}} \equiv \int_{-\infty}^{\infty} \langle x(t)x(0)\rangle e^{i\omega t} dt. \tag{2.50}$$

For a given signal that is obtained during a measurement time τ_{m}, we define the gated Fourier transform over a finite time interval:

$$\tilde{x}(\omega) = \frac{1}{\sqrt{\tau_{\mathrm{m}}}} \int_0^{\tau_{\mathrm{m}}} x(t)e^{i\omega t} dt. \tag{2.51}$$

Under the assumption that the mechanical process is stationary and is of finite intensity, the Wiener-Khinchin theorem connects Eq. (2.50) and (2.51) when $\tau_{\mathrm{m}} \to \infty$ [1],

$$\lim_{\tau_{\mathrm{m}} \to \infty} \langle |\tilde{x}(\omega)|^2 \rangle = S_{\mathrm{xx}}(\omega). \tag{2.52}$$

From Eq. (2.50) and (2.52), it is easy to show that the area under the experimentally measured power spectral density yields the variance of the mechanical displacement $\langle x^2 \rangle$:

$$\langle x^2 \rangle = \frac{1}{2\pi} \int_{-\infty}^{\infty} S_{\mathrm{xx}}(\omega) d\omega. \tag{2.53}$$

2.3.3 Quantisation of a harmonic oscillator

For a harmonic oscillator, the classical Hamiltonian is given as

$$\mathcal{H}_{\mathrm{M}} = \frac{p^2}{2m_{\mathrm{eff}}} + \frac{1}{2} m_{\mathrm{eff}} \Omega_{\mathrm{m}}^2 x^2 \tag{2.54}$$

where p represents the momentum. The first and the second terms describe the kinetic energy and the potential energy due to the restoring force respectively. By replacing p and x with operators $\hat{p}$ and $\hat{x}$, the Hamiltonian is quantised as

$$\hat{\mathcal{H}}_{\mathrm{M}} = \frac{\hat{p}^2}{2m_{\mathrm{eff}}} + \frac{1}{2} m_{\mathrm{eff}} \Omega_{\mathrm{m}}^2 \hat{x}^2. \tag{2.55}$$

The momentum $\hat{p}$ and position $\hat{x}$ operators are subject to the canonical commutation relation given as

$$[\hat{x}, \hat{p}] = i\hbar. \tag{2.56}$$

Thus, we define the two conjugate observables — creation $\hat{b}^\dagger$ and annihilation $\hat{b}$ operators (also known as ladder operators), as follows

$$\hat{b}^\dagger = \frac{1}{\sqrt{2m_{\mathrm{eff}}\hbar\Omega_{\mathrm{m}}}} \left(m_{\mathrm{eff}} \Omega_{\mathrm{m}} \hat{x} - i\hat{p} \right), \tag{2.57}$$

$$\hat{b} = \frac{1}{\sqrt{2m_{\mathrm{eff}}\hbar\Omega_{\mathrm{m}}}} \left(m_{\mathrm{eff}} \Omega_{\mathrm{m}} \hat{x} + i\hat{p} \right), \tag{2.58}$$

which obey the commutation relation

$$[\hat{b}, \hat{b}^\dagger] = 1. \tag{2.59}$$

Note that $\hat{b}^\dagger$ is the mechanical equivalent of the optical creation operator $\hat{a}^\dagger$ defined earlier. One interpretation of $\hat{b}^\dagger$ and $\hat{b}$ considers them as the creation and annihilation of a quasi-particle of mechanical oscillation, known as a phonon. Therefore, the momentum and the

position operator can be written with the two ladder operators as

$$\hat{x} = x_{\mathrm{ZPF}}\left(\hat{b}^{\dagger}+\hat{b}\right), \tag{2.60}$$

$$\hat{p} = im_{\mathrm{eff}}\Omega_{\mathrm{m}}x_{\mathrm{ZPF}}\left(\hat{b}^{\dagger}-\hat{b}\right), \tag{2.61}$$

where

$$x_{\mathrm{ZPF}} = \sqrt{\frac{\hbar}{2m_{\mathrm{eff}}\Omega_{\mathrm{m}}}} \tag{2.62}$$

is the zero-point fluctuation amplitude of the mechanical oscillator. In this regard, with substitution of Eq. (2.60) and (2.61) into Eq. (2.55), we can rewrite the Hamiltonian as

$$\hat{\mathcal{H}}_{\mathrm{M}} = \hbar\Omega_{\mathrm{m}}\left(\hat{b}^{\dagger}\hat{b}+\frac{1}{2}\right), \tag{2.63}$$

where the operator $\hat{b}^{\dagger}\hat{b}$ describes the number of the phonons of the system. The ground state of this mechanical system has a fundamental energy of $\hbar\Omega_{\mathrm{m}}/2$, and each additional phonon adds a quantum of $\hbar\Omega_{\mathrm{m}}$ to the total energy.

2.4 Dynamics of optomechanical systems

Coupling the properties of the cavity radiation field to the mechanical motion via momentum transfer of photons, the field of optomechanics has emerged. The simplest form of optical-mechanical coupling occurs in a Fabry-Pérot cavity with one end mirror fixed and another movable mirror acting as a mechanical resonator. The radiation-pressure coupling comes from the transfer of photon momentum due to the reflection perpendicular to the mirror's surface. A single photon with a wavelength of λ transfers the momentum $|\Delta p| = 2\hbar k = 2\hbar \times 2\pi/\lambda$. The radiation pressure force experienced by the mirror, caused by the intracavity photons, is therefore expressed as

$$\langle \hat{F}_{\mathrm{opt}}\rangle = 2\hbar k\frac{\langle \hat{a}^{\dagger}\hat{a}+1/2\rangle}{\tau_{\mathrm{cav}}} = \hbar\frac{\omega_{\mathrm{cav}}}{L}\langle \hat{a}^{\dagger}\hat{a}+\frac{1}{2}\rangle, \tag{2.64}$$

where $\tau_{\mathrm{cav}} = 2L/c$ is the cavity round trip time.

2.4.1 Hamiltonian formulation

Considering the uncoupled optical (Eq. (2.12)) and mechanical (Eq. (2.63)) modes that are represented by two harmonic oscillators, we give the approximate Hamiltonian of the system where the interaction between the radiation field and the mirror is not introduced

yet:

$$\hat{\mathcal{H}}_0 = \hbar\omega_{\mathrm{cav}}\left(\hat{a}^\dagger\hat{a} + \frac{1}{2}\right) + \hbar\Omega_{\mathrm{m}}\left(\hat{b}^\dagger\hat{b} + \frac{1}{2}\right). \tag{2.65}$$

With a movable mirror, however, the cavity length changes with the displacement of the oscillator, thus the cavity resonance frequency ω_{cav} is modulated by the mechanical amplitude, where we have

$$\begin{aligned} \omega_{\mathrm{cav}}(x) &= \frac{m\pi c}{L+x} \\ &\simeq \frac{m\pi c}{L} - \frac{m\pi c}{L^2}x + ... \\ &= \omega_{\mathrm{cav}} - Gx + ... \end{aligned} \tag{2.66}$$

Here an assumption that $x \ll L$ is made. The parameter $G = m\pi c/L^2 = \omega_{\mathrm{cav}}/L$ converting the displacement of the mirror to the frequency change, is known as frequency pull parameter. In the following sections, it can be seen that this parameter also links to the optomechanical coupling strength.

By substituting Eq. (2.66) into Eq. (2.65), the cavity Hamiltonian with the mechanical modulation can hence be split into the generic cavity Hamiltonian and the interaction Hamiltonian, so that the Hamiltonian of the optomechanical system can be described as:

$$\hat{\mathcal{H}}_{\mathrm{sys}} = \hat{\mathcal{H}}_{\mathrm{O}} + \hat{\mathcal{H}}_{\mathrm{M}} + \hat{\mathcal{H}}_{\mathrm{int}}, \tag{2.67}$$

with $\hat{\mathcal{H}}_0$ and $\hat{\mathcal{H}}_{\mathrm{M}}$ is given by Eq. (2.12) and (2.63) respectively. The interaction term is given by

$$\hat{\mathcal{H}}_{\mathrm{int}} = -\hbar G\hat{x}\left(\hat{a}^\dagger\hat{a} + \frac{1}{2}\right) = -\hbar G x_{\mathrm{ZPF}}\left(\hat{a}^\dagger\hat{a} + \frac{1}{2}\right)\left(\hat{b} + \hat{b}^\dagger\right), \tag{2.68}$$

where we use the definition of the position operator mentioned in Eq. (2.60). Another important quantity of the system, the vacuum optomechanical coupling strength, is obtained:

$$g_0 = G x_{\mathrm{ZPF}}. \tag{2.69}$$

Generally speaking, g_0 is more fundamental than G, because it quantifies the interaction between a single photon and a single phonon. In the cavity optomechanical system discussed in this work, the cavity is usually detuned by more than half of the linewidth using a piezo and the cavity responses are investigated under the semiclassical regime, thus G is more useful to know.

From the derivative of $\hat{\mathcal{H}}_{\mathrm{int}}$ with the respect to displacement, we can identify the

radiation pressure force acting on the oscillator,

$$\hat{F}_{\rm opt} = -\frac{{\rm d}\hat{\mathcal{H}}_{\rm int}}{{\rm d}\hat{x}} = \hbar G\left(\hat{a}^\dagger\hat{a} + \frac{1}{2}\right) = \hbar\frac{g_0}{x_{\rm ZPF}}\left(\hat{a}^\dagger\hat{a} + \frac{1}{2}\right), \tag{2.70}$$

which is consistent with Eq. (2.64). Note that the full Hamiltonian $\hat{\mathcal{H}}_{\rm sys}$ also includes terms that describe the external drives or baths, coupled to variables through the damping rates κ for the cavity modes and $\Gamma_{\rm m}$ for the mechanical modes. These effects are omitted from the Hamiltonian but will be formulated efficiently in the equation of motion by using Langevin equation and input-output theory.

Considering the field operators in the rotating frame of the input laser frequency $\omega_{\rm l}$, the equations of motion are obtained from Eq. (2.67) by using quantum Langevin equation:

$$\dot{\hat{a}}(t) = -\left[\kappa/2 - i\left(\Delta + G\hat{x}(t)\right)\right]\hat{a}(t) + \sqrt{\kappa_{\rm in}}\hat{a}_{\rm in}(t), \tag{2.71}$$

$$\dot{\hat{x}}(t) = \frac{\hat{p}(t)}{m_{\rm eff}}, \tag{2.72}$$

$$\dot{\hat{p}}(t) = -m_{\rm eff}\Omega_{\rm m}^2\hat{x}(t) - \Gamma_{\rm m}\hat{p}(t) + \hat{F}_{\rm opt}(t) + \hat{F}_{\rm th}(t). \tag{2.73}$$

For the cavity field, the coupling to the environment mainly arises from the input field $\hat{a}_{\rm in}(t)$, which has expectation value $\langle\hat{a}_{\rm in}(t)\rangle = \alpha_{\rm in}(t)$. The Brownian force $\hat{F}_{\rm th}(t)$ which comes from thermal fluctuations with mean value $\langle\hat{F}_{\rm th}(t)\rangle = 0$, and has spectral density given by [70]

$$S_{\rm F}^{\rm (th)}(\omega) = m_{\rm eff}\Gamma_{\rm m}\hbar\omega\coth\left(\frac{\hbar\omega}{2k_{\rm B}T}\right). \tag{2.74}$$

This is obtained at thermal equilibrium at temperature T. The Boltzmann constant is denoted by $k_{\rm B}$. Given that the phonon thermal occupation number is defined as $n_{\rm th}(\omega) = 1/\left(e^{\hbar\omega/k_{\rm B}T} - 1\right)$, we have $S_{\rm F}^{\rm (th)}(\omega) = m\Gamma_{\rm m}\hbar\omega\left(2n_{\rm th}(\omega) + 1\right)$ the magnitude of which is proportional to the number of phonons.

Similarly, we consider the cavity in the semiclassical regime and use the mean response of the operators to describe the system. Denoting the mean response of the operators as $\langle\hat{x}(t)\rangle \to x$, $\langle\hat{p}(t)\rangle \to p$ and $\langle\hat{a}(t)\rangle \to a$, which give the calculation of the average observable value of the system. It thus can be described by the classical equations of motion as follows:

$$\dot{a} = -\left[\kappa/2 - i\left(\Delta + Gx\right)\right]a + \sqrt{\kappa_{\rm in}}a_{\rm in}, \tag{2.75}$$

$$\ddot{x} = -\Omega_{\rm m}^2 x - \Gamma_{\rm m}\dot{x} + \frac{\hbar G}{m_{\rm eff}}|a|^2. \tag{2.76}$$

2.4.2 Mechanical and optical bistability

As we mentioned above, in an optomechanical system, the optical and mechanical oscillators are not independent of each other, they interact with each other via radiation pressure force. One can qualitatively picture the relation between them by imagining a

direct consequence: the radiation pressure force from the intracavity field influences the mirror, displaces it, and thus causes a shift of the cavity resonance. This shift can be more than a linewidth with a high enough intracavity power. However, the shift of the cavity resonance will lead to a decrease in the intracavity power and further a change in the radiation pressure force, which will again affect the displacement of the mirror. Such interaction between the optical and the mechanical oscillators ultimately results in the bistable behaviour and optical spring effect, which will be discussed in this and next section.

We firstly investigate the static solution of Eq. (2.75) and (2.76). With the condition $\dot{a} = 0$ and $\dot{x} = \ddot{x} = 0$, the solution at steady-state is obtained as

$$a_{\mathrm{s}} = \frac{\sqrt{\kappa_{\mathrm{in}}} a_{\mathrm{in}}}{\kappa/2 - i\left(\Delta + G x_{\mathrm{s}}\right)}, \tag{2.77}$$

$$x_{\mathrm{s}} = \frac{\hbar G |a_{\mathrm{s}}|^2}{m_{\mathrm{eff}} \Omega_{\mathrm{m}}^2}. \tag{2.78}$$

By inserting the expressions of intracavity power (Eq. (2.24)) and input power (Eq. (2.19)) into Eq. (2.77) and (2.78), we get the relationship between the displacement x_{s} and the intracavity power $P_{\mathrm{cav,s}}$ at steady-state, written as

$$x_{\mathrm{s}} = \frac{G \tau_{\mathrm{cav}}}{m_{\mathrm{eff}} \Omega_{\mathrm{m}}^2 \omega_{\mathrm{L}}} P_{\mathrm{cav,s}}, \tag{2.79}$$

and a cubic relation for x_{s},

$$x_{\mathrm{s}} \left[\kappa^2/4 + \left(\Delta + G x_{\mathrm{s}}\right)^2\right] = \frac{G \kappa_{\mathrm{in}} P_{\mathrm{in}}}{m_{\mathrm{eff}} \Omega_{\mathrm{m}}^2 \omega_{\mathrm{L}}}, \tag{2.80}$$

which is equivalent to $P_{\mathrm{cav,s}}$ since they are in direct proportion (Eq. (2.79)).

In this cubic equation, if the discriminant is less than zero, there is only one real root, indicating that the mechanical oscillator stays in the single-state regime. However, when the discriminant of the equation is greater than zero, it gives three different roots, where the largest and the smallest solutions are stable. As shown in Fig. 2.6(a), the middle one is unstable, because the slope $\mathrm{d}P_{\mathrm{in,norm}}/\mathrm{d}x_{\mathrm{s,norm}}$, is negative with these solutions, and not all the eigenvalues of the Jacobian matrix will be non-negative. The numerical solutions of the mechanical displacement (or intracavity power) as a function of input power under different cavity detuning are displayed. The cavity responses in Fig. 2.6(a) are all obtained with a red-detuning of the cavity, where we observe that three possible cavity configurations exist with certain input powers. One example of the modification from the mechanical displacement leading to bistable behaviour of a cavity is presented in Fig. 2.6(b). In the absence of the optomechanical interaction, the cavity response is in a Lorentzian shape (in blue). With a "movable" mirror, however, the Lorentzian response to the detuning changes with a shifted resonance (in orange). The dashed lines represent the unstable solution, which corresponds to the lighter section of each line in Fig. 2.6(a),

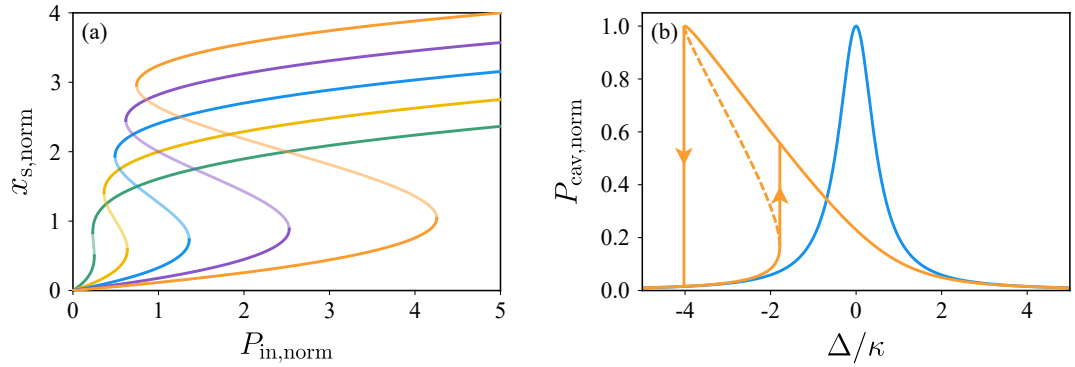

Figure 2.6: Effects of optomechanical bistability on a cavity. In the plots P_{cav} is normalised in terms of $P_{\mathrm{g}} = \hbar\omega_{\mathrm{l}}|a_{\mathrm{s}}|^2\big|_{Gx_{\mathrm{s}}=\kappa} = \kappa m_{\mathrm{eff}}\Omega_{\mathrm{m}}^2\omega_{\mathrm{l}}/G^2$, with which P_{cav} and P_{in} are normalised as $P_{\mathrm{g}}/\tau_{\mathrm{cav}}$ and $P_{\mathrm{g}}\kappa^2/4\kappa_{\mathrm{in}}$ respectively. The cavity detuning is in units of κ whereas displacement's unit is κ/G. Displacement as a function of input powers is plotted in (a), with detuning of $-\kappa$ (green), -1.5κ (yellow), -2κ (blue), -2.5κ (purple), -3κ (orange). The lighter section of each line represents the unstable solution of the displacement. In (b), the bistable behaviour of the cavity is given in orange. The numerical result of the normalised intracavity power is shown in a function of cavity detuning, with an input power $P_{\mathrm{in}} = P_{\mathrm{g}}\kappa^2/4\kappa_{\mathrm{in}}$. The blue line is plotted as a reference to show the cavity response without any mechanical coupling.

giving the regime where the cavity response behaves differently depending on the scanning directions.

For Eq. (2.77), it is also clear to see that the presence of the mechanical displacement modifies the intracavity field. For convenience, we normalise the intracavity photon number according to that on resonance ($n^{\max}$):

$$n_{\mathrm{norm}} = \frac{|a_{\mathrm{s}}|^2}{n^{\max}} = \frac{1}{1 + 4\left(\Delta + Gx_{\mathrm{s}}\right)^2/\kappa^2}, \tag{2.81}$$

where

$$n^{\max} = \frac{4\kappa_{\mathrm{in}}|a_{\mathrm{in}}|^2}{\kappa^2}. \tag{2.82}$$

We can then get the mean radiation pressure force from Eq. (2.70), by denoting $\langle\hat{a}^\dagger\hat{a}\rangle \to |a_{\mathrm{s}}|^2$,

$$F_{\mathrm{opt}}(x) \simeq \hbar G|a_{\mathrm{s}}|^2 = \frac{\hbar G n^{\max}}{1 + 4\left(\Delta + Gx\right)^2/\kappa^2}, \tag{2.83}$$

Integral of the radiation pressure force, we have the effective potential for the mechanical oscillator from the sum of the elastic ($F_{\mathrm{el}}(x) = -m_{\mathrm{eff}}\Omega_{\mathrm{m}}^2 x$) and the optical (Eq. (2.83))

force potential

$$\begin{aligned} V_{\mathrm{eff}}(x) &= -\int dx\,(F_{\mathrm{el}}(x)+F_{\mathrm{opt}}(x)) \\ &= \frac{1}{2}m_{\mathrm{eff}}\Omega_{\mathrm{m}}^2x^2-\frac{1}{2}\hbar\kappa n^{\max}\arctan\frac{2\,(\Delta+Gx)}{\kappa}. \end{aligned} \tag{2.84}$$

2.4.3 Dynamical backaction

In the previous section, we investigated the optomechanical system in the steady state or under the static condition. In this section, we will discuss the dynamic system with the optomechanical interaction. To simplify the calculations, we introduce the so-called "linearised" approximate description of cavity optomechanics with the assumption that the system fluctuates only slightly around its equilibrium point, thus we have

$$x=\bar{x}+\delta x,\quad a=\alpha+\delta a,\quad a_{\mathrm{in}}=\alpha_{\mathrm{in}}+\delta a_{\mathrm{in}}. \tag{2.85}$$

Substituting them into Eq. (2.75) and (2.76), the dynamical equations of the first-order read

$$\delta\dot{a} = -(\kappa/2-i\Delta)\,\delta a+iG\,(\alpha\delta x+\bar{x}\delta a)+\sqrt{\kappa_{\mathrm{in}}}\delta a_{\mathrm{in}}, \tag{2.86}$$

$$\delta\ddot{x} = -\Omega_{\mathrm{m}}^2\delta x-\Gamma_{\mathrm{m}}\delta\dot{x}+\frac{\hbar G}{m_{\mathrm{eff}}}\left(\alpha\delta a^*+\alpha^*\delta a\right). \tag{2.87}$$

We then apply the Fourier transform to solve the equations in the frequency domain, which yields the following set of equations:

$$[\kappa/2-i\,(\omega+\Delta+G\bar{x})]\,\delta a(\omega) = iG\alpha\delta x+\sqrt{\kappa_{\mathrm{in}}}\delta a_{\mathrm{in}}(\omega), \tag{2.88}$$

$$[\kappa/2-i\,(\omega-\Delta-G\bar{x})]\,\delta a^*(\omega) = -iG\alpha^*\delta x+\sqrt{\kappa_{\mathrm{in}}}\delta a_{\mathrm{in}}^*(\omega), \tag{2.89}$$

$$-\omega^2\delta x(\omega)+\Omega_{\mathrm{m}}^2\delta x(\omega)-i\Gamma_{\mathrm{m}}\omega\delta x(\omega) = \frac{\hbar G}{m_{\mathrm{eff}}}\left(\alpha^*\delta a(\omega)+\alpha\delta a^*(\omega)\right). \tag{2.90}$$

Replacing $\delta a(\omega)$ and $\delta a^*(\omega)$ in Eq. (2.90) with Eq. (2.88) and Eq. (2.89), we obtain

$$\left[\chi_{\mathrm{m}}(\omega)^{-1}+\Sigma_{\mathrm{opt}}(\omega)\right]\delta x(\omega)=F(\omega), \tag{2.91}$$

with

$$\chi_{\mathrm{m}}(\omega) = \left[m_{\mathrm{eff}}\left(\Omega_{\mathrm{m}}^2-i\Gamma_{\mathrm{m}}\omega-\omega^2\right)\right]^{-1}, \tag{2.92}$$

$$\Sigma_{\mathrm{opt}}(\omega) = \hbar|G\alpha|^2\left(\frac{1}{(\Delta+G\bar{x}+\omega)+i\kappa/2}+\frac{1}{(\Delta+G\bar{x}-\omega)-i\kappa/2}\right), \tag{2.93}$$

$$F(\omega) = \hbar G\sqrt{\kappa_{\mathrm{in}}}\left(\frac{\alpha^*a_{\mathrm{in}}(\omega)}{\kappa/2-i\,(\omega+\Delta+G\bar{x})}+\frac{\alpha a_{\mathrm{in}}^*(\omega)}{\kappa/2-i\,(\omega-\Delta-G\bar{x})}\right). \tag{2.94}$$

By writing in this way, we obtain an equation having the same structure as Eq. (2.49). Thus, $\chi_{\mathrm{m}}(\omega)$ can be recognised as the natural mechanical susceptibility, $\Sigma_{\mathrm{opt}}(\omega)$ denotes

the optical correction to the susceptibility and $F(\omega)$ is the radiation pressure fluctuation produced by laser shot noise. Therefore, the effective mechanical susceptibility is suggested as

$$\chi_{\rm eff}(\omega)^{-1} = \chi_{\rm m}(\omega)^{-1} + \Sigma_{\rm opt}(\omega), \tag{2.95}$$

and can be rewritten as

$$\chi_{\rm eff}(\omega) = \left[m_{\rm eff}\left(\omega_{\rm eff}^2 - \omega^2 - i\gamma_{\rm eff}\omega\right)\right]^{-1}. \tag{2.96}$$

This allows us to investigate the dynamics with the effective mechanical frequency, $\omega_{\rm eff}$, and the effective mechanical damping, $\gamma_{\rm eff}$, which are perturbed from the original parameters by adding a correction that is said to be the optical spring, as follows:

$$\begin{aligned}
\omega_{\rm eff}(\omega) &= \sqrt{\Omega_{\rm m}^2 + \frac{\Re(\Sigma_{\rm opt}(\omega))}{m_{\rm eff}}} \\
&= \sqrt{\Omega_{\rm m}^2 + \frac{\hbar|G\alpha|^2}{m_{\rm eff}}\left[\frac{\Delta + G\bar{x} + \omega}{(\Delta + G\bar{x} + \omega)^2 + \kappa^2/4} + \frac{\Delta + G\bar{x} - \omega}{(\Delta + G\bar{x} - \omega)^2 + \kappa^2/4}\right]}
\end{aligned} \tag{2.97}$$

$$\begin{aligned}
\gamma_{\rm eff}(\omega) &= \Gamma_{\rm m} + \frac{\Im(\Sigma_{\rm opt})}{m_{\rm eff}\omega} \\
&= \Gamma_{\rm m} + \frac{\hbar|G\alpha|^2\kappa}{2m_{\rm eff}\omega}\left[\frac{1}{(\Delta + G\bar{x} + \omega)^2 + \kappa^2/4} - \frac{1}{(\Delta + G\bar{x} - \omega)^2 + \kappa^2/4}\right]
\end{aligned} \tag{2.98}$$

In this perspective, rather than investigating the movable mirror independently and trying to figure out its interaction with the light field inside the cavity, we consider the optomechanical system as an extended oscillator, where the effects of radiation pressure force are included in the effective susceptibility as a correction term.

2.5 Photothermal interactions in an optomechanical system

For applications of mirrors, the surface shape is one of the most important parameters, which determines their employment and performance in experiments. The mirror surface geometry remains unchanged only under an ideal situation where the mirror is exposed to a uniform temperature change and the material is isotropic. However, in most realistic cases, the temperature change induced by the laser is inhomogeneous, which changes the mirror in size, radius and hence its focus. Thus, the mirror's behaviour with temperature change is critical in optical systems where a high sensitivity is required. In this section, we will introduce photothermal effects in optics, optical resonators, and further optomechanical systems.

2.5.1 Photothermal effects in optics

Photothermal effects in optics can be ignored in experiments where the optical field itself is not of interest and laser intensity is not huge. For very big mirrors, or large changes in temperature, for example, the equipments in LIGO where very high laser intensity is applied, a spatial change in thermal coefficient of expansion causes a surface distortion. With a uniform temperature bath, the anisotropy in expansion leads to an inhomogeneous change on the surface of the mirror. For most mirror materials, however, the anisotropy of thermal expansion $\Delta\alpha$ is on the order of a few percent, so this effect is only considered on large mirrors or very sensitive instruments, such as the optomechanical levitation setup discussed in the following chapters. In more common cases, if the laser is acting as the thermal bath, the distortion also comes from the spatial characteristics of the laser.

Moreover, the axial temperature gradient along the optical axis of the mirror from the surface to the interior also deforms the mirror surface by changing the optical radius R. The change in radius of curvature ΔR has a quadratic dependence on the radius, which is described as [71]

$$\Delta R = \frac{\alpha}{k} Q R^2, \tag{2.99}$$

where α and k denote the thermal coefficient of expansion and the thermal conductivity of the mirror material respectively. The heat flux per unit area Q produces the temperature gradient. The ratio α/k is the thermal distortion index of the mirror material which determines distortion due to the temperature change. To minimise it, a large thermal conductivity and a low thermal expansion coefficient are desired. For the glassy materials commonly used in mirrors, thermal conductivity varies little (ranging from about $1.1\,\mathrm{W\,m^{-1}\,K}$ for Pyrex to $1.6\,\mathrm{W\,m^{-1}\,K^{-1}}$ for Zerodur [71]), therefore the thermal expansion coefficient becomes critical when designing the mirror materials.

After a sudden change of the temperature at the mirror's surface, a temperature gradient is established from the centre of the surface to the edges. The surface temperature then decays with time with the heat transferring to the interior, where the temperature T_h rises up exponentially with time t:

$$T_\mathrm{h} = T\left[1 - \exp\left(\frac{-t}{\tau_\mathrm{h}}\right)\right], \qquad \tau_\mathrm{h} = \frac{h^2}{\pi^2}\frac{1}{k/\rho c_\rho}, \tag{2.100}$$

where the thickness of the mirror, or the distance from the surface is denoted by h. The density and the specific heat of the material are, respectively, written as ρ and c_ρ. T gives the surface temperature and τ_h denotes the thermal time constant of the mirror which is inversely proportional to the thermal diffusivity $k/\rho c_\rho$. Therefore, in the experiments where laser power is not changing, in order to minimise the time for the mirror to reach thermal equilibrium, a small thermal time constant and hence a large value of thermal diffusivity is desirable in mirror designs. With a cavity in an optomechanical system, however, a small time constant gives faster reactivity, which may induce other nonlinear

effects into the system. In the following sections, we use a simplified model to describe only the photothermal effects on optics and consider the property changes of mirrors only in one dimension.

2.5.2 Photothermal effects in an optical resonator

In an optical resonator, one of the most important parameters is the cavity length, which directly determines the resonance frequencies. In a common optical cavity when the temperature change on the mirror surface induced by the laser beam is not very large, the most significant effect resulting from the temperature rise is the photothermal displacement, or optical length change. Suppose that in a mirror the temperature relaxes towards the equilibrium point with a rate γ_{th}, we describe the temperature evolution with the differential equation as [72]

$$\dot{T} = -\gamma_{\mathrm{th}} \left(T - T_0 - \frac{\partial T}{\partial P_{\mathrm{cav}}} P_{\mathrm{cav}} \right), \tag{2.101}$$

where T_0 is the equilibrium temperature and γ_{th} is the relaxation rate of the joint photothermal effect. The quantity P_{cav} refers to the power of the heating laser, specifically the intracavity power when a cavity is under discussion. Considering the most significant effect manifested as the thermal expansion of the mirror materials, we assume that the photothermal displacement is linearly dependent on the temperature near the equilibrium, which yields

$$\dot{x}_{\mathrm{th}} = -\gamma_{\mathrm{th}} \left(x_{\mathrm{th}} + \frac{\partial x_{\mathrm{th}}}{\partial P_{\mathrm{cav}}} P_{\mathrm{cav}} \right). \tag{2.102}$$

Here we define the term $\partial x_{\mathrm{th}}/\partial P_{\mathrm{cav}}$ as the photothermal coefficient with SI unit $\mathrm{m\,W^{-1}}$, denoted by β:

$$\beta = \frac{\partial x_{\mathrm{th}}}{\partial P_{\mathrm{cav}}}. \tag{2.103}$$

This parameter quantifies the photothermal displacement response to the laser power. With a positive β, it is clear to see that the radiation power causes an increase of the photothermal displacement, physically, an expansion of the mirror materials, leading to a reduction of the effective optical length inside the cavity. Conversely, a negative β results in a decrease of photothermal displacement and hence an increase of the effective optical length. Note that for commonly used substrate materials, such as fused silica, sapphire, and BK7, the photothermal coefficient is usually positive.

The transient solution of Eq. (2.102) is easy to obtain when the cavity power does not evolve in time and has the following form

$$x_{\mathrm{th}} = x_1 e^{-\gamma_{\mathrm{th}} t} - \beta P_{\mathrm{cav}}, \tag{2.104}$$

where x_1 is determined by the initial condition. If the intracavity power that drives the photothermal displacement evolves with time, we can solve Eq. (2.102) in the frequency domain using the Fourier transform and we have

$$\dot{x}_{\rm th}(\omega) = \frac{\gamma_{\rm th}\beta P_{\rm cav}(\omega)}{i\omega - \gamma_{\rm th}}, \tag{2.105}$$

where we define the photothermal susceptibility $\chi_{\rm th} = (i\omega - \gamma_{\rm th})^{-1}$. This quantity is equivalent to the first-order pole approximation of the generalised photothermal interaction. Unlike the radiation pressure susceptivity (Eq. (2.96)) whose reciprocal is quadratic to ω, the reciprocal of photothermal susceptibility is linearly proportional to it.

It is important to mention that here we use the expansion of the mirror coating as an example to give the expression of photothermal displacement. This is because usually in a cavity it is dominant over other effects. Effects such as photothermally-induced refractive index change on a mirror coating also modify the effective optical length of the cavity, which may become prominent when the mirror is part of a high-sensitivity interferometer. Moreover, the thermal gradients along the optics axis and non-uniform spatial distribution of the heating source (a Gaussian beam, etc.) can cause distortion on the mirror surface, which may lead to a change in cavity modes and cavity dynamics. More investigation on photothermal effects will be given in Chapter 5.

2.5.3 Photothermal effects in an optomechanical system

We now consider photothermal effects in an optomechanical system. In the previous sections, we have given the dynamic equations of motion of the cavity with only radiation pressure as the interaction between the optical field and the oscillator. Recalling Eq. (2.66), and replacing the oscillator displacement x with the total displacement caused by radiation pressure force and the photothermal effect $x_{\rm th} + x_{\rm rp}$, we have

$$\omega_{\rm cav}(x_{\rm rp}, x_{\rm th}) \simeq \omega_{\rm cav} - G\left(x_{\rm rp} + x_{\rm th}\right), \tag{2.106}$$

By substitution of Eq. (2.102) into the equation of motion, Eqs. (2.75)-(2.76), for the optomechanical system, and also replacing x with $x_{\rm th} + x_{\rm rp}$, updated equations of motion with a photothermal coupling are thus obtained

$$\dot{a} = -\left[\kappa/2 - i\left(\Delta + G\left(x_{\rm rp} + x_{\rm th}\right)\right)\right] a + \sqrt{\kappa_{\rm in}} a_{\rm in}, \tag{2.107}$$

$$\ddot{x}_{\rm rp} = -\Omega_{\rm m}^2 x_{\rm rp} - \Gamma_{\rm m}\dot{x}_{\rm rp} + \frac{\hbar G}{m_{\rm eff}}|a|^2, \tag{2.108}$$

$$\dot{x}_{\rm th} = -\gamma_{\rm th}\left(x_{\rm th} + \beta\frac{\hbar G c}{2}|a|^2\right). \tag{2.109}$$

From the equations above, we have the equations for the system's steady state:

$$a_{\mathrm{s}} = \frac{\sqrt{\kappa_{\mathrm{in}}}a_{\mathrm{in}}}{\kappa/2 - i\left[\Delta + G\left(x^{\mathrm{s}}_{\mathrm{rp}} + x^{\mathrm{s}}_{\mathrm{th}}\right)\right]}, \tag{2.110}$$

$$x^{\mathrm{s}}_{\mathrm{rp}} = \frac{\hbar G|a_{\mathrm{s}}|^2}{m_{\mathrm{eff}}\Omega^2_{\mathrm{m}}}. \tag{2.111}$$

$$x^{\mathrm{s}}_{\mathrm{th}} = -\beta\frac{\hbar G c}{2}|a_{\mathrm{s}}|^2. \tag{2.112}$$

2.6 Optomechanical levitation

In the configurations where the oscillating component is mechanically clamped to a substrate or support, coupling of mechanical motion to the thermal disturbances is unavoidable. Extrinsic thermal fluctuations limit the optomechanical sensitivity, introducing decoherence which is harmful to achieving optomechanics in the quantum regime. Optical levitation, instead, by removing all mechanical contact with the surroundings, provides an environmental isolation scheme, which allows the full manipulation of the quantum state and mechanical frequency of the levitated particles via the optical fields [73, 74, 75, 76].

2.6.1 Levitation and control of microscopic objects in vacuum

In the last few decades, optically levitating nano- and micro-objects in vacuum has received increasing attention in areas ranging from fundamental quantum physics to commercial sensors. Attractive research directions have been unlocked by the many recent achievements, different cooling and controlling techniques have been used in various experimental schemes.

By levitating the particles and restricting the unwanted extrinsic interaction, a previously unattainable isolation from the environment can be obtained. The large masses and densities of the levitated objects provide high inertial sensitivities for acceleration and force measurement [77, 78, 79, 80]. The ability to couple the internal degrees of freedom, such as phonons, magnons and excitons, to the well-controlled external degrees of freedom makes levitation systems excel as force sensors that can be exploited in different fields. For example, a levitated particle that carries a charge responds to electric fields that can be designed as an electric sensor [81, 82, 83, 84, 85], objects carrying magnetic moments interact with magnetic fields and thus constitute magnetometers [86, 87], and more naturally, with high mass, the levitated particles are good candidates for gravitational sensing [88]. With the optical cavity-based and active- [89, 90, 91] or passive-feedback [92, 93, 94] techniques that have been developed for levitation in vacuum, the motion of dielectric levitated nanoparticles can be cooled into the quantum ground state [89, 90, 95], paving the way to the study of quantum limited sensing and detection.

Another distinctive characteristic of a levitation system is the high degree of control over both conservative dynamics and coupling to the environment. Levitated particles

are free to move with the existence of the external influences, allowing for precise control and coupling of the conservative motion [96, 97, 98], equilibrium position [99, 100, 101], and rotation degrees of freedom [102, 103, 104, 105] of the particles. Such techniques provide a means of engineering the quantum motional and rotational states of a levitated object [106]. Moreover, extending control to all degrees of freedom of a levitated particle is the key to reducing sources of noise and decoherence in the experimental systems to a fundamental minimum scale. This will enable studies in unexplored regimes of macroscopic quantum physics and the probing of weak forces, including the preparation of macroscopic quantum superpositions of objects composed of billions of atoms, detection of non-Newtonian gravity, and searches for new physics beyond the standard model [107].

The advances outlined above of levitated systems, especially the controllable isolation, have opened the door to the study of single-particle stochastic thermodynamics. The tunability of the coupling with the environment makes levitated systems an ideal platform to investigate equilibration [108] or underdamped Brownian motion in both linear [109] and nonlinear [110] regimes. It also provides a powerful tool in the study of nonequilibrium physics, such as the thermalisation of mesoscopic objects in vacuum as well as complex many-particle physics [111, 112, 113, 114].

2.6.2 Optical levitation of a microscopic mirror

Recent studies in levitating milligram-scale mirrors make optical levitation a promising technique in metrology, especially the detection of exceedingly small changes in gravitational force, and, more fundamentally, an excellent candidate to explore quantum and nonlinear effects in the macroscopic regime.

The first scheme of using a levitated mirror as one of the end mirrors of a Fabry-Pérot cavity is presented in a configuration where the mirror is levitated by an optical tweezer [66], in order to eliminate the dissipation and decoherence introduced by the mechanical support in traditional optomechanical systems. In this paradigm, an optical spring mirror with a dual-disk structure is suspended by the optical gradient force that is provided by two linearly polarised elliptical Gaussian beams of equal wavelength horizontally crossing each other. The mirror consists of a silica disc that is connected via a silica pillar to a disc mirror, which is acting as an end mirror for a vertical cavity. With such a geometry, the beams can be applied solely to the silica disc to avoid laser heating on the disk mirror.

However, optical tweezers require highly focused beams to create the optical trap, which limit the mass and the size of the trapped objects. Based on the calculation, the mirror levitated in this optical tweezer system can only have a mass up to the order of nanograms, which restricts further applications for levitation of heavier objects. Whereas later, with the proposals of a scattering-free tripod and sandwich of optical cavities, milligram-scale mirrors can be levitated [115], which enables the systems to reach the standard quantum limit theoretically.

The sandwich configuration gives the simplest possible optical levitation in which a macroscopic mirror is optically levitated by two vertical Fabry-Pérot cavities linearly aligned [116]. The levitated mirror is vertically positioned between the two fixed mirrors, acting as one of the end mirrors of both cavities with the upper and lower mirrors fixed. To achieve the stabilisation of the suspended mirror, the top cavity is set to be red-detuned and the bottom cavity uses a blue-detuned laser, to minimise the suspension thermal noise. This system is theoretically proposed to reach the standard quantum limit and can be developed experimentally to create macroscopic entanglement as well as test quantum mechanics in mesoscopic regime.

Another proposal for levitating the mirror using only radiation pressure force is the tripod configuration, where the forces are generated by the three intracavity optical fields and an optical potential well is formed to trap the upper mirror [67]. The tripod scheme is designed to provide stability in the horizontal direction when the gravitational force of the mirror is balanced by the radiation pressure vertically. A small perturbation to the gravitational acceleration will cause a displacement of the position of the levitated mirror, leading to the change of the intracavity fields.

The advantages of such a system in developing high precision metrology devices result from the ease of information readout from the output of the optical cavity, the high sensitivity of gravitational acceleration measurement, and being free of scattering which confines all information that photons carry into the cavity. Furthermore, the capability of interfacing the optical field with the gravitational force via the macroscopic mirror opens the possibilities to test quantum gravity theories, that attempt to integrate quantum mechanics and general relativity [117].

This proposal has been experimentally studied with a vertical Fabry-Pérot cavity where a free-standing mirror is acting as the top reflector of the cavity and is designed to be levitated by the intracavity field [40]. The nonlinear dynamics of the system are observed, including high-order sideband generation, optical bistability, parametric amplification, and the optical spring effect. This work focuses on this experimental setup as a test bed for the successful levitation in the tripod configuration. A rigorous investigation into the dynamics and the photothermal effects, the development of refined models, and a technique to cancel photothermal induced instability of the system will be included in the following chapters.

Chapter 3

Optomechanical Levitation System and Current Model

Optical levitation systems are interesting for their extreme environmental isolation, which offer unique tools for precise metrology, optomechanical coupling and preparation of mechanical quantum states [106]. In this chapter, we will investigate the experimental setup of the one laser levitation system and its nonlinear dynamics. we will also present the experimental results of the cavity response under different input powers and scan speeds, with which the effectiveness of the current model will be discussed.

3.1 Experimental setup

The particular system under consideration here is a vertical Fabry-Pérot cavity, where the top end mirror is free-standing on an Invar ($FeNi_{36}$) spacer, as shown in Fig. 3.1. The top mirror of the cavity is coated with Ta_2O_5 and SiO_2 bi-layers acting as a distributed Bragg reflector (presented in Fig. 3.1(c)), which provides a reflectivity as high as 99.992% on the curved side of a fused silica spherical cap. The mass of the levitated mirror studied here is 1.116 ± 0.003 mg with a radius of curvature of 25 mm, diameter of 3 mm, and thickness of around 50 µm. The optical power required in order to levitate a mass at this scale is around 1.6 kW, which is high enough to have detrimental effects on the mirror's surface. Due to a relatively small spot size, the intensity at the surface of the mirror can reach as high as $3\,\mathrm{MW\,cm^{-2}}$, which is 10^3 times higher than the intensity in the baseline LIGO interferometers, resulting in significant photothermal effects.

The bottom mirror is a conventional 1-inch concave mirror, with a high-reflectivity coating on a fused silica substrate. It is attached to a piezoelectric actuator which facilitates a linear scan of the cavity length and induces a detuning to the cavity. The whole cavity is approximately 80 mm long and is enclosed by a monolithic Invar case to reduce thermal fluctuations (Fig. 3.1(a)). A spacer on the top, which is fixed to the Invar case, has a hole with three small symmetric contact points to support the mirror when it is not lifted or levitated. This is designed to minimise Van de Waals forces sketched in Fig. 3.1(d). A 1050 nm Nd:YAG laser is coupled into the cavity via the bottom mirror,

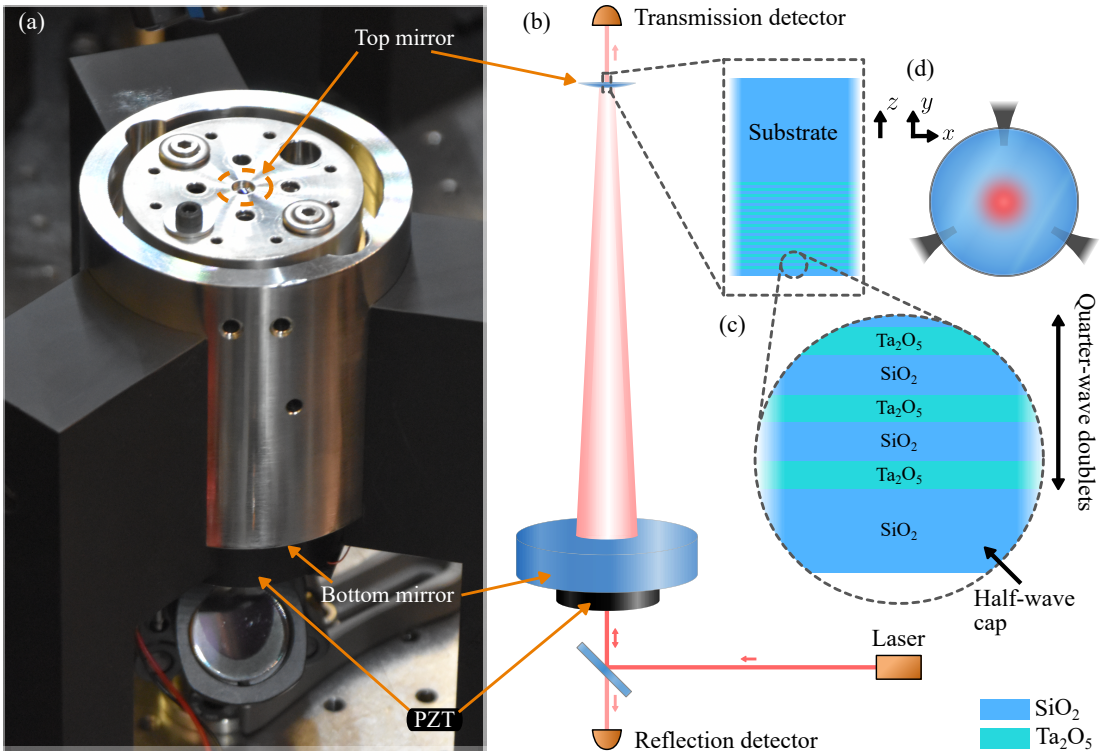

Figure 3.1: Experimental setup. (a) The vertical Invar cavity used in the levitation experiments. A small lightweight mirror is subject to the radiation pressure inside the cavity. The mirror is placed on the three small supporting points that are connected to the Invar case. The bottom mirror is attached to the piezoelectric actuator, which move together to induce the cavity detuning for a linear scan. (b) Schematic of the single laser levitation system. (c) High reflective mirror with Ta_2O_5 and SiO_2 bi-layers used as a distributed Bragg reflector. (d) Levitation mirror placed on the Invar mount.

producing an input light with up to 20 W of power.

When the radiation pressure exerted by the intracavity field is sufficiently strong to overcome the weight of the mirror, the mirror is lifted off one of the contact points. Thus the effective cavity length increases, and the intracavity field becomes blue-detuned compared to the resonance of the cavity. Note that at the scales involved, the "lifting" can be considered a normal translation (even if it is a rotation pivoted around the remaining contact points) because displacements of the centre of the mass is around only nanometers. Under these conditions the mirror enters the optical spring regime. The total of the radiation pressure and gravitational forces of the mirror provide a restoring force, creating the optical trap for the macroscopic mechanical oscillator in this levitation setup [67]. By moving the bottom mirror with the piezoelectric actuator, we change the resonance condition of the cavity, effectively changing the cavity detuning while keeping the laser frequency constant. To monitor the evolution of the intracavity field, we measure the reflected and the transmitted outputs of the cavity. The detailed design of the cavity and the optical layouts of the experiments can be found in Dr. Jinyong Ma's PhD thesis "*Photothermal Nonlinearity in Optical Cavities and Optomechanical Systems*" [118].

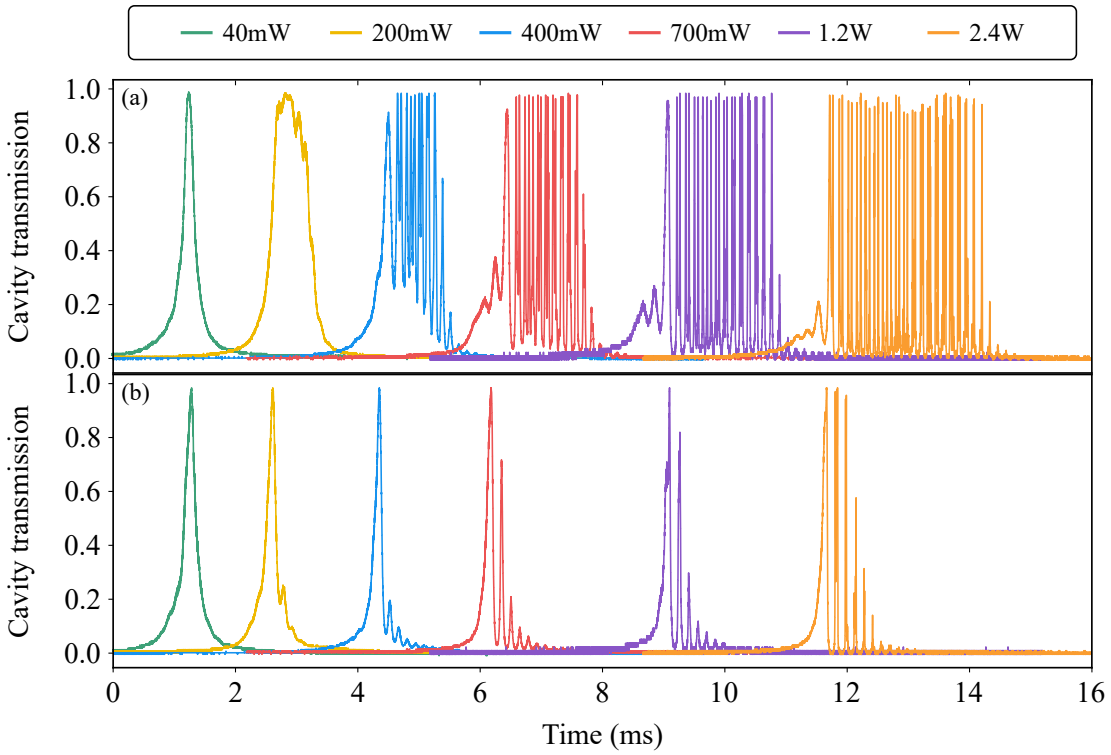

Figure 3.2: Cavity transmission under different input power. The results presented are taken with input power 40 mW (green), 200 mW (yellow), 400 mW (blue), 700 mW (red), 1.2 W (purple) and 2.4 W (orange), and under the same scan-speed of 1.105 µm s^{-1}. (a) shows transmission of the cavity during a downward scan, from red- to blue-detuned frequencies, showing the parametric amplification. (b) depicts the output of the cavity with an upward scan, from blue- to red-detuned frequencies. The cavity finesse is around 1970.

In this optomechanical system, photothermal interactions, manifested in different types, causes nonlinearity in the cavity dynamics. Photothermal expansion and refractive index change of the mirror coating due to thermal absorption are prominent effects which contribute to optical bistability and asymmetry in the cavity response to a linear scan. The excitation of the acoustic modes of the mirror causes it to vibrate, which further incorporates other effects that cause effective optical length change. In general, photothermal effects modify the system dynamics, introduce parametric gain to the cavity, and further amplify the oscillation which has been observed in the experiments. In the following sections, we will explore all these effects, interactions and dynamics.

The transmission of the cavity driven by different input powers are shown in Fig. 3.2, where (a) and (b) present the responses of the cavity under opposite scan directions, a downward scan (red- to blue-detuned frequencies) and an upward scan (blue- to red-detuned frequencies) respectively. Comparing the experimentally observed transmission output for various input powers, we show that the optical bistability is easier to observe at higher input power. A scan from red- to blue-detuning causes the resonance to follow along, leading to the "self-locking" of the cavity, which results in a broadening of the cavity resonance. In contrast, with an opposite scan from blue- to red-detuning, the cavity will

encounter the unstable region first and thus reacts by rapidly crossing over to the opposite side of resonance. This anti-locking mechanism leads to a much narrower Lorentzian profile of the cavity resonance. These phenomena are also implied by the equation of motions of the system and the simulation of its dynamics in the next section (see Fig. 3.3). As presented in Fig. 3.2, at low power, around 40 mW (green), the transmission is still very close to Lorentzian shape in both self-locking and anti-locking cases. However, with increased input power, cavity responses (at around 200 mW, shown in yellow) with the two opposite scan directions become asymmetric, especially for the self-locking regime. Cavity, with a finesse of approximately 1970, starts oscillating at about 300 mW (blue) under a scan-speed of $1.105\,\mu\mathrm{m\,s^{-1}}$. The mechanical oscillation results from the excitation of the acoustic modes of the mirror. This leads to the cavity crossing resonance multiple times during a single scan, which is shown in the cavity reflection and transmission traces.

3.2 Equation of motion

A simple model to describe the effective photothermal displacement in a cavity assumes a relaxation linearly proportional to the optical power [72, 119]. This empirical law originates from a single-pole approximation of the full thermo-elastic response of the mirror [120] in the case of photothermal expansion. Despite its simplicity, this equation proved its success in predicting the complicated dynamical behaviour of optomechanical cavities under the regime where the interaction between intracavity field and the mirror is weak [40].

The equations of motion for the system in the rotating frame of the cavity resonant frequency are:

$$\dot{a} = \left[-\kappa/2 + i(\Delta + G(x_{\mathrm{lev}} + x_{\mathrm{th}} + x_{\mathrm{ac}}))\right] a + \sqrt{\kappa_{\mathrm{in}}}\, a_{\mathrm{in}}, \tag{3.1}$$

$$\dot{x}_{\mathrm{th}} = -\gamma_{\mathrm{th}}(x_{\mathrm{th}} + \beta_{\mathrm{th}} P_{\mathrm{opt}}(a)), \tag{3.2}$$

$$\ddot{x}_{\mathrm{ac}} = -\gamma_{\mathrm{ac}}\dot{x}_{\mathrm{ac}} - \omega_{\mathrm{ac}}^2 x_{\mathrm{ac}} + F_{\mathrm{opt}}(a)/m_{\mathrm{ac}}, \tag{3.3}$$

$$\ddot{x}_{\mathrm{lev}} = \begin{cases} -\gamma_{\mathrm{lev}}\dot{x}_{\mathrm{lev}} & \text{when supported,} \\ -\gamma_{\mathrm{lev}}\dot{x}_{\mathrm{lev}} + (F_{\mathrm{opt}}(a) - F_{\mathrm{g}})/m & \text{when not supported,} \end{cases} \tag{3.4}$$

where the modification of the effective optical length is separated into three different entities: acoustic (x_{ac}), centre-of-mass (x_{lev}) and photothermal (x_{th}) displacements. These dynamic equations characterise the experimental system in the classical limit. The evolution of the optical field is shown as Eq. (3.1). The amplitude of the driving field is a_{in}, coupling through the input mirror at a rate κ_{in}. The imaginary part is the oscillatory term (normally at the optical frequency, but in the rotating frame it is described by the detuning of the cavity). The total losses are described by κ (with $\kappa > \kappa_{\mathrm{in}}$), which defines the decay rate of the cavity. The evolution of the amplitude of the intracavity field a depends on the shift of the centre of the mass x_{lev} caused by the radiation pressure force,

the displacement of the mirror's surface following vibrations of acoustic mode x_{ac}, and the difference of the cavity length due to total photothermal effects x_{th}. The detuning of the cavity is defined as $\Delta = \omega_{\mathrm{l}} - \omega_{\mathrm{opt}}$, where ω_{l} and ω_{opt} are angular frequencies of the optical field and the cavity resonance respectively. The coefficient $G = \omega_{\mathrm{opt}}/L_{\mathrm{cav}}$ is the optomechanical coupling strength between the mirror and the intracavity field, where L_{cav} is the length of the cavity.

Equation (3.2) gives the empirical model of photothermal effects. The thermal relaxation rate γ_{th} and the susceptivity coefficient β_{th} depend on the properties of the mirror material and its absorption coefficient. There are several ways in which photothermal effects can influence the cavity [121]. One way is thermal expansion: by absorbing optical power, the coating and substrate of the mirrors can expand and cause a reduction in cavity length. Another possibility is the thermo-optic effect, where the refractive index of a material is modified due to a variation in temperature, which changes the effective optical path within the cavity. With this model, the photothermal effects are merged and described as one collective displacement, which conceals the detail of how different photothermal effects interact with each other and with the cavity. The amalgamation, however, provides convenience for us to analyse the impact of photothermal effects on the cavity dynamics. Note that the susceptivity coefficient β_{th} can be positive or negative depending on the empirical effect that is photothermally induced, effectively shortening or lengthening the cavity. For example, if the refractive index change in the mirror coating is significant, the thermo-optic effect dominates, causing an increase in the effective cavity length. If the mirror material has a negative expansion coefficient, an increase in cavity length will also occur. This, however, is a rare scenario that is not normally observed in ordinary substrate materials.

The evolution of the centre of mass of the mirror is described in Eq. (3.4). The radiation pressure force $F_{\mathrm{opt}} = \hbar G|a|^2 = 2P_{\mathrm{opt}}/c$ could be calculated with the intra-cavity power P_{opt} and the speed of light c. The gravitational weight of the mirror is denoted as $F_{\mathrm{g}} = mg$, where g is free-fall gravitational acceleration and m is the total mass of the mirror. When there is sufficient power in the cavity, the radiation pressure force can lift the mirror above its supporting stand. The net force acting on the mirror is given by the balance of radiation pressure and its weight. Otherwise, when the intracavity power is not strong enough to lift the mirror, the full weight is absorbed by the reactionary forces of the stage and hence the net force becomes 0. The forces on the mirror may also excite the natural vibrational modes of the mirror. These are described by an "acoustic" degree of freedom, which behaves as a harmonic oscillator of frequency ω_{ac} and damping γ_{ac}, described in Eq. (3.3). The effective mass of this acoustic mode, m_{ac}, is generally a fraction of gravitational mass of the mirror ($m_{\mathrm{ac}} < m$). Here we have to emphasise that the force needed to lift the mirror is not generally equivalent to the gravitational weight of the mirror but greater, as the Van der Waals interaction and other static forces work against the radiation pressure as well. Also, in order to operate the system in an off-resonance detuned regime for the optical spring trap, a higher intensity of intracavity

field is needed. The dissipation coefficient of the centre-of-mass motion $\gamma_{\rm lev}$ is considered different from that of the acoustic mode $\gamma_{\rm ac}$ due to the fact that the former is mostly caused by air viscosity, whereas the latter by internal friction.

3.3 System dynamics

The parameters used in the model for simulations are inferred from the experimental results, which we list here once again: $L = 80\,\mathrm{mm}$, $m = 1.116\,\mathrm{mg}$, $m_{\rm ac} = 0.38\,\mathrm{mg}$, $\omega_{\rm ac} = 2\pi \times 28.6\,\mathrm{kHz}$, $\gamma_{\rm ac} = 2\pi \times 30\,\mathrm{Hz}$, $\gamma_{\rm lev} = 2\pi \times 50\,\mathrm{Hz}$, $\kappa_{\rm in} = 2\pi \times 220\,\mathrm{kHz}$, $G = 2\pi \times 3.6\,\mathrm{MHz\,nm^{-1}}$. The cavity decay rate κ used is different from one simulation to the other due to the difference in measured cavity finesses from different days. Thermal relaxation rate $\gamma_{\rm th}$ and susceptivity coefficient $\beta_{\rm th}$ are calculated by fitting the model to the experimental data. Differences in finesse change these quantities between various results presented. Note that in experiments conducted the radiation force never reached a threshold that the top mirror can be lifted, so we restrict Eq. (3.4) to the case *when supported*. With the initial condition $x_{\rm lev} = 0$, we have the derived result $\dot{x}_{\rm lev} = \ddot{x}_{\rm lev} = 0$ for all times, which gives simplified dynamical equations of the system where the modification of the effective optical length only comes from the acoustic and the photothermal displacement. Thus, we introduce the momentum of the effective mass of the acoustic mode $p_{\rm ac}$, and rewrite them as

$$\begin{aligned}
\dot{a} &= \left[-\kappa/2 + i(\Delta + G(x_{\rm th} + x_{\rm ac}))\right] a + \sqrt{\kappa_{\rm in}} a_{\rm in}, && (3.5)\\
\dot{a}^* &= \left[-\kappa/2 - i(\Delta + G(x_{\rm th} + x_{\rm ac}))\right] a^* + \sqrt{\kappa_{\rm in}} a^*_{\rm in}, && (3.6)\\
\dot{x}_{\rm th} &= -\gamma_{\rm th}(x_{\rm th} + \beta_{\rm th} P_{\rm opt}(a)), && (3.7)\\
\dot{x}_{\rm ac} &= p_{\rm ac}/m_{\rm ac}, && (3.8)\\
\dot{p}_{\rm ac} &= -\gamma_{\rm ac} p_{\rm ac} - m_{\rm ac}\omega_{\rm ac}^2 x_{\rm ac} + \hbar G|a|^2. && (3.9)
\end{aligned}$$

3.3.1 Optical bistability in the levitation system

Setting the time derivatives in Eq. (3.5)-(3.9) to zero, we obtain the equation to solve the amplitude of the intracavity field in the steady state, which is written as

$$\begin{aligned}
\left[G\left(-\beta_{\rm th}\frac{c}{2}\hbar G + \frac{\hbar G}{m_{\rm ac}\omega_{\rm ac}^2}\right)\right]^2 \left(|a|^2\right)^3 + 2\Delta G\left(-\beta_{\rm th}\frac{c}{2}\hbar G + \frac{\hbar G}{m_{\rm ac}\omega_{\rm ac}^2}\right)\left(|a|^2\right)^2 \\
+ \left(\kappa^2/4 + \Delta^2\right)|a|^2 - \kappa_{\rm in}|a_{\rm in}|^2 = 0. \qquad (3.10)
\end{aligned}$$

The steady-state solutions of the intracavity power as a function of effective detuning, solved with the current model, are illustrated in Fig. 3.3(a). The intracavity power at the resonance ($\Delta = 0$) is proportional to the input power ($a_{0,\,\rm res} = 2\sqrt{\kappa_{\rm in}} a_{\rm in}/\kappa$). With higher input power, the cavity obtains higher intracavity power. To show the dynamics of the cavity in a clearer picture, the results are normalised to the intracavity power for each

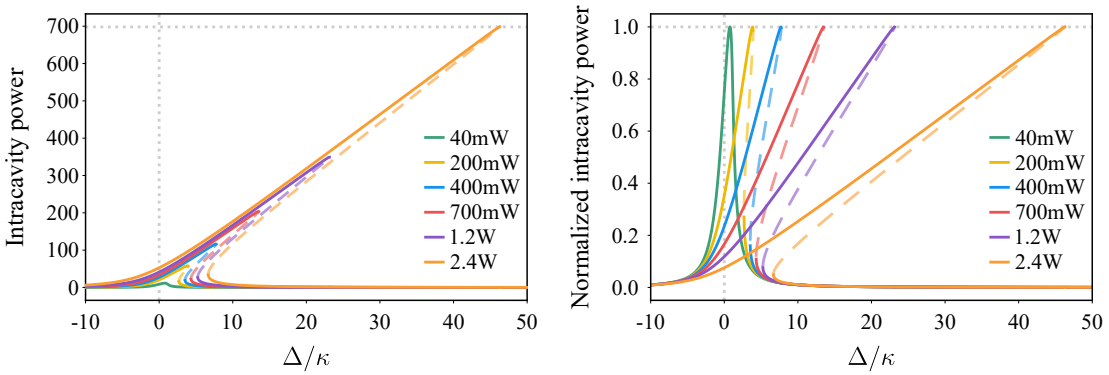

Figure 3.3: Cavity response as a function of detuning for the system driven by various input powers, showing optical bistability as a result of the photothermal interaction. The intracavity power and their normalised results are shown in (a) and (b) respectively. The Optically unstable solutions, plotted in dashed lines, are inaccessible steady-state solutions. Parameters used for the plots are $\kappa/2\pi = 950\,\mathrm{kHz}$, $\gamma_{\mathrm{th}}/2\pi = 426\,\mathrm{Hz}$, and $\beta_{\mathrm{th}} = 9.3\,\mathrm{pm\,W^{-1}}$.

of the curves at resonance ($\Delta = 0$), shown in Fig. 3.3(b). Optically unstable solutions, plotted in dashed lines, are inaccessible steady-state solutions.

With low input laser power ($P_{\mathrm{in}} = 40\,\mathrm{mW}$), the cavity response is nearly a Lorentzian shape (in green). However, as the input power sent into the cavity becomes higher, the cubic equation Eq. (3.10) yields three roots, a signature of bistable behavior. As shown in Fig. 3.3, the cavity response becomes more asymmetric, and resonance is shifted toward the blue-detuned side where two stable states (solid curves) and the unstable state (dashed curves) occur, which indicates an opposite bistable regime compared to the case with only radiation pressure interaction. That is because in our system, as the levitation is not considered and the mechanical interaction is induced only by the acoustic vibration of the mirror, photothermal effects dominate the optical length modification of the cavity. Unlike the mechanical displacement, where a higher intracavity power provides a stronger radiation force to push the mirror away, the photothermal displacement shortens the effective optical length as suggested by Eq. (3.7). As far as photothermal expansion is considered, the material of the mirror has a positive β_{th}. It is important to note that here the detuning of the cavity is the difference between the input laser frequency and the cavity resonance without any photothermal or mechanical modification, whereas the effective detuning used in Fig. 3.4 gives the difference between the laser frequency and the modified cavity resonance frequency.

3.3.2 Photothermal modification of optical spring

With the picture of optical bistability, only the dynamical picture of the optical fields (transmission, reflection and intracavity fields) at static steady-state can be described. The full dynamic evolution must account for the change of the elements such as the buildup of oscillations due to the positive restoring force and possible antidamping from a

negative effective viscous coefficient. Therefore we use the Jacobian matrix obtained from the linearisation of Eq. (3.1)-(3.4) to analyse the system bistability:

$$M_{\mathrm{J}} = \begin{bmatrix} -\kappa/2 + i\Delta_{\mathrm{eff}} & 0 & iG\alpha & iG\alpha & 0 \\ 0 & -\kappa/2 - i\Delta_{\mathrm{eff}} & -iG\alpha^* & iG\alpha^* & 0 \\ -\gamma_{\mathrm{th}}\beta_{\mathrm{th}}c\hbar G\alpha^*/2 & -\gamma_{\mathrm{th}}\beta_{\mathrm{th}}c\hbar G\alpha/2 & -\gamma_{\mathrm{th}} & 0 & 0 \\ 0 & 0 & 0 & 0 & 1/m_{\mathrm{ac}} \\ \hbar G\alpha^* & \hbar G\alpha & 0 & -m_{\mathrm{ac}}\omega_{\mathrm{ac}}^2 & -\gamma_{\mathrm{ac}} \end{bmatrix}, \tag{3.11}$$

where $\alpha = \sqrt{\kappa_{\mathrm{in}}}\langle a_{\mathrm{in}}\rangle / (\kappa/2 - i\Delta_{\mathrm{eff}})$ gives the steady-state value of the amplitude of the intracavity field. The effective detuning is $\Delta_{\mathrm{eff}} = \Delta + G(\langle x_{\mathrm{th}}\rangle + \langle x_{\mathrm{m}}\rangle)$. The angled brackets denote steady-state values for the respective degrees of freedom.

The dynamical system information is contained in the eigenvalues of this matrix, which shows how the natural damping and frequency of the acoustic mode are modified by both the photothermal interaction and radiation pressure. The real parts of the eigenvalues indicate the damping (or antidamping) coefficients of the system, thus only when the real parts of all eigenvalues of the Jacobian matrix are negative the system can be considered stable. The imaginary parts correspond to the steady-state eigenfrequencies in the system. The optical modification of these mechanical constants corresponds to a generalised optical spring effect, showing similar phenomena to optomechanical systems where a pure radiation pressure force modifies the mechanical susceptibility. Therefore, it is rather important to illustrate the effective oscillator frequency ω_{eff} and damping rate γ_{eff} in the investigation of the system dynamics. The effective resonator frequency and damping rate are obtained as

$$\omega_{\mathrm{eff}} = \Im\{\mathrm{eig}(M_{\mathrm{J}})\}, \tag{3.12}$$

$$\gamma_{\mathrm{eff}} = -2\Re\{\mathrm{eig}(M_{\mathrm{J}})\}, \tag{3.13}$$

where $\Im$ is the imaginary part and $\Re$ is the real part of the eigenvalue of the Jacobian matrix. The effects of the optical interaction on the natural acoustic frequency and damping rate of the oscillator are shown in Fig. 3.4. Together with Fig. 3.3, a rigorous analysis of the experimental observation can be conducted.

The parametrically amplified oscillation emerges in the red-detuned regime (negative effective detuning), which corresponds to a negative effective damping as shown in Fig. 3.4(b). When the average detuning imposed by the external scan goes from red to blue (downward scan of piezo), before it reaches the resonance, the effective detuning stays in the red-detuned regime and the oscillation is continuously undergoing parametric gain, leading to a further enhancement of the amplified oscillation. These effects are induced by the photothermal interaction between the laser and the levitated mirror, which get stronger with higher intracavity power. As shown in Fig. 3.3, with higher input power (intracavity power) the bistable behavior becomes more obvious. Intuitively, one can imagine a scenario where the top mirror expands inwards due to the thermal absorption and the

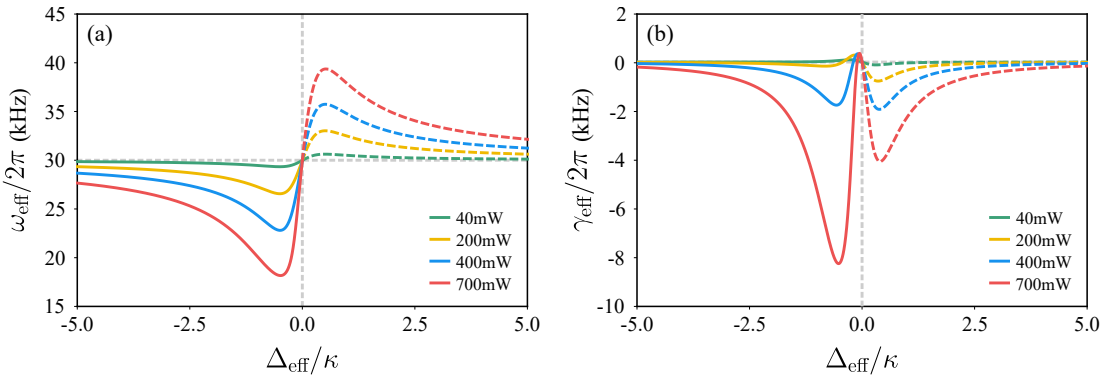

Figure 3.4: Backaction of radiation pressure and photothermal effects in the optomechanical system. Plots (a) and (b) show the modification of the oscillation's frequency and damping due to optical back action respectively, when the cavity is driven by the input powers of 40 mW (green), 200 mW (yellow), 400 mW (blue) and 700 mW (red). The parameters are plotted as a function of the effective detuning $\Delta_{\rm eff}$. The dashed lines give the optically unstable solutions, which correspond to the inaccessible steady-state solutions in Fig. 3.3. With no back action (gray), $\omega_{\rm eff} \equiv \omega_{\rm ac}$ and $\gamma_{\rm eff} \equiv \gamma_{\rm ac}$ at all detunings. Other parameters inserted into the Jacobian matrix for the simulation are same as the values used for Fig. 3.3.

bottom piezoelectric actuator is scanning downwards to change the detuning. In this case, the expansion of the top mirror compensates for the detuning induced by the downward travel of the bottom mirror. In the static picture, this prolongs the cavity residing in the red detuning regime and results in a self-locking response. However, as soon as the scan detuning falls on the opposite side of the resonance, the cavity jumps to the one stable state regime which is relatively far away from the resonance and the acoustic mode turns quiescent again. When scanning in the opposite direction (from blue to red), the oscillations are also excited but on the right-hand side of the traces (Fig. 3.2(b)). In this case, since the cavity jumps too quickly to the next stable state when scanning across the resonance, there is no sufficient time for the oscillation to develop significantly.

Another interesting phenomenon with the photothermally induced modification of the optical spring effect can be seen in Fig. 3.4(a). The oscillation frequency of the resonator decreases with a small red detuning of the resonance. With higher driving power, this reduction in the frequency becomes more significant. Considering a downwards (red- to blue-detuned) scan of the cavity around the resonance, an increasing oscillation frequency should be observed. This is shown in the experimental results presented in Fig. 3.7(c), by analysing the data in the frequency spectrum and tracking the time evolution of the transmission.

3.3.3 Excitation of acoustic modes

In Fig. 3.5, the cavity response corresponding to different scan speeds is presented. This shows that the excitations are easier to observe when the scan speed is slow enough for a full build-up of the oscillation, i.e., a situation that is closest to steady-state evolution.

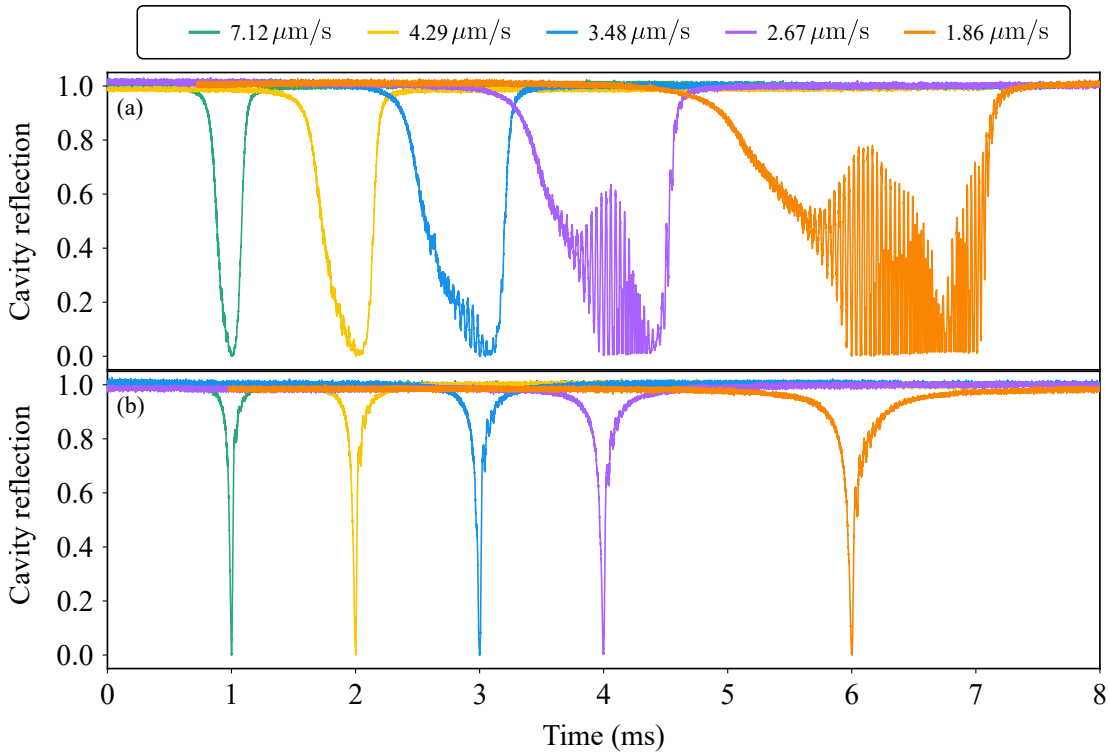

Figure 3.5: Cavity reflection with scan-speeds of $7.12\,\mu\mathrm{m\,s^{-1}}$ (green), $4.29\,\mu\mathrm{m\,s^{-1}}$ (yellow), $3.48\,\mu\mathrm{m\,s^{-1}}$ (blue), $2.67\,\mu\mathrm{m\,s^{-1}}$ (purple) and $1.86\,\mu\mathrm{m\,s^{-1}}$ (orange). The results are taken with the same input power of 495 mW. (a) Reflection of the cavity during a downward scan, from red- to blue-detuned frequencies. With a slower scan speed, the oscillations linked to the excitation of acoustic modes of the levitated mirror are parametrically amplified by the photothermal effects. (b) Reflection of the cavity with an upward scan, from blue to red detuning. The cavity finesse is around 2850.

Experimental results of the reflection of a cavity that has a finesse of around 2850 and is driven by an input power of 495 mW are given in the figure. The reflection signal during a downwards scan (from red- to blue-detuned frequencies) and an upwards scan (from blue- to red-detuned frequencies) are shown in Fig. 3.5(a) and (b) respectively. From left to right, the traces are the experimental results with the scan speed ranging from $7.12\,\mu\mathrm{m\,s^{-1}}$ to $1.86\,\mu\mathrm{m\,s^{-1}}$.

With an input power of 495 mW the cavity tends to self-lock in the red-detuning regime. The traces show a broadened and asymmetric Lorentzian profile when the scan speed is high ($7.12\,\mu\mathrm{m\,s^{-1}}$), whereas it encounters the unstable state first by approaching from the opposite direction where a narrowed Lorentzian shape appears. When the scan speed is lower ($4.29\,\mu\mathrm{m\,s^{-1}}$ and $3.48\,\mu\mathrm{m\,s^{-1}}$), oscillations start to occur in the self-locking responses. This is because the cavity length change induced by the downwards scanning slows down, allowing the cavity to stay in the red-detuning regime longer and thus giving more time for the cavity's response to the parametric gain that results from photothermal effects. Applying even lower scan speeds ($2.67\,\mu\mathrm{m\,s^{-1}}$ and $1.86\,\mu\mathrm{m\,s^{-1}}$) enables the stronger parametric amplification of photothermally induced oscillation. Small oscillations

have also been observed in the anti-locking regime. We notice that the oscillation happens in the different side of the traces in Fig. 3.5(a) and (b). This is because the scan directions are opposite, but the negative damping only occurs in the steady-state red-detuning regime. Therefore, when scanning upwards, only until the average detuning imposed by the external scan passes the resonance, the cavity enters the red-detuned regime and thus the cavity starts oscillating. After crossing the resonance, however, the cavity jumps too quickly to the next stable state, giving very limited time for the oscillation to develop significantly.

3.4 Ineffectiveness of the current model

In this section, we investigate the effectiveness of the existing model. We show that this model provides a faithful picture of the dynamics of the levitation system in the regime of lower input power or faster scanning speed, where oscillation is not observed on cavity transmission. In the scenario of higher input power and when the amplified oscillation is involved, the model becomes less reliable due to the ineffective fitting for the oscillation duration. This is mainly caused by the simplification of modelling the photothermal effects where different photothermal effects are combined. Because the system is operated in a regime where photothermal effects are the major interaction that introduces and further enhances the parametric gain that can destabilise the system. This issue will be addressed in Chapter 5.

In order to verify the accuracy of the model, we first compare the simulation results

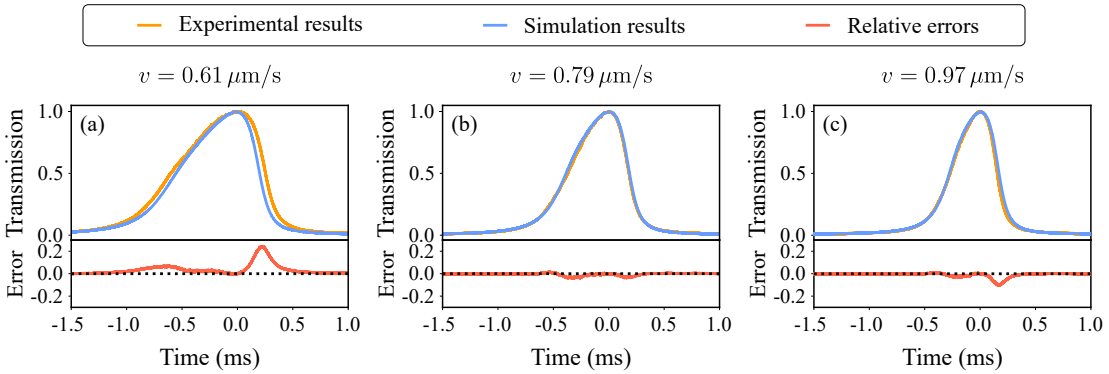

Figure 3.6: Simulation and experimental results of the cavity driven by the low input power. The normalised transmissions from experiments under different scan speeds are shown in orange (finesse = 2850). The simulation results (blue) for the cavity with scan speeds of $0.61\,\mu\mathrm{m\,s^{-1}}$, $0.79\,\mu\mathrm{m\,s^{-1}}$ and $0.97\,\mu\mathrm{m\,s^{-1}}$ are given in (a), (b) and (c) respectively. With lower scan speed, the cavity transmission becomes more asymmetric and the shifted Lorentzian response broadens. The simulation successfully fits all these features, which can be inferred from the error given in red. Here, we calculate error with the ratio of the difference between simulation and experimental data to the experimental data. The parameters used in simulation are: $\kappa = 2\pi \times 658\,\mathrm{kHz}$, $\gamma_{\mathrm{th}} = 2\pi \times 450\,\mathrm{Hz}$, $\beta_{\mathrm{th}} = 9\,\mathrm{pm\,W^{-1}}$.

with experimental results in the low-power regime. Experimental (orange) and simulation (blue) results of the normalised intensity of cavity transmission when the system is driven by 93 mW input power are shown in Fig. 3.6. The traces are aligned at their maximum. From left to right, we present the system under different scan speeds from 0.61 µm s^{-1} to 0.97 µm s^{-1}. The difference between the experimental and the simulation results are shown as error in red curves. Comparing the three traces with different scan speeds, it is easy to see that with higher speed (Fig. 3.6(c)) the transmission has a more Lorentzian-shaped resonance, as we mentioned in the previous sections. With lower scan speed (Fig. 3.6(a)), however, the traces are broadened, because photothermal effects modify the response blue-detune the resonance proportionally to the intracavity power, therefore dragging the maximum cavity output forward in the scan. These features are well simulated by the model in this power regime, which is also indicated by the errors given in Fig. 3.6.

With the cavity driven by a laser with high power, however, this model loses reliability. Applying the simulation at an input power of 2.75 W as an example, we give a detailed analysis including time evolution as well as the frequency spectrum, presented in Fig. 3.7. It shows that a high input power leads to a long self-locking response which carries multi-frequency oscillations. Fig. 3.7(e) gives the frequency spectrum of the experimental and simulation results. The mechanical oscillation of 28.6 kHz is excited and parametrically amplified around 0.3 ms after the cavity starts oscillating. The double of the first-order effective frequency is higher than the expectation, which is due to the cavity crossing the resonance twice within one vibration. Because the amplitude of the oscillation has been amplified significantly, this doubled frequency stands out from other frequencies in the spectrum. This oscillation also becomes more obvious in the anti-locking regime where, as we mentioned earlier, there is no sufficient time for it to develop.

Even though the existing model of the system with its dynamic equations simulates some of the cavity behaviours such as the oscillation frequency and the excitation of the acoustic modes with high input power, other important features of the cavity response are not well described. The most important feature is the oscillation duration. We can see from Fig. 3.7(b) that the oscillation time in the simulation is only half as long as that in the experiments. This flaw is also found in the anti-locking regime, where the oscillation damps very quickly in the simulation while the experimental data gives a much slower damping (Fig. 3.7(a)). It is important to mention that simply increasing the photothermal susceptivity β_{th} of the joint photothermal effect in the model can also extend the oscillation duration of the cavity response at this power regime. But it will also change the photothermal interaction strength at lower power regime, leading to discrepancies between the model and the experiment, which is discussed in detail in Chapter 5 (section 5.5).

Another important feature that the simulation fails to manifest is the build-up of the oscillation in the beginning of the scan. In experiments, the intracavity power rises up more slowly (compared to the simulations) before the oscillation starts. The amplitude of the oscillation is then amplified gradually. In contrast, during the simulation the intracavity power level rises faster with the scan and after oscillation occurs it is immediately and

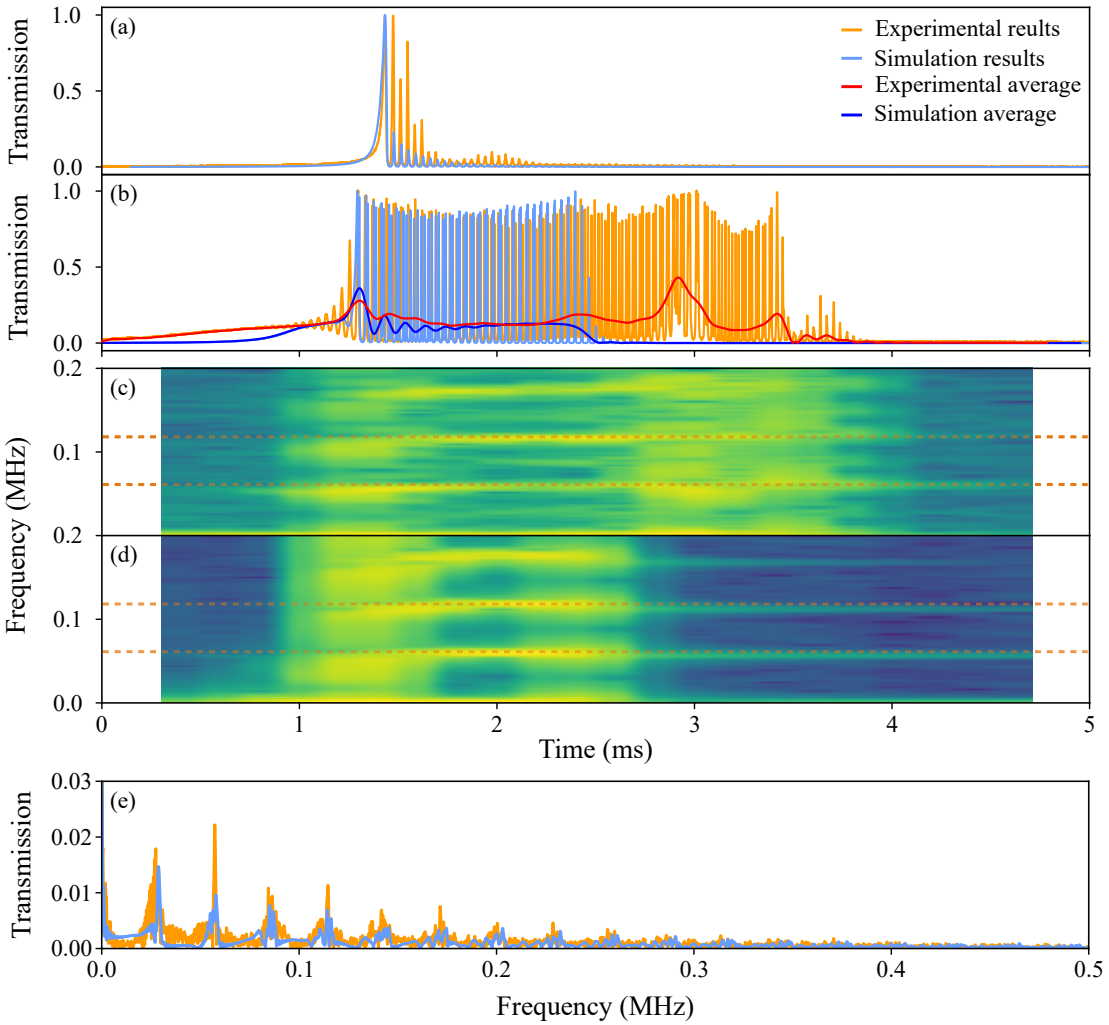

Figure 3.7: Experimental results and simulation for the system driven by a high power input laser. The orange curves in (a) and (b) are, respectively, the normalised transmissions of anti-locking and self-locking cavity response at an input power of 2.75 W with a scan speed of 2.67 $\mu m\,s^{-1}$ (finesse = 2550). Simulations (blue) of the system with the existing model are also presented in (a) and (b). In order to compare the simulations to the experimental results, a lowpass Butterworth filter is applied to both the experimental (red) and simulation (blue) results to get the average of the self-locking cavity responses. The frequency analysis is also presented. (c) and (d) are frequency evolution of the experimental and simulation results respectively, where orange dashed lines emphasise the acoustic modes frequencies of interest. Using the orange dashed lines as references, we show that the oscillation frequency is changing slightly, which is modulated by the photothermal effects as suggested by Fig. 3.4. (e) The frequency spectrum of the experimental and simulated transmission. The values that used for simulation are: $\kappa = 2\pi \times 735\,kHz$, $\gamma_{th} = 2\pi \times 450\,Hz$, $\beta_{th} = 9\,pm\,W^{-1}$.

dramatically amplified. This is also shown in Fig. 3.7(c) and (d).

3.5 Conclusion

In this chapter, we presented our optomechanical levitation setup and discussed the experimental results with different scan speeds and different input power. We showed that with a higher input power or a slower scan, the cavity show more obvious bistability. Photothermal interaction causes parametrically amplified oscillation to the cavity, which results in an impairment of the system. We also investigated the dynamics of the system with the existing model and discussed the photothermal modification of the effective frequency and damping of the oscillation. This model gives a faithful simulation when the cavity is driven at low power, but becomes unreliable when the input power is high, which is due to the simplification of modelling the empirical photothermal effect. This emphasises the importance of a more detailed investigation independently on different types of photothermal effects.

Chapter 4

Photothermal Cancellation in an Optical Levitation System

In the previous chapter, we have presented experimental data and investigated how photothermal effects induce instabilities in the levitation system. The cavity length is changed as a result of photothermal expansion, thermo-optic effects, and the excitation of the acoustic modes of the levitation mirror. These effects have large consequences on the dynamics of the system. They modify the effective frequency and the effective damping of the oscillation. The parametrically amplified oscillation occurs when the cavity is driven by high input power, thus inhibiting stable levitation. In this chapter, we introduce a technique to achieve cancellation of photothermally induced instability. By inserting an optical window inside the cavity, the effective photothermal coefficient of the system can be modified [122]. We analyse the photothermal parameters of various materials that form the optical window. The analysis is employed using a cavity-enhanced detection scheme. The results we obtained not only show a promising way to engineer and control optomechanical interactions in our system, but also offer a potential approach to establish a convenient stabilisation technique, *photothermal backaction feedback*. This technique can be extended to the proposed tripod scheme [67] and further, more general optomechanical systems.

4.1 Theoretical framework

Recalling what we have discussed about the photothermal effect in Chapter 3, we assume that the susceptivity coefficient β_{th} of the empirical photothermal effect in our system is positive, which will always decrease the effective optical length, based on the fact that the self-locking regime only occurs during a downward scan of piezo in the experiments. Under this assumption, we consider thermal expansion as the dominant effect in the system, which has already been proved insufficient for building a reliable model of the dynamics of the system, by the fact that this simple model is less effective in high power regime. Other photothermal effects, such as the thermo-optic effect and a negative thermal expansion coefficient of the mirror material, can increase the effective optical length and dominate under certain conditions. If we merge all the photothermal effects into the empirical

interaction term, then β_{th} in Eq. (3.7) can either be positive or negative depending on the contribution of the individual effects. In this section, without introducing how we change the sign of β_{th} in our experimental setup, we discuss the photothermally induced modification with different susceptivity coefficients β_{th} and explain why it is important to investigate it with different signs.

4.1.1 Bistability of a system with different photothermal interaction

In Chapters 2-3, we have discussed the effects of radiation pressure and photothermal effects with a positive susceptivity coefficient β_{th}. In the absence of these effects ($G = 0$), a Lorentzian profile as a function of detuning (light gray in Fig. 4.1) is observed. Considering only radiation pressure, the optical field interacts with the position degrees of freedom, which modifies the cavity response and induces a resonance shift towards red detuning regime (black). However, with photothermal interaction, if $\beta_{\text{th}} > 0$, the resonances are modified towards blue detuned frequencies due to the negative sign of this interaction term in the system's equations of motion (Eq. (3.5)-(3.9)). The different cavity responses to both optical and photothermal interactions are presented again in Fig. 4.1. For $\beta_{\text{th}} < 0$ (red), the photothermal effects modify the resonance towards the opposite detuning, leading a shift to the red detuned frequencies, the same side as when only the optical field modifies

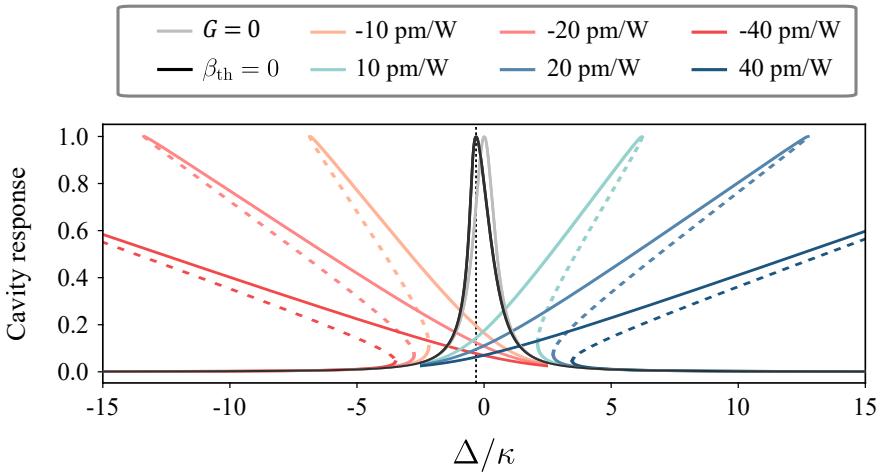

Figure 4.1: Optical bistability of the optomechanical system under different photothermal effects. All plots given in red and blue show the normalised cavity response as a function of optical detuning simulated with progressively stronger photothermal effects corresponding to $|\beta_{\text{th}}|$ of 10, 20, and $40\,\text{pm}\,\text{W}^{-1}$. The reference scenario with no optomechanical backaction ($G = 0$) is plotted in light gray. The black curve represents the system with only radiation pressure and no photothermal effects ($\beta_{\text{th}} = 0$), which indicates that with only radiation pressure, the backaction is not significant and leads only to a small shift in resonance. The system response with both radiation pressure and photothermal effects where $\beta_{\text{th}} < 0$ and $\beta_{\text{th}} > 0$ are shown in red and blue respectively. Optically unstable solutions are plotted in dashed lines, showing the inaccessible cases in steady state. The values of the relevant parameters for simulations are: $P_{\text{in}} = 200\,\text{mW}$, $\kappa/2\pi = 660\,\text{kHz}$, and $\gamma_{\text{th}}/2\pi = 400\,\text{Hz}$.

the effective optical length. Thus, in the red detuning regime, the cavity allows one unstable (dashed red) and two stable steady-state solutions (solid red) simultaneously for the same detuning. The dependence of the cavity response on the direction of the scan is now swapped, as can be seen from Fig. 4.1. Given a scan from red to blue detuning, the cavity is anti-locked. It encounters the unstable region first and then rapidly crosses over to the opposite side of resonance. Whereas, when scanning from blue to red detuning, the time that the cavity stays on the right-hand side of the resonance lengthens, causing the cavity to self-lock. In order to better understand the photothermal interaction with a negative susceptivity coefficient, one can simply use the photothermal expansion to visualise the evolution of the effective optical length during the scan of detuning. With a blue- to red-detuned scan, the bottom mirror moves outwards from the cavity, increasing the optical length. Opposite to the case when $\beta_{\mathrm{th}} > 0$, i.e. the top mirror expands, with a negative β_{th}, the mirror contracts, leading to a further increase in the effective optical length, making the cavity pass the resonance faster, resulting in an anti-lock of the cavity. Scanning from the opposite direction, when the bottom mirror moves inwards to the cavity, the top mirror contracts due to the photothermal effects, leading to a slower reduction of the effective optical length and a consequential self-locking mechanism.

4.1.2 Photothermal induced instability

By inserting different values of β_{th} into the Jacobian matrix given in Chapter 3 (Eq. (3.11)), we can analyse the stability and dynamic evolution of the system. The imaginary $\Im\{\mathrm{eig}(M_{\mathrm{J}})\}$ (Eq. (3.12)) and the real $-2\Re\{\mathrm{eig}(M_{\mathrm{J}})\}$ (Eq. (3.13)) parts of the eigenvalues of this matrix give information about the change in original effective frequency and damping rate of the oscillator due to the optical interaction, shown in Fig. 4.2 with $\beta_{\mathrm{th}} > 0$ in red and $\beta_{\mathrm{th}} < 0$ in blue. Unlike the result we get for the static solution in Fig. 4.1, the effective frequency of the oscillator is predominantly modified by radiation pressure as shown in Fig. 4.2. Comparing the simulation with only radiation pressure ($\beta_{\mathrm{th}} = 0$) to the ones under both interactions, it is clear that changes in the sign or strength of the photothermal effect produce only small variation in the effective frequency. Optical stability, however, is significantly affected by the photothermal interaction. For positive β_{th}, the system cannot be stable at blue detuning regime. When β_{th} is negative, instead, the blue-detuned frequency becomes stable, where the optical back action gives a positive restoring force, as shown in Fig. 4.2(b). The regime where $\beta_{\mathrm{th}} < 0$ is rather important for free-mass and low-frequency optomechanical systems relying on the optical spring effect for optical confinement. In this regime, photothermal effects cooperate with the radiation pressure effect, causing an expansion of the cavity length change in the same direction. Since they contribute differently to the "stiffness" and "damping" properties of the system, they can truly operate together to stabilise the optomechanical cavity from both a static and a dynamic perspective. This was the inspiration for experiments to cancel photothermally induced instability by inverting the sign of the photothermal interaction [122].

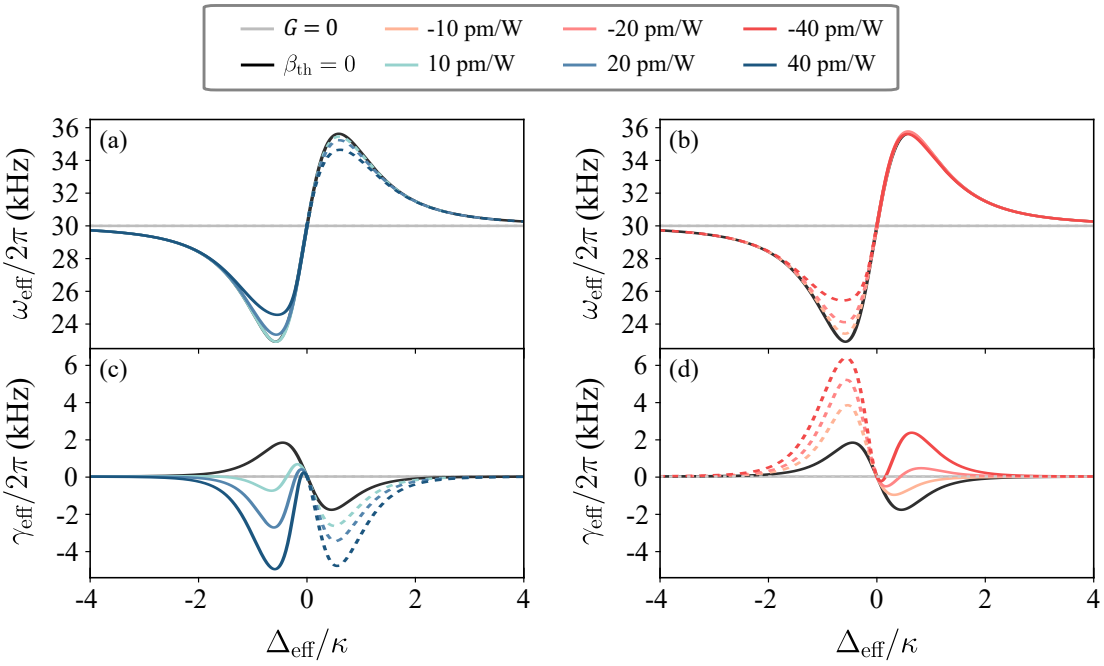

Figure 4.2: Modification of the oscillator's frequency and damping under different photothermal effects. All plots given in red and blue are simulated with photothermal effects corresponding to β_{th} from -40 to 40 pm W^{-1}. The reference scenario with no optomechanical backaction ($G = 0$) is presented in light gray. The black curve shows the simulation of a system with only radiation pressure and no photothermal effects ($\beta_{\mathrm{th}} = 0$). (a) and (b) give the modification of effective oscillation induced by both radiation pressure and photothermal effects with $\beta_{\mathrm{th}} < 0$ and $\beta_{\mathrm{th}} > 0$ respectively. The effective damping of the resonator as a function of effective detuning are shown in (c) and (d). Optically unstable solutions are plotted in dashed lines, showing the inaccessible cases in steady state. The values of the relevant parameters for simulations are: $P_{\mathrm{in}} = 200\,\mathrm{mW}$, $\kappa/2\pi = 660\,\mathrm{kHz}$, and $\gamma_{\mathrm{th}}/2\pi = 400\,\mathrm{Hz}$.

Intuitively, photothermal interaction strongly influencing the damping properties of the system is expected, because the photothermal change due to optical power directly enters into the first-order time derivative of displacement (Eq. (3.2)). The effective damping can be modified to be more than three orders of magnitude greater than the natural damping (30 Hz), where, depending on the sign of β_{th}, parametric instability ($\gamma_{\mathrm{eff}} < 0$) or an increase of stability ($\gamma_{\mathrm{eff}} < 0$) are observed over almost the entire range of effective detuning.

In general, both radiation pressure and photothermal effects contribute to optical backaction by inducing modifications of different properties of the oscillator — the former to the effective frequency and the latter to the effective damping. As such, they can in principle contribute in parallel to the stabilisation of the combined optomechanical system. This inspired the proposal of modifying the cavity with an additional photothermal degree of freedom to passively control the effective interaction and hence stabilise the system. As emphasised earlier, to simplify the simulation and facilitate the analysis of the experimental system, we can always merge different photothermal effects into a joint one under certain conditions, such as when one photothermal effect is dominant or different photothermal effects have similar relaxation rates. The simulations discussed in the following

sections in this chapter are all conducted with low input power where no oscillation is observed. Therefore, the simple model with the empirical photothermal effect is sufficient for the investigation of the system.

4.2 Experimental setup

In the previous section, we discussed how photothermal effects with negative β_{th} could stabilise the optomechanical cavity by inducing positive damping. In this section, we will show that the inclusion of a laser window inside the cavity adds a new photothermal effect into the levitation setup. The additional effect lengthens the optical path length, which can successfully counterbalance the optical length decrease induced by the original photothermal effects, as shown in Fig. 4.3. The window modifies the photothermal response of the system through its photothermal expansion induced as the laser passes through it. Note that the refractive index of the window material will also change with the thermal absorption, which may lead to an effective counter effect to the expansion, for example a decrease in refractive index with a temperature rise. In this chapter, however, we only

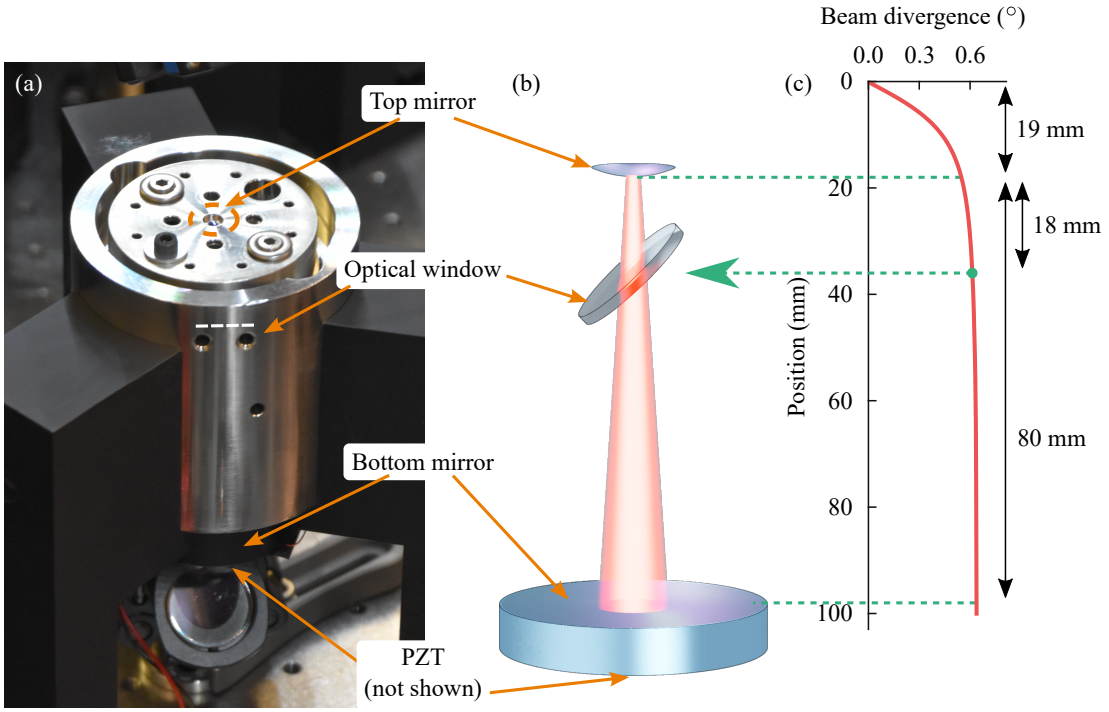

Figure 4.3: Experimental setup and schematic illustration of the vertical cavity with an optical window for photothermal cancellation [122]. (a) The monolithic Invar casing of the optical cavity that is used in the experiments for levitation. The white dashed line shows where the highly transparent window is placed. (b) Schematic illustration of the vertical optical cavity with a free-standing top mirror and a window tilted at Brewster's angle to minimise power loss. (c) The beam size and divergence angle of the intracavity field relative to the cavity length, where the position of each part is presented. The position is zeroed at the waist of the laser beam which has a divergence of 0.6° at the location of the optical window.

consider the overall photothermal effects from different sources. Thus, with optical windows made of different materials, the susceptivity coefficient β_{th} of the photothermal effect can be altered to smaller and even negative values, which provides a promising way to stabilise the system.

More internal cavity losses are induced by a window due to the reflection on its surfaces. Thus, the optical window is designed to be highly transparent and tilted close to Brewster's angle in order to reduce this type of loss. Other effects, such as light scattering and absorption, also increase the loss, which can not be fully removed. In the absence of the laser window, the total cavity loss is estimated to be 2200 ppm, including the transmissivity of 750 ppm for the bottom mirror, 80 ppm for the levitation mirror, and 1370 ppm from the optical scattering, which gives a finesse of around 2850 (measured from the experiment). The implementation of different windows introduces different amounts of losses, as listed in Table 4.1.

In order to minimise the surface scattering loss of p polarised light introduced by the additional windows, we place the uncoated windows inside the Invar case and adjust them to their Brewster's angle. The Invar stage was designed with an adjustable platform where the angle of the optical window can be changed, as seen in Fig. 4.3(a)(b). The calculation of the surface loss as a function of the tilt angle based on Snell's law and Fresnel equations for N-BK7 and sapphire windows is shown in Fig. 4.4. Note that this calculation does not consider additional sources of loss from the window, hence the minimum touches 0. We show in the figure that to achieve a loss induced by the window lower than 900 ppm even after accounting for the beam's divergence angle of 0.6°, the window needs to be put in a certain range: 54.9–58.2° for N-BK7 and 59.2–61.7° for sapphire under a wavelength of 1050 nm for the experiments. The sensitivity of the cavity finesse corresponding to the window angle has been verified in the experiments. We have a range of more than 2°, which is enough for the alignment to find a reasonable angle where the loss of the cavity is still low. Note that it is also possible to use a flat anti-reflection coated window placed horizontally to reduce the loss. Compared to the employment of uncoated windows at

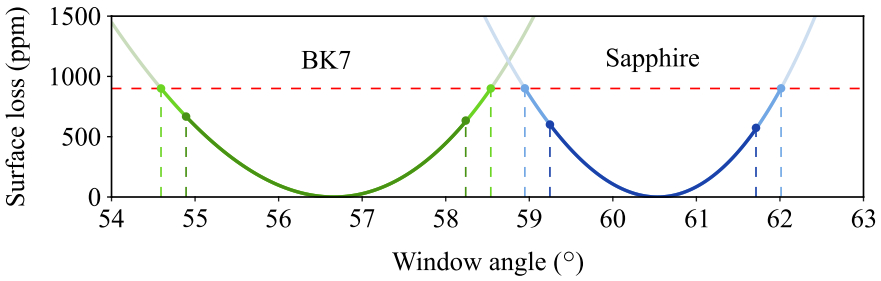

Figure 4.4: Surface loss at the window's interface as a function of the window angle with respect to the laser beam. Brewster's angles are found to be 56.7° for the N-BK7 windows and 60.5° for the sapphire window. The dashed red line defines the loss threshold of a 30% finesse loss. The dark green and dark blue sections present the acceptable range after taking the beam's divergence into consideration [122].

Brewster's angle, however, it is a less effective approach.

Residual surface loss proved hard to estimate quantitatively since it depends on the local surface roughness of the window. The internal absorption loss can be minimised by carefully choosing the window material, although moderate absorption is in fact beneficial for the modification of the photothermal interaction. The input laser is linearly polarised with a zero-order $\lambda/2$ waveplate to obtain an optimum window transmission, as Brewster's angle just works for a particular polarisation but not the others. The window was positioned closer to the beam's waist to ensure a higher optical intensity and a smaller beam size for gaining sufficient photothermal effects on the window to modify the original photothermal effects from the top mirror.

4.3 Photothermal cancellation

The experimental results taken without a window and with a thick (1 mm) N-BK7 window are shown in Fig. 4.5, where (b) and (d) show the cavity responses with the window inserted. When the piezo carries the bottom mirror and scans upwards (from blue to red), as we expected, the cavity is anti-locked due to a positive photothermal interaction. With the thick (1 mm) N-BK7 window, (b) indicates that the cavity responds in a totally different way, which is not only manifested in the swapping of anti-locking and self-locking regime according to the resonance, but is also evident in the sign of the effective damping. Without a window (Fig. 4.5(a)(c)), where $\beta_{\mathrm{th}} > 0$, it is clear to see the amplified oscillation in both anti- and self-locking regime. With the thick N-BK7 window, while scanning from blue to red detuning, the cavity transmission increases slowly, indicating a very big value of β_{th}. Under such strong photothermal effects, however, the cavity doesn't show oscillations.

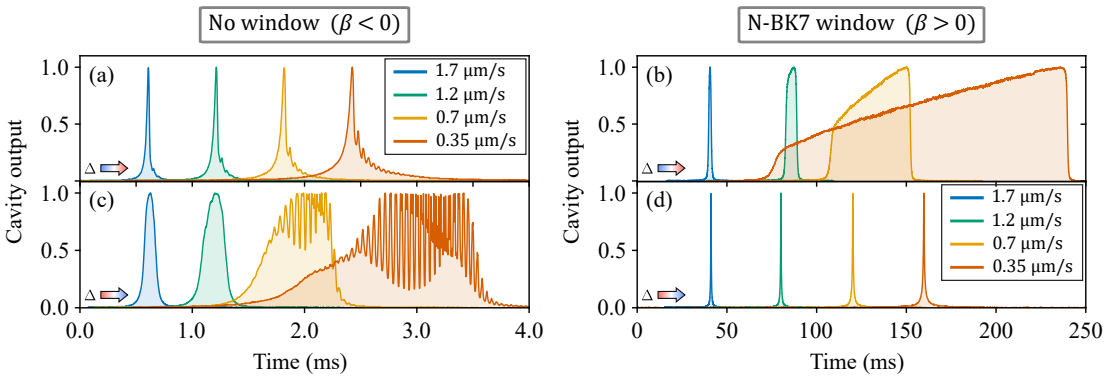

Figure 4.5: Experimental data showing the modification of cavity dynamics from photothermal effects [122]. (a) and (c) Normalised transmission of a bare cavity without any window ($\sigma_{\mathrm{th}} = 3750 \pm 650\,\mathrm{Hz\,pm\,W^{-1}}$). The data was taken under 144 mW input power. (b) and (d) Normalised transmission of the same cavity after inserting a 1 mm thick N-BK7 optical window ($\sigma_{\mathrm{th}} = -22380 \pm 670\,\mathrm{Hz\,pm\,W^{-1}}$). An input power of 310 mW was applied to the cavity for this set of data. The blue-to-red and red-to-blue scans are shown respectively in (b) and (d). Here, $\sigma_{\mathrm{th}} = \gamma_{\mathrm{th}}\beta_{\mathrm{th}}$ is calculated by the fitted values of γ_{th} and β_{th} from the experimental data.

This is because the photothermal effect with a negative β_{th} gives a damping effect (positive γ_{eff}) that can suppress the excitation of acoustic modes of the cavity. This is the result we both expected and desired, which is discussed earlier with the Jacobian matrix, and is presented in Fig. 4.2(d).

4.3.1 Optical window parameters

Parameters fitted from the experimental data of the bare cavity and the cavity with different optical windows are listed in Table 4.1. The 1 mm thick N-BK7 window is produced by Thorlabs (part number WG11010). The sapphire and the thin N-BK7 wafer windows are from Edmund Optics (part number 66-188). Very different optical absorption and photothermal properties might be observed with N-BK7 windows from different suppliers. The transmittance reported by Thorlabs is 0.927 (10 mm-thick sample) at the wavelength of 1050 nm. The transmittance reported by Edmund Optics, however, is 0.999 (10 mm-thick sample) and 0.997 (25 mm-thick sample) at the same wavelength. The N-BK7×2 and N-BK7×4 windows are stacks of individual thin wafers joined by a small amount of optical index-matching fluid designed for N-BK7 (Cargille's BK7 glass matching liquid, part number 19586) [122].

Table 4.1: Parameters of the cavity with different optical windows.

	Bare	Sapphire	N-BK7 ×1	N-BK7 ×2	N-BK7 ×4	N-BK7 thick
Refractive index	—	1.77	1.52	1.52	1.52	1.52
Thickness (mm)	—	3.0	0.22	0.44	0.88	1.0
Photothermal coefficient, $\sigma_{\mathrm{th}}/2\pi$ ($\mathrm{Hz\,pm\,W^{-1}}$) (fitted)	3750(650)	2870(350)	2120(740)	960(230)	N/A	-22380(670)
Photothermal relaxation rate, $\gamma_{\mathrm{th}}/2\pi$ (Hz) (fitted)	426(145)	279(10)	380(115)	151(51)	N/A	4.39(13)
Photothermal susceptivity, β_{th} ($\mathrm{pm\,W^{-1}}$) (fitted)	9.3(19)	10.5(13)	7.0(6)	6.6(15)	N/A	-5100(20)
Cavity finesse (measured)	2850(73)	2240(41)	2350(40)	2070(43)	1915(44)	650(4)
Cavity linewidth, κ (MHz) (measured)	0.33	0.42	0.40	0.45	0.46	1.44

Here in the table, to measure the cancellation strength, we define the photothermal coefficient as $\sigma_{\mathrm{th}} = \gamma_{\mathrm{th}}\beta_{\mathrm{th}}$. With a smaller value of the photothermal coefficient σ_{th}, smaller photothermal interaction is observed in the system, which leads to less bistable behaviour

of the system. This shows the cancellation of the photothermal effects of different materials. The negative sign of the photothermal coefficient of the cavity with think N-BK7 window indicates the flip of the modification of the photothermal effects (Fig. 4.5).

4.3.2 Theoretical fit and error analysis

Background noise sources, such as acoustic vibrations, laser fluctuation, and seismic noise, strongly affect raw data traces. The uncertainties from the nonlinearity of the piezo actuator also introduce error in the measurement. The regular approach to parameter estimation gives the error bar obtained with a statistical distribution of the best fitted parameters that are extracted from the individual measurements taken under the same experimental configuration. Cavity finesse, linewidth, and scan speed of the piezoactuator are calibrated independently before the fitting of γ_{th}, β_{th}, and σ_{th}. This method of error analysis, however, is not always possible to employ in our experimental data, especially when the photothermal effects are almost fully cancelled, so that β_{th} is close to 0. Thus, a different method is needed to analyse the error of the parameters.

For the bare cavity, the cavity with the sapphire window, and the cavity with the 1 mm thick N-BK7 window, we get the best fits for γ_{th}, β_{th} and σ_{th} by least-square optimisation. The values of the fitting results listed in Table 4.1 are obtained from the average best fits with error given by the standard deviation. We give the examples of the fitting for individual traces in Fig. 4.6, where only self-locking results are presented. That is because in the self-locking regime the cavity crosses the resonance slowly, allowing the photothermal effects to modify the cavity response during a relatively long time. This leads to better precision when extracting the fitted parameters. Note that for the 1 mm

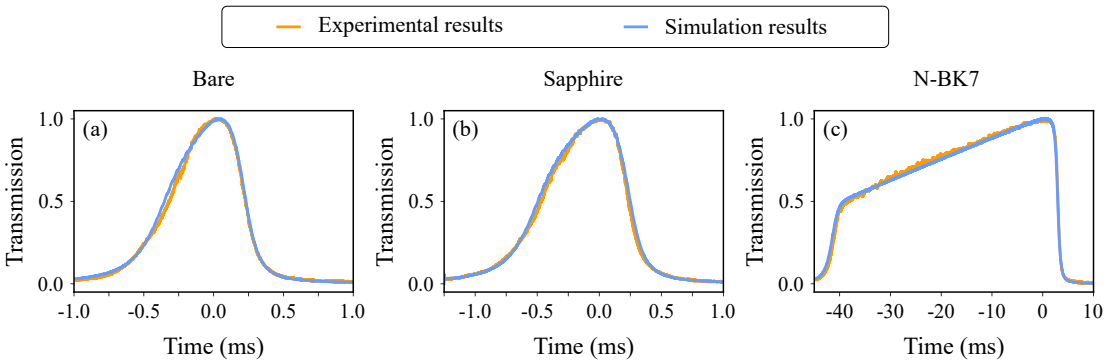

Figure 4.6: Representative plots of cavity output for (a) the bare cavity (with an input of 93 mW and a scan-speed of 0.79 µm s^{-1}), (b) cavity with a 3 mm sapphire window (with an input of 230 mW and a scan-speed of 0.92 µm s^{-1}), and (c) cavity with 1 mm N-BK7 window (with an input of 310 mW and a scan-speed of 0.65 µm s^{-1}). Orange and blue curves show the single experimental traces used for parameter fitting and the best theoretical fits respectively. The resulting parameters are: (a) $\gamma_{\mathrm{th}}/2\pi = 426$ Hz, $\beta_{\mathrm{th}} = 9.3$ pm W^{-1}, and $\sigma_{\mathrm{th}}/2\pi = 3962$ Hz pm W^{-1}; (b) $\gamma_{\mathrm{th}}/2\pi = 279$ Hz, $\beta_{\mathrm{th}} = 10.5$ pm W^{-1}, and $\sigma_{\mathrm{th}}/2\pi = 2930$ Hz pm W^{-1}; (c) $\gamma_{\mathrm{th}}/2\pi = 4.3$ Hz, $\beta_{\mathrm{th}} = -5100$ pm W^{-1}, and $\sigma_{\mathrm{th}}/2\pi = -21\,930$ Hz pm W^{-1}.

N-BK7 window, the photothermal susceptivity coefficient is negative, so the self-locking regime occurs in the scan-up direction.

With single or multiple layered thin N-BK7, as $\beta_{\rm th}$ gets closer to 0, to observe visible photothermal effects, the detuning scans have to be slowed down to a greater extent, making the scans results more vulnerable to acoustic noise (example traces are shown in Fig. 4.7). The resulting errors in fitting parameters from individual traces are extremely large. Filtering was considered but not possible due to the similar time-scales between the noises and the cavity response. In such a scenario, instead, we use the average of multiple data traces to smooth out the wobbles caused by external noise. When averaging multiple traces, it is necessary to overlap them. Choosing different reference points to orient all the traces to take the average, then, introduces an uncertainty for the fitting. Thus we define a weighted averaging method to analyse the error arising from the alignment. We calculate the average traces aligned at multiple different reference points, e.g. 10%, 20%, $\cdots$, 100% of the maximum values of the transmission. The standard deviation of the average traces under different alignments is considered as the weight of the sample:

$$w_1 = \frac{1}{\mathrm{Std}_1},\ w_2 = \frac{1}{\mathrm{Std}_2},\ \ldots,\ w_{\rm N} = \frac{1}{\mathrm{Std}_{\rm N}}. \tag{4.1}$$

Here we align the traces at different percentages of the maximum on both the left- and right-hand sides of the resonance, which gives 19 average traces, so we have $N = 19$ in our analysis. Thus the average and the error of $\gamma_{\rm th}$, $\beta_{\rm th}$ and $\sigma_{\rm th}$ are given:

$$\gamma_{\rm std} = \sqrt{\frac{N\sum_{i=1}^{N} w_i\left(\gamma_{\rm th}^i - \bar{\gamma}_{\rm th}\right)^2}{(N-1)\sum_{i=1}^{N} w_i}} \quad \text{where} \quad \bar{\gamma}_{\rm th} = \frac{\sum_{i=1}^{N} w_i\gamma_{\rm th}^i}{\sum_{i=1}^{N} w_i}, \tag{4.2}$$

$$\beta_{\rm std} = \sqrt{\frac{N\sum_{i=1}^{N} w_i\left(\beta_{\rm th}^i - \bar{\beta}_{\rm th}\right)^2}{(N-1)\sum_{i=1}^{N} w_i}} \quad \text{where} \quad \bar{\beta}_{\rm th} = \frac{\sum_{i=1}^{N} w_i\beta_{\rm th}^i}{\sum_{i=1}^{N} w_i}, \tag{4.3}$$

$$\sigma_{\rm std} = \sqrt{\frac{N\sum_{i=1}^{N} w_i\left(\sigma_{\rm th}^i - \bar{\sigma}_{\rm th}\right)^2}{(N-1)\sum_{i=1}^{N} w_i}} \quad \text{where} \quad \bar{\sigma}_{\rm th} = \frac{\sum_{i=1}^{N} w_i\sigma_{\rm th}^i}{\sum_{i=1}^{N} w_i}. \tag{4.4}$$

Examples of weighted averaging method for cavity data taken with single and double N-BK7 wafer windows are given in Fig. 4.8. Fitting under an alignment at 50% and 100% of maximum values are presented. The fits are of acceptable confidence. It is worth noting that the data for the double N-BK7 wafer window is noisier than that for a single wafer window. In the case of quadruple stack of N-BK7 wafer windows, however, with a power of more than 60 mW, the downward-scan trace started showing other phenomena and the model with only empirical photothermal effect term is not effective. With lower power, the photothermal effects in the cavity response during both downwards and upwards scans are very small, leading to an insufficient fitting of the parameters and the error bar with the methods mentioned in this section. The transmission under different scan directions is nearly symmetric, which indicates that the photothermal effect is close to zero (see

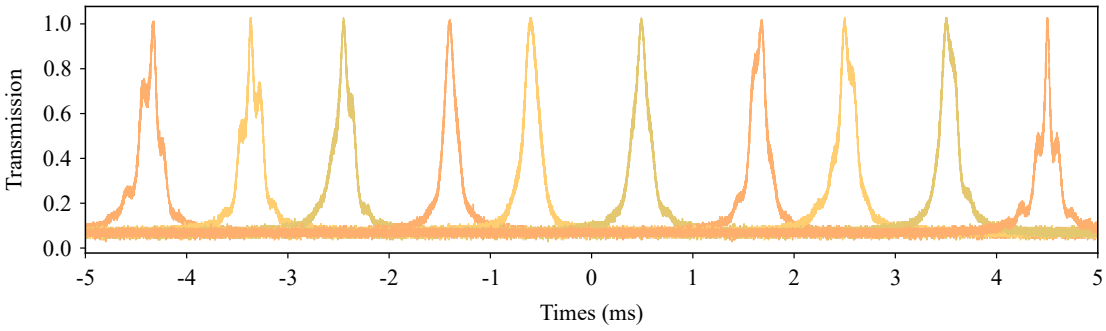

Figure 4.7: Representative plots of transmission of the cavity with $4 \times 0.22\,\text{mm}$ N-BK7 wafer windows. The 10 traces shown in the plots are the cavity outputs under the same experimental condition where the input power is 40 mW and the cavity is scanned downwards with a speed of $1.69\,\mu\text{m}\,\text{s}^{-1}$.

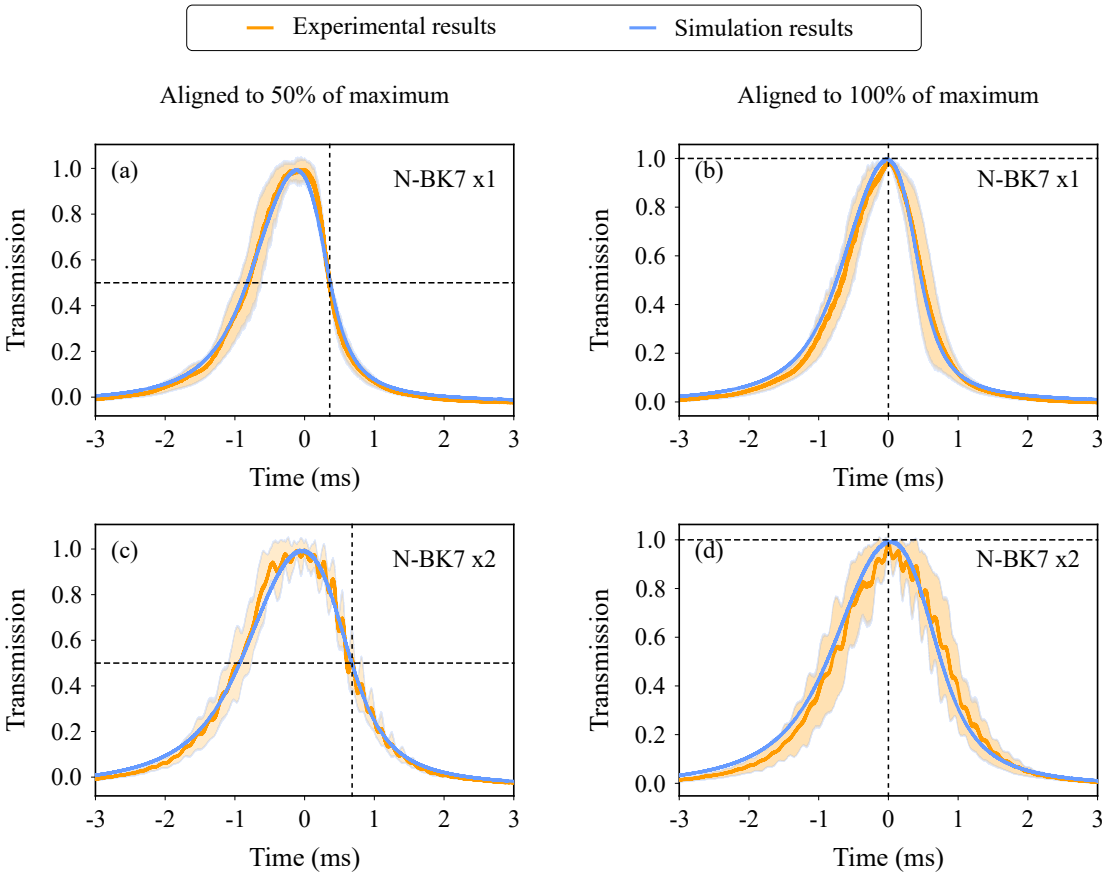

Figure 4.8: Representative plots of experimental results and theoretical fittings of transmission for a cavity with (a)-(b) single N-BK7 window (with scan-speeds of $0.26\,\mu\text{m}\,\text{s}^{-1}$) or (c)-(d) double N-BK7 window (with scan-speeds of $0.21\,\mu\text{m}\,\text{s}^{-1}$). The darker orange curves represent the average of the experimental data. Individual traces of same experimental configuration are given by the lighter boundaries, where (a) (c) shows when they are aligned at 50% of maximum, and (b) (d) illustrate the alignment of them at 100% of maximum. Blue traces are the simulation with the best fitting values of the parameters.

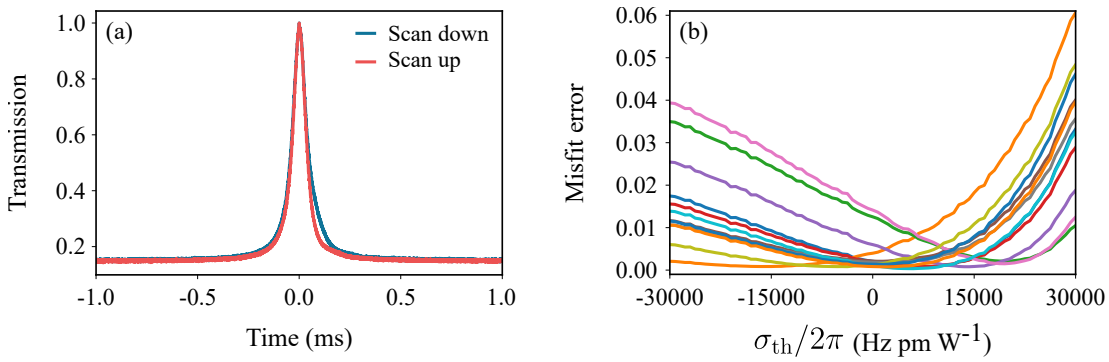

Figure 4.9: Cavity response and misfit error of $4 \times 0.22\,\mathrm{mm}$ N-BK7 wafer windows. (a) Transmission with downwards and upwards scan ($3.49\,\mu\mathrm{m\,s^{-1}}$) of the cavity length with an input power of 40 mW, indicating the significant cancellation of photothermal effects with N-BK7 windows. (b) Misfit error versus σ_{th} with the alignment of data traces taken from same experimental configuration at different reference point. Different colours correspond to different alignments.

Fig. 4.9). When using the same averaging method to process the data, the fits turned out to be untrustworthy. The best fits of σ_{th} with different alignments varied largely from $-16\,500\,\mathrm{Hz\,pm\,W^{-1}}$ to $19\,500\,\mathrm{Hz\,pm\,W^{-1}}$. In this scenario, extracting the photothermal parameters from the data is not a good approach to estimating the photothermal effects interacting with the system. But as shown in Fig. 4.9(b), we can still draw the conclusion that most low misfit errors populate at the values where σ_{th} is near zero.

Note that using a joint photothermal interaction to describe the cavity dynamics can simplify the model but still give a relatively accurate estimation on how strong the overall photothermal effects inside the cavity under certain conditions. Less modification is induced with single or double N-BK7 windows. In this situation, one photothermal effect is dominant. Therefore the dynamics can be simulated accurately. The error prone model with four N-BK7 windows again emphasises the necessity of an in depth investigation on different photothermal effects. The fitting values of photothermal relaxation rate γ_{th} under different circumstances are not consistent with each other (Table 4.1). This indicates that the response time of the photothermal effects from the windows and the top mirror are different. That is because a zero β_{th} represents a nearly complete cancellation of the photothermal effects. This happens when interaction strength of the photothermal effects induced by the top mirror and the window are relatively equal, thus the overall photothermal effect model becomes untrustworthy.

4.4 Conclusion

In this chapter, we have discussed, in general, how the photothermal effects with different susceptivity coefficients affect the dynamics of an optomechanical system and thus induce bistability or stability into the system. We illustrated the principle of photothermal cancellation where a formerly unstable system can be rendered stable by the suppression of

parametric gain. The theory given can be generally used in any optomechanical system where photothermal effects are considered. In the experiments, by including a window into the cavity, we modified and even cancelled the photothermal properties of our system. By inverting the sign of the photothermal interaction to let it cooperate with radiation pressure, we balanced the cavity dynamics around a stable equilibrium point. The technology discussed in this chapter provides a passive feedback control for the applications that are particularly susceptible to parasitic photothermal effects, such as high-sensitivity resonating systems. This stabilisation technique is beneficial for improving system performance limited by photothermal dynamics, and can be easily adapted into the areas of optics, optomechanics, photonics, and laser technologies.

Chapter 5

Refined Model with Multiple Photothermal Effects

In the last two chapters, we briefly mentioned the ineffectiveness of the existing model, where we use only one empirical photothermal effect term to describe the overall effects that come from the changing properties of mirror materials. Given that usually the response times of different properties are different, merging them into a combined photothermal effect eliminates the association between each other, which may lead to incorrect modeling of the system in a certain range. For example, with different power or temperature dependence, two different thermal effects may both get enhanced in one power regime but counteract each other in another regime. Moreover, different effects respond at different paces, giving different relaxation times. Thus, some effects may only manifest themselves when the scan of the cavity is slow if they have a large relaxation time.

We have observed in Chapter 4 that the existing model gives rather reliable simulations when one of the photothermal effects dominates the interaction — a large positive effect governed by the expansion of the top mirror or a large negative effect the strong modifications caused by the optical window inside the cavity. When two counteracting photothermal effects have their interaction strength at the same level, as shown in the last chapter, even with low input power, numerical fitting with the existing model becomes unreliable. In Chapter 3, we also showed that with higher input power, the model loses its reliability, which may be caused by the different relaxation times or power dependence of the photothermal effects. Therefore, it is very important to give an in-depth investigation into separate photothermal effects and discuss them individually.

In this chapter, we will take a step back and consider the normal cavity without window where we will focus on two different photothermal effects that influence the cavity. One is thermal expansion: by absorbing optical power, the coating and substrate of the mirrors can expand and cause a reduction in cavity length. Another possibility is the thermo-optic effect, where the refractive index of a material is modified due to a variation in temperature, thus changing the effective optical path of the cavity. This effect is not negligible, and we will see in fact it plays a significant role in this system.

5.1 Heat transfer and optical intensity in the coating

To understand the photo-induced thermal effects on the mirror, we first need to understand not only how the different components of the mirror react to the absorption of optical power, but also how the temperature and optical intensity are distributed within the materials of the mirror. With an extremely high intracavity field of a few kilowatts, and a small beam diameter near the coating around 100 µm, even a small fraction of radiation absorption can cause a local rise in temperature in the coating, resulting in photothermal expansion and thermo-optic effects that modify the effective cavity length.

To undertake an in-detail analysis on these two effects, we first calculate the optical intensity inside the mirror coating. The top mirror is coated with a dielectric Bragg coating designed for high reflectivity. The coating is made of $\lambda/4$-wave doublets and a $\lambda/2$-wave cap layer, shown in Fig. 5.1(b) with the high-index material Ta_2O_5 and the low-index material SiO_2. In Fig. 5.1(a), we give a simulation of the intensity of the light field, by

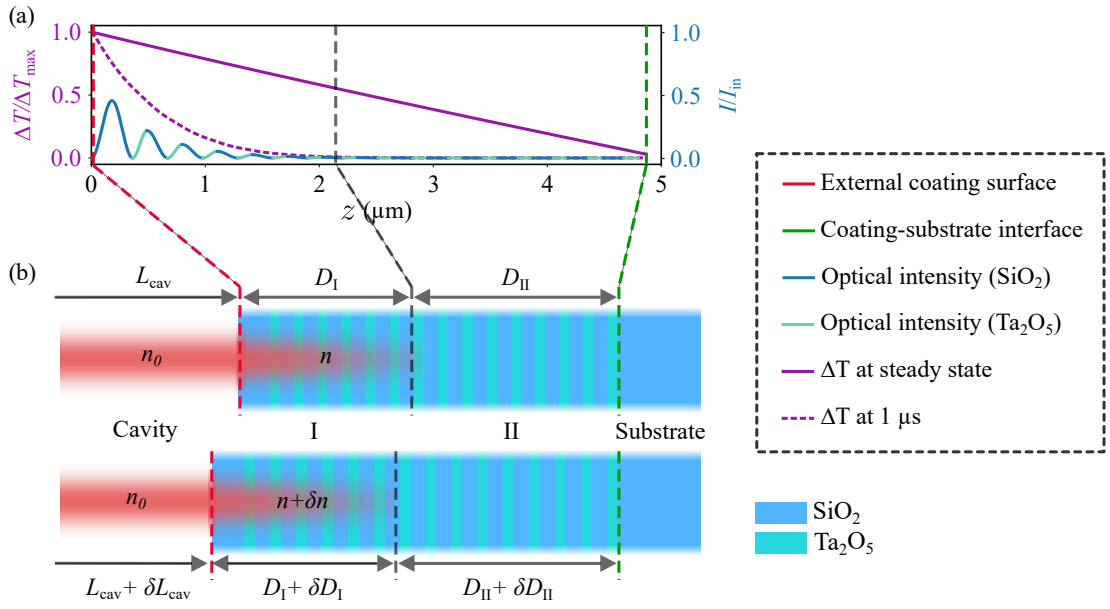

Figure 5.1: Phothermal expansion and thermo-optic effects in the dielectric Bragg coating of the top mirror. Simulation of the optical intensity of the light field inside the cavity is shown in (a), the darker and lighter blue represent the light field inside the layer of SiO_2 and Ta_2O_5 respectively. The mirror coating absorbs the heat from the laser and transfers it to the deeper layers, causing a temperature gradient along the z axis. The dashed purple curve gives the temperature change at 1 µs after the laser shone on the surface of the mirror. The solid purple line shows the thermal distribution inside the levitation mirror coating at equilibrium time. (b) Schematic of the expansion and refractive index change of the top mirror due to photothermal effects, which cause effective optical length variation. The upper figure illustrates the coating before it absorbs the heat from the intracavity field, and the lower figure shows the material after response to the photothermal effects. The red and green dashed lines that connect (a) and (b) represent the external coating surface and the coating-substrate interface. The grey dashed line divides the coating into Part (I) and (II) where 1% light transmits through.

deriving the transfer matrix formalism for electromagnetic waves in the layered dielectric coating with the boundary conditions set at the interface between each layer. The dashed grey line is drawn at the layer around 2 µm deep in the coating, where 99% of the light is reflected. Using this as a boundary, we divide the top mirror coating into two different parts, shown in Fig. 5.1(b): part (I) close to the surface (red dashed line) with thickness D_{I} and part (II) connected to substrate (green dashed line) with thickness D_{II}. The laser shone on the mirror not only produces optical energy but also thermal energy. The heat from the intracavity field is thus absorbed by the mirror coating and then diffused into the deeper layers, causing a temperature gradient inside the coating along the z axis.

In order to investigate how the mirror responds to the intracavity field by absorbing the thermal energy from it, we estimated the thermal conduction of the coating by solving the heat diffusion equation numerically:

$$\alpha \nabla^2 T(x,y,z,t) - \frac{\partial T(x,y,z,t)}{\partial t} = 0, \tag{5.1}$$

where $T(x,y,z,t)$ denotes temperature. We use a cylindrical mirror with a coating formed of two materials, Ta_2O_5 and SiO_2, as shown in Fig. 5.1(b). The thermal diffusivity $\alpha = \kappa_{\mathrm{th}}/s\rho$ of Ta_2O_5 (SiO_2) is 1.57×10^{-8} (8.41×10^{-10}) $\mathrm{m^2\,s^{-1}}$, where $s = 5.0\times10^5$ (7.5×10^5) $\mathrm{J\,kg^{-1}\,K^{-1}}$ is the specific heat, $\rho = 4.2\times10^3$ (2.2×10^3) $\mathrm{kg\,m^{-3}}$ is the density and $\kappa_{\mathrm{th}} = 33$ (1.38) $\mathrm{W\,m^{-1}\,K^{-1}}$ is the thermal conductivity [123]. Since the cavity power decays sharply inside the coating, the heat is deposited primarily near the surface. With the fact that the laser beam used in the experiments has a Gaussian intensity profile, we assume that the mirror experiences a Gaussian flux:

$$\vec{n}\cdot\vec{\nabla}T(x,y,0,t) = -\frac{P_{\mathrm{circ}}\mathcal{A}}{\kappa_{\mathrm{th}}\pi w_0^2} e^{-2\frac{x^2+y^2}{w_0^2}}, \tag{5.2}$$

where $\vec{n}$ is the outward-facing unit normal to the surface, the waist size w_0 on the surface of the mirror is around 100 µm, according to the resonant cavity mode, which is constant in time, at its surface center. We estimate the heat transfer with an ideal mirror absorption given by the percentage of light absorbed $\mathcal{A} = 10$ ppm (parts per million) and an input power of 1 W that gives a power circulating in the cavity of $P_{\mathrm{circ}} \approx 300\,\mathrm{W}$. On the inner side of the coating, where the medium of diffusion switches to the fused silica substrate, we homogenise the temperature flux with Robin boundary conditions:

$$\kappa_{\mathrm{th}}\vec{n}\cdot\vec{\nabla}T(x,y,z_1,t) + h\,(T - T_1) = 0, \tag{5.3}$$

where $h = 1.65\times10^8$ $\mathrm{W\,m^{-2}\,K^{-1}}$ is the thermal contact conductance (TCC) which is defined as the reciprocal of thermal contact resistance (TCR) [124]. $T(x,y,z_1,t)$ represents the temperature at the end of the material simulated, which is the interface between the mirror coating and the substrate. T_1 denotes the temperature of the environment, which we assume is constant. Note that, in vacuum, the major heat loss will be the thermal radiation, thus a different boundary condition needs to be applied.

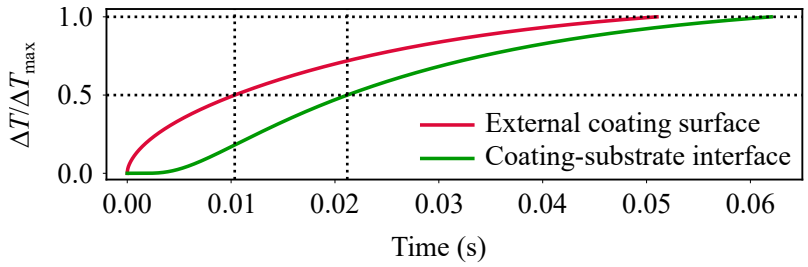

Figure 5.2: Simulation of the temperature changes on the external coating surface (red) and the coating-substrate interface (green) caused by the heat absorption from intracavity field. The temperature changes of the external-coating surface and the coating-substrate interface are normalised to those at the steady-sate. For the external-coating surface, ΔT_{max} is around 1.2 K, whereas for the coating-substrate interface, $\Delta T_{\mathrm{max}} \approx 0.002\,\mathrm{K}$. The colours correspond to the positions indicated by the same colours in Fig. 5.1. The simulation is under an intracavity power of 300 W and an ideal mirror absorption of $\mathcal{A} = 10$ ppm. The thermal properties of the mirror coating that used for the simulations are: for SiO_2, $s = 7.5 \times 10^5\ \mathrm{J\,kg^{-1}\,K^{-1}}$, $\rho = 2.2 \times 10^3\ \mathrm{kg\,m^{-3}}$, and $\kappa_{\mathrm{th}} = 1.38\ \mathrm{W\,m^{-1}\,K^{-1}}$; for Ta_2O_5, $s = 5.0 \times 10^5\ \mathrm{J\,kg^{-1}\,K^{-1}}$, $\rho = 4.2 \times 10^3\ \mathrm{kg\,m^{-3}}$, and $\kappa_{\mathrm{th}} = 33\ \mathrm{W\,m^{-1}\,K^{-1}}$.

Figure 5.2 reveals that the temperature at the external surface rises fast in the beginning, and changes slowly after 0.02 s have elapsed. By contrast, the temperature at the interface of the substrate with the coating that is around 5 µm inside the coating takes around 5 ms to start changing. Since the thermo-optic effect is primarily concentrated at the surface of the coating (D_{I}), while the thermal expansion contributes over the entire coating (D_{I} and D_{II}), we conclude that the timescale for the two processes of thermal expansion and thermo-optic effects differs [121]. The surface layers of the coating thus experience "fast" refractive index variation, while the deeper layers experience "slow" expansion from thermal energy. This gives two different relaxation rates for the different thermal effects, emphasising the importance of separating them into two independent terms. In Fig. 5.1, the simulation of the temperature change 1 µs from the heat source acting on the mirror, and the thermal distribution at equilibrium time are illustrated in dashed and solid purple lines. Note that the absorption of the mirror coating in the experimental setup is usually not ideal and the system is sometimes operated under high input power (as high as 5 W). Both higher input power and larger absorption will cause more heat to transfer into the mirror coating, hence resulting in higher temperature rise. From Eq. (5.2), however, we know that the values of the intracavity power P_{circ} and the absorption $\mathcal{A}$ don't change the evolution of the thermal conduction. The time taken to reach equilibrium (Fig. 5.2) and the distribution of the temperature (Fig. 5.1(a)) thus remain the same with different P_{circ} and $\mathcal{A}$.

5.2 Photothermal expansion and thermo-optic effects

As we mentioned earlier, temperature change can cause expansion and changes to the refractive index of the mirror material. Our simulation in Fig. 5.1 tells us that the tem-

perature change of the substrate can be ignored, and the light is almost fully reflected from at the interface between part (I) and (II). Under this estimation, we deduce that part (I) responds to the temperature change on both expansion and refractive index change, whereas in part (II) only the thermal expansion effect is considered since very little optical power penetrates through to experience a change in index. To first-order approximation, the effective cavity lengths before (cold) and after (hot) the top mirror absorbs the thermal energy of the optical field are given by:

$$x_{\text{cold}} = L_{\text{cav}} n_0 + D_{\text{I}} n, \tag{5.4}$$

$$x_{\text{hot}} = (L_{\text{cav}} + \delta L_{\text{cav}})\, n_0 + (D_{\text{I}} + \delta D_{\text{I}})\, (n + \delta n)\,. \tag{5.5}$$

Equation (5.4) gives the effective optical length of the cavity which consists of the effective length outside and inside the mirror coating before the mirror's surface reacts to the thermal effects. The refractive index of the medium of the cavity is n_0, which is air or vacuum in our system. We assume thermal changes to this refractive index to be negligible, if not zero (in vacuum). For a demonstrative calculation, it suffices to consider only the average refractive index of the coating n in the following derivation of the two independent thermal effects. With thermal absorption, the expansion of the coating causes an increase of δD_{I} in the thickness of (I) and δD_{II} in (II), which results in a reduction of the distance between two mirrors $\delta L_{\text{cav}} = -(\delta D_{\text{I}} + \delta D_{\text{II}})$. The schematic diagram of the change of the coating is illustrated in Fig. 5.1(b), where we only note the change, $n + \delta n$, in the average refractive index of part (I), which will influence the effective optical length of the cavity. Thus the effective optical length can be written as Eq. (5.5). The substrate is considered to act as a thermal reservoir with direct radiative thermal energy exchanged with the environment.

Ignoring higher order terms, the variation of the effective optical length of the cavity

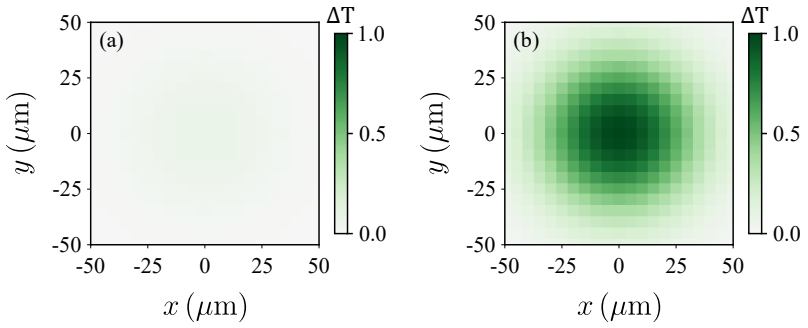

Figure 5.3: Simulation of the temperature changes on a cross-section of the mirror's surface. The temperature changes are normalised to the maximum temperature change (at the centre) at the equilibrium state. (a) gives the temperature change of the surface at 0.2 µs. (b) gives the temperature change of the surface after it has reached the equilibrium state. The simulation is under an intracavity power of 300 W and an optimistic mirror absorption of $\mathcal{A} = 10$ ppm. Other values of the mirror properties used for the simulation are listed in the caption of Fig. 5.2.

due to thermal effects is:

$$\begin{aligned} x_{\mathrm{th}}(D,n) &= x_{\mathrm{cold}} - x_{\mathrm{hot}}, \\ &= -\left(\delta D_{\mathrm{I}} + \delta D_{\mathrm{II}}\right) n_0 + \delta(D_{\mathrm{I}} n), \end{aligned} \tag{5.6}$$

which gives a clearer perspective of the system's reaction to the thermal effects. The effective optical length difference between cold and hot cavity comes from two components: the first term indicates the reduction of the effective optical length from the decrease of the distance between the input and output mirrors of the cavity, while the second term represents the effective optical length change *inside* the levitated mirror.

In our system, we use a gaussian beam to drive the cavity, which causes an inhomogeneous distribution of the thermal flux into the mirror coating and further an uneven distribution of the temperature increase. The rough simulation of the thermal conduction inside the mirror coating shows that the temperature distribution is not uniform in the cross section (see in Fig. 5.3). Therefore, it is important to note that, in our assumption, we only consider the expansion and refractive index change close to the mirror center ($< 100\,\mu\mathrm{m}$ of the diameter). Moreover, because the thermal energy diffused to the edge of the mirror is negligible, we assume that the mirror expansion is towards the interior of the cavity. To further simplify the model, we ignore nonlinear effects on the intra-cavity field and the reshaping of the coating surface, which are caused by the uneven distribution of thermal energy.

By writing it as

$$x_{\mathrm{th}}(D,n) = -\left(n_0 - n\right)\delta D_{\mathrm{I}} - n_0 \delta D_{\mathrm{II}} + D_{\mathrm{I}}\delta n, \tag{5.7}$$

a mathematical perspective of the effective optical length change is given. This helps us to separate the thermal expansion effect and the thermo-optic effect, as well as independently analyse them. The first term indicates the thermal expansion effect on the coating part (I) :

$$\begin{aligned} x_{\mathrm{exI}}(D_{\mathrm{I}}(T)) &= -\left(n_0 - n\right)\delta D_{\mathrm{I}} \\ &= -\left(n_0 - n\right)\frac{\mathrm{d}D_{\mathrm{I}}}{\mathrm{d}T}\delta T. \end{aligned} \tag{5.8}$$

Because $D_{\mathrm{I}} = D_{\mathrm{I,\,cold}} + \delta D_{\mathrm{I}}$, where $D_{\mathrm{I,\,cold}}$ is the original (constant) length before the coating absorbing heat energy, the time derivative of x_{exI} can be written as:

$$\begin{aligned}
\dot{x}_{\mathrm{exI}} &= -\frac{\mathrm{d}(\delta D_{\mathrm{I}}(T(\varepsilon,t)))}{\mathrm{d}t}(n_0-n) \\
&= -\frac{\mathrm{d}D_{\mathrm{I}}(T(\varepsilon,t))}{\mathrm{d}t}(n_0-n) \\
&= -\frac{\mathrm{d}D_{\mathrm{I}}}{\mathrm{d}T}\frac{\mathrm{d}T(\varepsilon,t)}{\mathrm{d}t}(n_0-n) \\
&= -\frac{\mathrm{d}D_{\mathrm{I}}}{\mathrm{d}T}\left(\frac{\partial T}{\partial t}+\frac{\partial T}{\partial \varepsilon}\frac{\mathrm{d}\varepsilon}{\mathrm{d}t}\right)(n_0-n) \\
&= -\frac{\mathrm{d}D_{\mathrm{I}}}{\mathrm{d}T}\left[\gamma_{\mathrm{ex}}(T_0-T)+\frac{\partial T}{\partial \varepsilon}P_{\mathrm{opt}}\right](n_0-n)\,. \qquad (5.9)
\end{aligned}$$

Here we assume that the expansion terms D_{I} and D_{II} and the (average) refractive index of the coating materials n only depend on the local temperature T, which changes due to the thermal energy absorption ε and the cooling by the environment. The thermal relaxation rate is denoted as γ_{ex}. Note that here we use the subscript "ex" to stand for expansion simply for better correspondence in later equations, but this relaxation rate is not intrinsically related to expansion. Given that $\eta_{\mathrm{ex}} = \mathrm{d}P_{\mathrm{opt}}/\mathrm{d}\varepsilon$ is proportional to the reciprocal of the thermal absorption coefficient, which gives the ratio of the thermal energy that the mirror absorbs from the intracavity field, we could further simplify the expression.

$$\begin{aligned}
\dot{x}_{\mathrm{exI}} &= -\frac{\mathrm{d}D_{\mathrm{I}}}{\mathrm{d}T}\left(-\gamma_{\mathrm{ex}}\delta T+\eta_{\mathrm{ex}}\frac{\mathrm{d}T}{\mathrm{d}P_{\mathrm{opt}}}P_{\mathrm{opt}}\right)(n_0-n) \\
&= -\gamma_{\mathrm{ex}}\left[\left(-(n_0-n)\frac{\mathrm{d}D_{\mathrm{I}}}{\mathrm{d}T}\delta T\right)+\left(\frac{\eta_{\mathrm{ex}}}{\gamma_{\mathrm{ex}}}(n_0-n)\frac{\mathrm{d}D_{\mathrm{I}}}{\mathrm{d}T}\frac{\mathrm{d}T}{\mathrm{d}P_{\mathrm{opt}}}\right)P_{\mathrm{opt}}\right] \\
&= -\gamma_{\mathrm{ex}}\left(x_{\mathrm{exI}}+\frac{\partial D_{\mathrm{I}}}{\partial P_{\mathrm{opt}}}P_{\mathrm{opt}}\right) \\
&= -\gamma_{\mathrm{ex}}\left(x_{\mathrm{exI}}+\beta_{\mathrm{exI}}P_{\mathrm{opt}}\right), \qquad (5.10)
\end{aligned}$$

where β_{exI} is susceptivity coefficient of photothermal expansion. This equation shows the power dependence of the expansion, where a positive susceptivity coefficient, where the material expands after absorbing the thermal energy, gives a reduction of the effective optical length. By replacing $(n_0 - n)$ with n and D_{I} with D_{II}, an analogous calculation gives the derivative of the effective optical length change of part (II):

$$\dot{x}_{\mathrm{exII}} = -\gamma_{\mathrm{ex}}\left(x_{\mathrm{exII}}+\beta_{\mathrm{exII}}P_{\mathrm{opt}}\right), \qquad (5.11)$$

where $\beta_{\mathrm{exII}} = \partial D_{\mathrm{II}}/\partial P_{\mathrm{opt}}$.

Because the thermal expansion effect in part (I) and (II) share the same values of γ_{ex}, we can simply add up the two equation (5.10) and (5.11) to get the time derivative of the thermal expansion in the whole mirror coating:

$$\dot{x}_{\mathrm{ex}} = -\gamma_{\mathrm{ex}}\left(x_{\mathrm{ex}}+\beta_{\mathrm{ex}}P_{\mathrm{opt}}\right), \qquad (5.12)$$

where $\dot{x}_{\mathrm{ex}} = \dot{x}_{\mathrm{exI}} + \dot{x}_{\mathrm{exII}}$, $x_{\mathrm{ex}} = x_{\mathrm{exI}} + x_{\mathrm{exII}}$ and $\beta_{\mathrm{ex}} = \beta_{\mathrm{exI}} + \beta_{\mathrm{exII}}$ if the susceptivity coefficient of part (I) and (II) are independent of each other.

Similarly, we can get the derivative of the effective optical length variation of thermo-optic effects:

$$\begin{aligned}
\dot{x}_{\mathrm{re}} &= \frac{\mathrm{d}n(T(\varepsilon,t))}{\mathrm{d}t} D_{\mathrm{I}} \\
&= \frac{\mathrm{d}n}{\mathrm{d}T}\frac{\mathrm{d}T(\varepsilon,t)}{\mathrm{d}t} D_{\mathrm{I}} \\
&= \frac{\mathrm{d}n}{\mathrm{d}T}\left(\frac{\partial T}{\partial t} + \frac{\partial T}{\partial \varepsilon}\frac{\mathrm{d}\varepsilon}{\mathrm{d}t}\right) D_{\mathrm{I}} \\
&= \frac{\mathrm{d}n}{\mathrm{d}T}\left[\gamma_{\mathrm{re}}\left(T_0 - T\right) + \frac{\partial T}{\partial \varepsilon} P_{\mathrm{opt}}\right] D_{\mathrm{I}} \\
&= \frac{\mathrm{d}n}{\mathrm{d}T}\left(-\gamma_{\mathrm{re}}\delta T + \eta_{\mathrm{re}}\frac{\mathrm{d}T}{\mathrm{d}P_{\mathrm{opt}}} P_{\mathrm{opt}}\right) D_{\mathrm{I}} \\
&= -\gamma_{\mathrm{re}}\left[\left(D_{\mathrm{I}}\frac{\mathrm{d}n}{\mathrm{d}T}\delta T\right) - \left(\frac{\eta_{\mathrm{re}}}{\gamma_{\mathrm{re}}} D_{\mathrm{I}}\frac{\mathrm{d}n}{\mathrm{d}T}\frac{\mathrm{d}T}{\mathrm{d}P_{\mathrm{opt}}}\right) P_{\mathrm{opt}}\right] \\
&= -\gamma_{\mathrm{re}}\left(x_{\mathrm{re}} - \frac{\partial n}{\partial P_{\mathrm{opt}}} P_{\mathrm{opt}}\right) \\
&= -\gamma_{\mathrm{re}}\left(x_{\mathrm{re}} - \beta_{\mathrm{re}} P_{\mathrm{opt}}\right), \qquad (5.13)
\end{aligned}$$

where γ_{re} and β_{re} are the thermal relaxation rate and susceptivity coefficient of the thermo-optic effects, and η_{re} is proportional to reciprocal of the thermal absorption coefficient β_{re}, which is only dependent on the refractive index change. Here, we use subscript "re" to stand for refractive index. We use the expression of x_{re} in this deduction, which is written as

$$x_{\mathrm{re}}(n(T)) = D_{\mathrm{I}}\frac{\mathrm{d}n}{\mathrm{d}T}\delta T. \qquad (5.14)$$

Here we give the detailed deduction to emphasise the different sign before the susceptivity coefficient compared with the thermal expansion, which intuitively, is reasonable. Because when the refractive index of the coating increases, the effective optical path length inside the coating increases, which increases the effective cavity length. This indicates that with the positive β_{re}, the refractive index increases when absorbing thermal energy, increasing the deduction of effective optical length. Whereas, in our system, with a negative β_{re}, the refractive index reduces after absorbing thermal energy, leading to a further decrease of the effective optical length.

5.3 Refined model

Replacing Eq. (3.7) in the system of equations of the levitation cavity (Eq. (3.5)-(3.9)) by the two independent equations, Eq. (5.12) and Eq. (5.13), we obtain an updated model containing three, not two, different displacement degrees of freedom interacting with the

intracavity field: thermal expansion, thermo-optic effect, and excitation of acoustic vibrations. Note that here the displacement induced by the partial lift-off of the mirror due to radiation pressure force is not considered because the system is operating under the threshold power that can be used for levitation. We could easily add this degree of freedom into the dynamic equations when including this interaction into the experiments. Thus, the equations become:

$$\dot{a} = \left[-\kappa/2 + i(\Delta + G(x_{\rm ex} + x_{\rm ac} + x_{\rm re}))\right] a + \sqrt{\kappa_{\rm in}} a_{\rm in}, \tag{5.15}$$

$$\dot{a}^* = \left[-\kappa/2 - i(\Delta + G(x_{\rm ex} + x_{\rm ac} + x_{\rm re}))\right] a^* + \sqrt{\kappa_{\rm in}} a^*_{\rm in}, \tag{5.16}$$

$$\dot{x}_{\rm ex} = -\gamma_{\rm ex}(x_{\rm ex} + \beta_{\rm ex} P_{\rm opt}(a)), \tag{5.17}$$

$$\dot{x}_{\rm re} = -\gamma_{\rm re}(x_{\rm re} - \beta_{\rm re} P_{\rm opt}(a)), \tag{5.18}$$

$$\dot{x}_{\rm ac} = p_{\rm ac}/m_{\rm ac}, \tag{5.19}$$

$$\dot{p}_{\rm ac} = -\gamma_{\rm ac} p_{\rm ac} - m_{\rm ac}\omega_{\rm ac}^2 x_{\rm ac} + \hbar G |a|^2. \tag{5.20}$$

From the system of equations, we can get the steady-state solutions by setting the derivative terms to zero, where we get a cubic equation:

$$G^2 \left[-(\beta_{\rm ex} - \beta_{\rm re}) \frac{c}{2}\hbar G + \frac{\hbar G}{m_{\rm ac}\omega_{\rm ac}^2} \right]^2 \left(|a|^2\right)^3 + 2\Delta G \left[-(\beta_{\rm ex} - \beta_{\rm re}) \frac{c}{2}\hbar G + \frac{\hbar G}{m_{\rm ac}\omega_{\rm ac}^2} \right] \times \left(|a|^2\right)^2 + \left(\kappa^2/4 + \Delta^2\right)|a|^2 - \kappa_{\rm in}|a_{\rm in}|^2 = 0. \tag{5.21}$$

Comparing to Eq. (3.10), we notice that the term $\beta_{\rm th}$ in Eq. (3.10) is replaced by $\beta_{\rm ex} - \beta_{\rm re}$. Thus, both $\beta_{\rm ex}$ and $\beta_{\rm re}$ decide the regime where the bistable behaviour of the system occurs (see in Fig. 4.1). If both $\beta_{\rm ex}$ and $\beta_{\rm re}$ are positive, the thermal expansion and thermo-optic effects are competing with each other, thus the overall modification of the cavity resonance is decided by the strength of these two interactions and the side that the resonance is shifted to depends on which is stronger. With a cavity where $|\beta_{\rm ex}| > |\beta_{\rm re}|$, the resonance shifts to a red-detuned frequency and the cavity enters into the self-locking regime during a downwards scanning. If the thermo-optic effect is much stronger than the photothermal expansion, however, the bistable states occur in the blue-detuning regime and the self-locking happens during a red- to blue-detuned scan. In this case, one photothermal effect always reduces the impact on the cavity of the other photothermal effect at stationary state. A similar argument would apply for the photothermal cancellation setup where with only photothermal expansion is under consideration. In that case, inward expansion of the mirror is compensated by the expansion of the window inside the cavity.

When $\beta_{\rm ex} > 0$ and $\beta_{\rm re} < 0$, the thermo-optic effect enhances the modifications caused by photothermal expansion, leading to more obvious photothermal displacement where the resonance shifts to the further blue-detuned regime. This causes the cavity to stay in the self-locking regime longer before it reaches resonance, as we have observed in the experiments when the cavity is driven by a high power (Fig. 3.7). Note that it is also possible to have a negative $\beta_{\rm ex}$, which refers to a material that contracts after absorbing

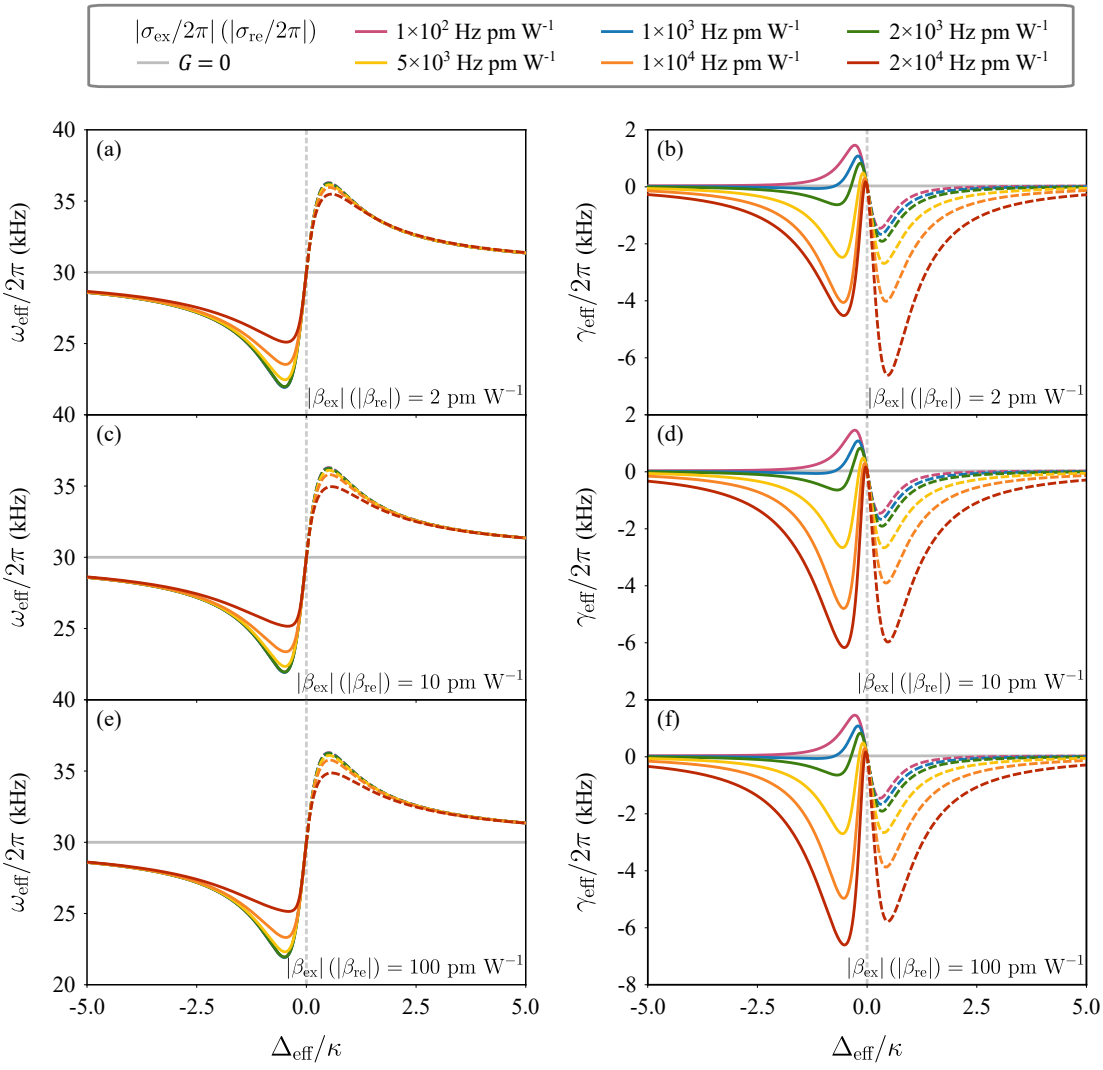

Figure 5.4: Modification of the oscillator's frequency and damping under different photothermal effects. All plots given in colored curves are simulated with photothermal effects corresponding to $\sigma_{ex}/2\pi$ ($|\sigma_{re}|/2\pi$) from 100 to 20 000 Hz pm W^{-1}. The reference scenario with no optomechanical backaction ($G = 0$) is presented in solid light grey line. (a), (c), and (e) give the modification of effective oscillation induced by both radiation pressure and photothermal effects with β_{ex} ($|\beta_{re}|$) = 2, 10, 100 pm W^{-1} respectively. The effective damping of the resonator as a function of effective detuning are shown in (b), (d) and (f). Optically unstable solutions are plotted in dashed lines, showing the inaccessible cases in steady state. The values of the relevant parameters for simulations are: $P_{in} = 200$ mW and $\kappa/2\pi = 735$ kHz.

heat. We will not discuss much about this situation because all the common glass used in optics have positive thermal expansion coefficients [71].

In Chapter 4, we discussed the effects of the photothermal interaction on the cavity steady-state with positive and negative $\beta_{\rm th}$. Along with the Jacobian matrix given by Eq. (3.11), we have also investigated the photothermal modification on the effective frequency and damping of the oscillator under different $\beta_{\rm th}$. Here we rewrite the Jacobian matrix with $\sigma_{\rm th}$, as

$$M_{\rm J} = \begin{bmatrix} -\kappa/2 + i\Delta_{\rm eff} & 0 & iG\alpha & iG\alpha & 0 \\ 0 & -\kappa/2 - i\Delta_{\rm eff} & -iG\alpha^* & iG\alpha^* & 0 \\ -\sigma_{\rm th} c\hbar G\alpha^*/2 & -\sigma_{\rm th} c\hbar G\alpha/2 & -\gamma_{\rm th} & 0 & 0 \\ 0 & 0 & 0 & 0 & 1/m_{\rm ac} \\ \hbar G\alpha^* & \hbar G\alpha & 0 & -m_{\rm ac}\omega_{\rm ac}^2 & -\gamma_{\rm ac} \end{bmatrix}. \tag{5.22}$$

We notice that in Eq. (5.22), both $\sigma_{\rm th}$ and $\gamma_{\rm th}$ play a role and affect the eigenvalues of the matrix. Here, in Fig. 5.4, we present how the photothermal effects change the dynamics of the system with different photothermal relaxation rates $\gamma_{\rm th}$, which are denoted as $\gamma_{\rm ex}$ and $\gamma_{\rm re}$ in the refined model. In order to understand the role that $\gamma_{\rm ex}$ ($\gamma_{\rm re}$) plays in the interaction, we plot the effective frequency and damping of the oscillator with same $\beta_{\rm ex}$ ($|\beta_{\rm re}|$) in Fig. 5.4 (a)-(b). With bigger $\gamma_{\rm ex}$ ($\gamma_{\rm re}$), the oscillation frequency gets slightly closer to the case without any photothermal or radiation-pressure interaction. For the damping rate, however, the modification is significantly dependent on the value of photothermal relaxation rate, where we can see the larger $\gamma_{\rm ex}$ ($\gamma_{\rm re}$) causes negative damping in the whole detuning range. This leads to the parametric gain into the oscillation of the acoustic mode and results in the instability of the system. We then investigate the case when $\sigma_{\rm ex}$ ($|\sigma_{\rm re}|$) is fixed but the $\gamma_{\rm ex}$ ($\gamma_{\rm re}$) is given by different values, under which only one term in the Jacobian matrix (Eq. (5.22)) is changing. Comparing the same color curves in Fig. 5.4(a), (c) and (e), we can tell that the effect of $\gamma_{\rm ex}$ ($\gamma_{\rm re}$) on the oscillation frequency is negligible. For the damping, however, a smaller photothermal relaxation rate $\gamma_{\rm ex}$ ($\gamma_{\rm re}$) gives more negative damping rate, leading to stronger amplification, shown in Fig. 5.4(b), (d) and (f).

The modification on effective damping rate of the oscillator from the photothermal effects with different relaxation rate $\gamma_{\rm ex}$ ($\gamma_{\rm re}$) again indicates the importance to separate different photothermal effects of the system when it is not dominated by only one of them.

5.4 Simulations and analysis

The simulation of the new model for the cavity driven by lower and higher input power are shown in Fig. 5.5 and Fig. 5.6, which compares experimental measurements of the normalised intensity of cavity transmission with the simulated results. The cavity is measured during a linear red-to-blue detuning scan. In all three panels (a–c) of Fig. 5.5

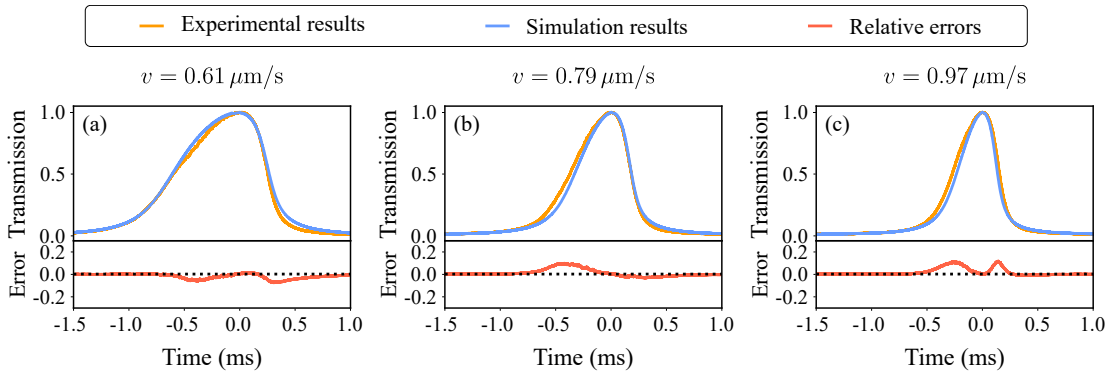

Figure 5.5: Simulation results of the new model for the cavity driven by low input power. The normalised transmissions from experiments under different scan speed are shown in orange. The simulation results (blue) for the cavity with scan speed of $0.61\,\mu\mathrm{m\,s^{-1}}$, $0.79\,\mu\mathrm{m\,s^{-1}}$ and $0.97\,\mu\mathrm{m\,s^{-1}}$ are given in (a), (b) and (c) respectively. The simulation of the new model successfully fits the broadening Lorentzian profile of the traces with different scan speed, which can be inferred from the error given in red. Here, we calculate error with the ratio of the difference between simulation and experimental data to the experimental data. The parameters used in simulation are: $P_{\mathrm{in}} = 93\,\mathrm{mW}$, $\kappa/2\pi = 658\,\mathrm{kHz}$, $\gamma_{\mathrm{ex}}/2\pi = 11\,\mathrm{Hz}$, $\beta_{\mathrm{ex}} = 120\,\mathrm{pm\,W^{-1}}$, $\gamma_{\mathrm{re}}/2\pi = 4000\,\mathrm{Hz}$, $\beta_{\mathrm{re}} = -2\,\mathrm{pm\,W^{-1}}$.

and the panels (a) and (d) of Fig. 5.6, experimental data is in orange, data simulated with the refined model written in Eq. (5.15)–(5.20) is in blue. The data is considered both at low and high power to compare different regimes. At low power (see in Fig. 5.5), traces with the cavity in the self-locking regime (downwards scanning) are aligned at their maximum. Comparing the three traces with different scan speeds, it is easy to see that with higher speed the transmission has a more Lorentzian-shaped resonance. With lower scan speed, however, the traces are broadened due the photothermal effects, showing more obvious characteristics of the bistable behaviour, as we discussed in the previous chapters. These features are well simulated by the refined models with two photothermal effects, by inserting 11 Hz, 4000 Hz, $120\,\mathrm{pm\,W^{-1}}$ and $-2\,\mathrm{pm\,W^{-1}}$ as the values of $\gamma_{\mathrm{ex}}/2\pi$, $\gamma_{\mathrm{re}}/2\pi$, β_{ex} and β_{re} respectively. With higher input power, the refined model gives a more faithful simulation by extending the duration of the oscillatory stage to the same length as the experimental data. This improvement can be seen in the time response of the cavity in both transmission intensity and oscillation frequency. In Fig. 5.6(a), the oscillation duration got extended to twice as long as the simulation from the old model (Fig. 3.7(b)), which is also indicated by the average trace (dark blue). In Fig. 5.6(b)(c), we show that even though the slow frequency increase that can be seen in the experimental data, in panel (b), is not fully simulated by the model, but the frequency change in the beginning (from 1 ms to around 1.7 ms) of the trace can be simulated better. Furthermore, we observe that the build-up process on the left-hand side is also slowed and closer to the measured phenomenon.

Even though the agreement is improved overall, some smaller features of the simulation are still not perfectly harmonised to the experimental data. One of these is the slow power build-up on the left-hand side of resonance, which may be caused by the nonlinearity and

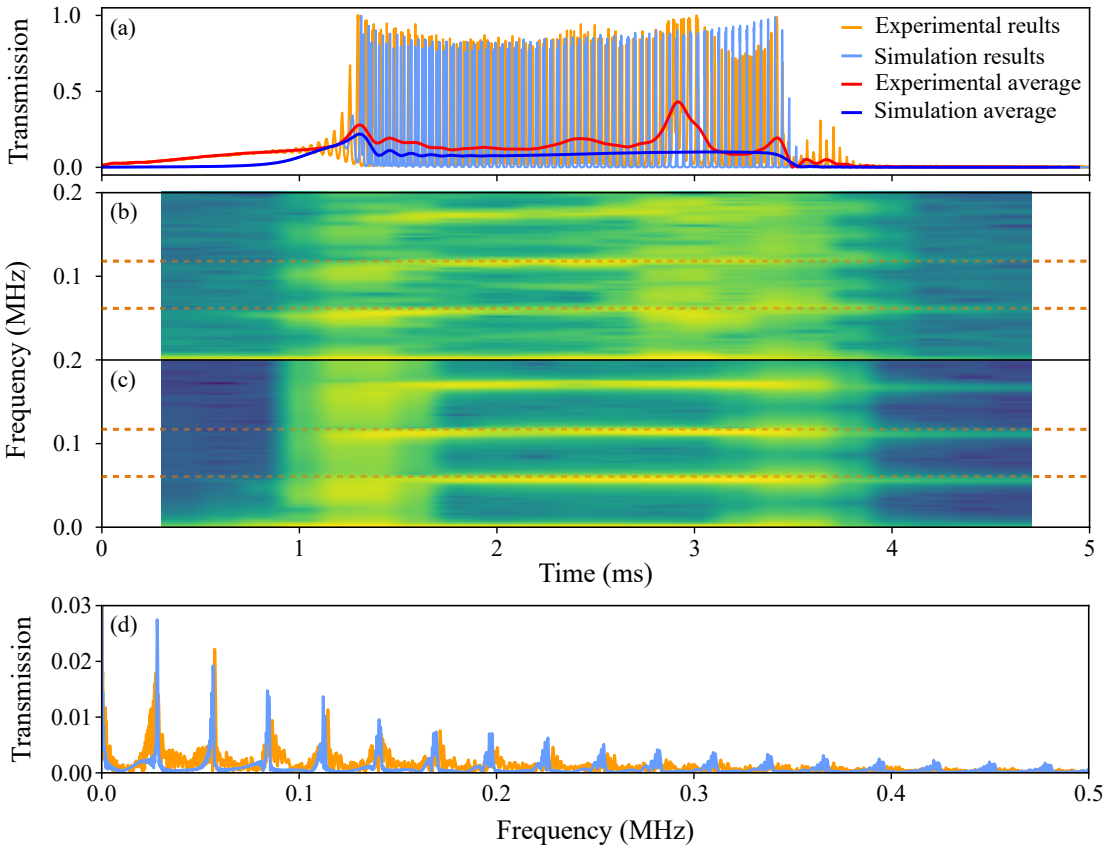

Figure 5.6: Experimental results and simulation of refined model for the system driven by a high power input laser. The orange and blue curves in (a) and (d) are the experimental and simulation data, respectively. (a) shows the normalised transmissions of a self-locking cavity response at an input power of 2.75 W and its calculated average given by a low-pass Butterworth filter which has an order of 20 and the cut-off frequency of 10 kHz. The frequency analysis is presented in (b) and (c), which show frequency evolution of the experimental and simulation results respectively. The orange dashed lines emphasise the acoustic modes frequencies that we are interested in, which are also plotted to show that the oscillation frequency is changing slightly. The values that used for simulation are: $\kappa/2\pi = 735\,\mathrm{kHz}$, $\gamma_{\mathrm{ex}}/2\pi = 11\,\mathrm{Hz}$, $\beta_{\mathrm{ex}} = 120\,\mathrm{pm\,W^{-1}}$, $\gamma_{\mathrm{re}}/2\pi = 4000\,\mathrm{Hz}$, $\beta_{\mathrm{re}} = -2\,\mathrm{pm\,W^{-1}}$. Parameters of other cavity properties are the same as that used in Figure 5.5.

interaction of both thermal effects, requiring more detailed study and analysis of the roles these two effects play in the parametric oscillatory instability of the system. The refined model also failed to provide an accurate simulation of the end part of the oscillation. It may be necessary to include other effects for a more precise model, such as the mode shift in the cavity due to the changing shape of the mirror caused by its local and unequal expansion, the bolometric interaction directly coupling photothermal absorption to the acoustic mode, the dependence of cavity decay rate and the input coupling rate on either acoustic or photothermal displacements.

Other laser-surface interactions are not discussed in our model that may also change the mirror coating and thus the intra-cavity field. For example, photochemical effects usually lead to laser-induced desorption and ablation, photoacoustic effects will affect

surface acoustic waves and further thermal diffusion in the materials, and a repulsion force on the surface may result in the emission of neutrals (via antibonding states), ions, explosive ablation, and shock wave generation. The expansion considered in this model is the simplest effect. There are other possible phenomena, commonly discussed in materials, which may be caused by thermal expansion, such as deformation, stress, evaporation, and again shock wave generation are not included.

5.5 Discussion on different models

In summary, we have introduced two different models: the original model with one joint photothermal effect and the refined model with two separate photothermal effects. In this section, we will discuss the models with different sets of parameters and how they change the simulation results. Furthermore, we will introduce another model with a nonlinear joint photothermal effect by adding a second-order term to the original model.

For easier reference and comparison, the sets of parameters used in different models, which are mentioned in this section are listed in Table. 5.1.

Table 5.1: Parameters of the cavity with different optical windows.

Set No.	1	2	3	4	5
Model	Original	Original	Nonlinear	Refined	Refined
Figures	3.6, 3.7	5.7	5.11	5.5, 5.6, 5.9	5.8, 5.9, 5.10
Photothermal relaxation rate, $\gamma_{\mathrm{th}}/2\pi$ (Hz)	450	450	216	N/A	N/A
Photothermal susceptivity, β_{th} ($\beta_{\mathrm{th},1}$) ($\mathrm{pm\,W^{-1}}$)	9	45	7.5	N/A	N/A
Second-order Photothermal susceptivity, $\beta_{\mathrm{th},2}$ ($\mathrm{pm\,W^{-1}}$)	N/A	N/A	0.035	N/A	N/A
Thermal expansion relaxation rate, $\gamma_{\mathrm{ex}}/2\pi$ (Hz)	N/A	N/A	N/A	11	60
Thermal expansion susceptivity, β_{ex} ($\mathrm{pm\,W^{-1}}$)	N/A	N/A	N/A	120	40
Thermo-optic relaxation rate, $\gamma_{\mathrm{re}}/2\pi$ (Hz)	N/A	N/A	N/A	4000	360
Thermo-optic susceptivity, β_{re} ($\mathrm{pm\,W^{-1}}$)	N/A	N/A	N/A	-2	-10

5.5.1 Best parameters for high-power fits

In the previous section, we presented the simulation of the refined model with two photothermal effects, which gives more reliable results that illustrate most of the characteristics of the cavity dynamics. It is natural to think that by simply increasing the photothermal susceptivity β_{th} of the joint photothermal effect in the old model (Eq. (3.5)-(3.9)), we

can also extend the oscillation duration of the cavity response at higher power regime. We show the simulation results with a larger β_{th} in Fig. 5.7. The time evolution of transmission at higher power (Fig. 5.7(b)) shows the extension of the oscillation as expected. However, it will also change the photothermal interaction strength at lower power regime, leading to discrepancies between the model and the experiment (Fig. 5.7(a)). This is because the profile of the transmission traces with lower power also depends on the modification of photothermal effects. A bigger photothermal susceptivity β_{th} gives a more obvious bistable behaviour of the system (Fig. 4.1). This emphasises the importance of separating the different photothermal effects for a more effective model.

We also mentioned that some smaller features of the experimental traces, such as the slow power build-up on the left-hand side of resonance, are not fitted. Thus, it is worthwhile to show that during the fitting of the values of γ_{ex}, γ_{re}, β_{ex} and γ_{re}, we have seen some simulation traces that fit the experimental results even better in the high power regime. With the same parameters, however, the fittings at lower power have huge discrepancies with the corresponding experiments. One example is given in Fig. 5.8, showing a better fitting for higher power transmission trace and considerably worse fitting at lower power. Panels (b),(c) and (e) show the simulation of the refined model with two photothermal effects, given an input power 2.75 W, the measured κ of $2\pi \times 735$ kHz and the fitted parameters $\gamma_{\text{ex}}/2\pi = 60$ Hz, $\beta_{\text{ex}} = 40\,\text{pm}\,\text{W}^{-1}$, $\gamma_{\text{re}}/2\pi = 360$ Hz, $\beta_{\text{re}} = -10\,\text{pm}\,\text{W}^{-1}$. Comparing with Fig. 5.6(a), the simulation trace (blue) in Fig. 5.8(b) also extends the duration of the oscillatory stage to the same length as the experimental data (orange). Moreover, the slow power buildup on the left-hand side of resonance is also seen in the simulation trace, which can be easily shown by the comparison of the average traces in

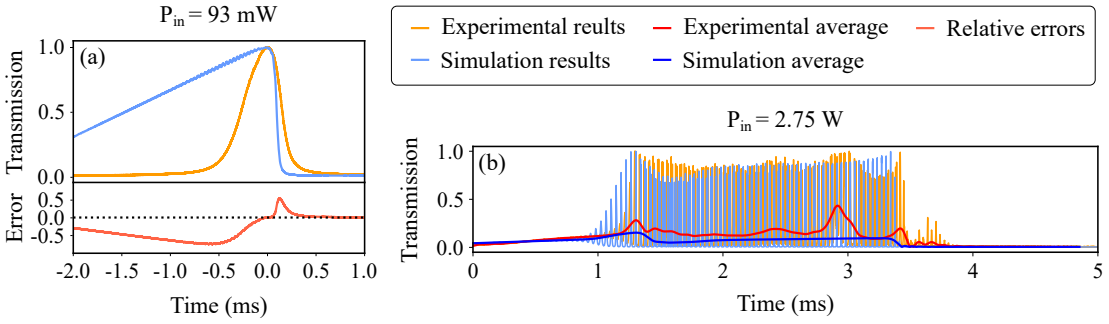

Figure 5.7: An example of the simulation of the original model with joint photothermal effect (Eq. (3.5)-(3.9)), for the system driven by lower and higher power input laser. The parameter that are used in simulations are $\kappa = 2\pi \times 735\,\text{kHz}$, $\gamma_{\text{th}} = 2\pi \times 450\,\text{Hz}$, $\beta_{\text{th}} = 45\,\text{pm}\,\text{W}^{-1}$. (a) presents the huge discrepancy between experimental (orange) and the simulation (blue) data in lower power regime (93 mm), which could also be seen in the error plot (coral). By increasing the β_{th} of the photothermal effect, the duration of the oscillation can be extended in the higher power regime, shown in (b). Other features of the experimental data, however, are not efficiently fitted, especially the peak-level of the oscillation and the initial build-up of oscillations. The low-pass Butterworth filter is applied to both experimental (red) and simulation (blue) results to get the average of the self-locking cavity responses, in order to give a better comparison of the simulations to the experimental results.

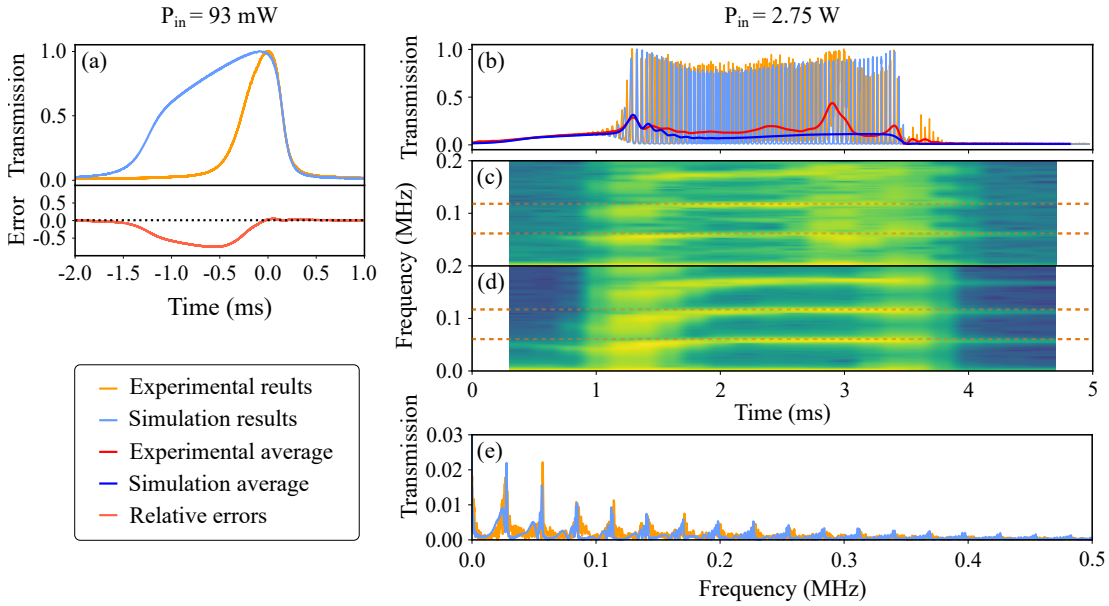

Figure 5.8: An example of the simulation of the refined model for the system that gives better results in high power regime. The parameters used in the simulations are $\kappa/2\pi = 735\,\text{kHz}$, $\gamma_{\text{ex}}/2\pi = 60\,\text{Hz}$, $\beta_{\text{ex}} = 40\,\text{pm}\,\text{W}^{-1}$, $\gamma_{\text{re}}/2\pi = 360\,\text{Hz}$, $\beta_{\text{re}} = -10\,\text{pm}\,\text{W}^{-1}$. For the cavity with an input power of 2.75 W, (b) and (d) show the simulation results of the transmission intensity (blue) and the oscillation frequency in time domain respectively. In (b), the low-pass Butterworth filter is applied to both experimental (red) and simulation (blue) results to get the average of the self-locking cavity responses, in order to give a better comparison of the simulations to the experimental results. In (c) and (d), orange dashed lines emphasise the acoustic modes frequencies of interest. (e) shows the comparison of experimental (orange) and simulation (blue) results of the cavity response in frequency domain. With the same parameters, however, the simulation results (blue) with the input power of 93 mm shown in (a) has a huge discrepancy with the experiments (orange), which can be also seen in the simulation errors plotted in coral.

dark blue and red. In contrast, the same simulation using the original model, fails to accurately capture the dynamics of the initial slow power build up, shown in Fig. 5.7(b). Fig. 5.8(c) and (d) present the time evolution of oscillation frequency in experiment and theory respectively. The dashed orange lines emphasise the acoustic modes frequencies that are of interest. The frequencies increase during the period from 1 ms to 2 ms, shown in both (c) and (d), which indicates the simulation result is in high accordance with the experimental data. With the same parameters, however, the simulation result (blue) at lower power (93 mW) gives a huge discrepancy with the experiments (orange), which is shown in the transmission traces and the error trace (see in Fig. 5.8(a)).

To further understand the discrepancy in the lower power regime, we should discuss the difference when inserting different values of γ_{ex}, γ_{re}, β_{ex} and β_{re} into the dynamic equations of motion Eq. (5.15)-(5.20). We rewrite the evolution of the amplitude of the intracavity field as

$$\dot{a} \quad = \quad (-\kappa/2 + i\Delta_{\text{eff}})\, a + \sqrt{\kappa_{\text{in}}} a_{\text{in}}, \tag{5.23}$$

where

$$\Delta_{\text{eff}} = \Delta + G\left(x_{\text{ac}} + x_{\text{ex}} + x_{\text{re}}\right). \tag{5.24}$$

In the experiments, we change the cavity length linearly with the piezoelectric actuator attached to the bottom mirror, which can be considered as another displacement of the cavity. So the detuning Δ can be written as a function of time (Eq. (2.37)). With the expression of the time derivative of the photothermal and acoustic displacements (Eq. (5.17)-(5.20)), the time evolution of the effective detuning of the cavity can then be written as

$$\begin{aligned}\Delta_{\text{eff}}(t) &= \Delta_0 + G\left(v_{\text{scan}}t + x_{\text{ac}}(t) + x_{\text{ex}}(t) + x_{\text{re}}(t)\right)\\ &= \Delta_0 + G\left[v_{\text{scan}}t + x_{\text{ac}}(t) - \left(\beta_{\text{ex}} - \beta_{\text{re}}\right)P(a(t))\right]\\ &\quad + G\left(\beta_{\text{ex}}e^{-\gamma_{\text{ex}}t} - \beta_{\text{re}}e^{-\gamma_{\text{re}}t}\right)P(a(t)).\end{aligned} \tag{5.25}$$

Note that Eq. (5.25) is given under steady-state conditions, which can be assumed as the case in our slow scans as long as there is no fast oscillation observed in the transmission.

When driving the cavity with lower power, such that no oscillation is observed in the transmission (at around 100 mW), the displacement induced by the acoustic mode of the top mirror is very small compared to that induced by the photothermal interaction and the cavity length scan. With a slow scan, the bottom mirror increases the effective optical length at a speed of around $1\,\mu\text{m}\,\text{s}^{-1}$. With no optomechanical backaction, i.e., no interaction between the top mirror and the intracavity field, the linewidth of the cavity response as a function of detuning κ equals to $2\pi \times 658\,\text{kHz}$, so the Lorentzian profile with a scan of $1\,\mu\text{m}\,\text{s}^{-1}$ has a linewidth of around 0.2 ms in the time domain. At low power, we consider a scan of detuning from -2κ to 2κ a full scan of one peak, so a full scan takes around 0.8 ms. In the experiments, with radiation pressure and photothermal interactions, we usually scan the cavity with even lower scan speed ($0.61\,\mu\text{m}\,\text{s}^{-1}$ as shown in Fig. 5.5) to obtain a more obvious bistable behaviour of the cavity. Due to the photothermal effects, the Lorentzian profile of the transmission gets broadened, resulting in longer scan time for one peak. In the example, we show the transmission of the cavity driven by a 93 mW input power, with a scan of $0.97\,\mu\text{m}\,\text{s}^{-1}$, a full scan of the peak takes around 1 ms (see in Fig. 5.5(c) and Fig. 5.8(a)).

Based on Eq. (5.25), we can explain why for both original model (Fig. 3.6) and the refined model (Fig. 5.5) give relatively good simulation in low power regime. For the simulations that are shown in Fig. 5.5, the values of the parameters for the two photothermal effects are $\gamma_{\text{ex}} = 2\pi \times 11\,\text{Hz}$, $\beta_{\text{ex}} = 120\,\text{pm}\,\text{W}^{-1}$, $\gamma_{\text{re}} = 2\pi \times 4000\,\text{Hz}$, $\beta_{\text{re}} = -2\,\text{pm}\,\text{W}^{-1}$. With these values, the relaxation time of the thermo-optic effect is around 0.04 ms, resulting in a fast decrease to 0 of the term $\beta_{\text{re}}e^{-\gamma_{\text{re}}t}$ in Eq. (5.25). The thermal expansion, however, has a large relaxation time, around 16 ms. Therefore the term $\left(\beta_{\text{ex}}e^{-\gamma_{\text{ex}}t} - \beta_{\text{re}}e^{-\gamma_{\text{re}}t}\right)$ is dominated by $\beta_{\text{ex}}e^{-\gamma_{\text{ex}}t}$. Note also that the $(\beta_{\text{ex}} - \beta_{\text{re}})$ therm is dominated by β_{ex}, hence

we can neglect the β_{re} term. Thus, in Eq. (5.25), the effective detuning of the cavity caused by photothermal effects is dominated by the photothermal expansion. This indicates that with lower input power when the acoustic oscillation is not amplified, the dynamic equations of the system can be described with only photothermal expansion, which explains the effectiveness of the refined model at lower power regime with these parameters. This again emphasises that the model with only a single photothermal effect is reliable when the different photothermal effects share the same relaxation rate, or when only one photothermal thermal effect dominates the system as the case that the bare cavity is driven with lower input power.

Using the parameters that give a better simulation of the initial buildup of the oscillations, the simulation in the lower input power regime has a huge difference with the experimental result (see Fig. 5.8(a)-(e)). This is because the relaxation rates ($\gamma_{\mathrm{ex}}/2\pi = 60\,\mathrm{Hz}$ and $\gamma_{\mathrm{re}}/2\pi = 360\,\mathrm{Hz}$) and the photothermal susceptivity ($\beta_{\mathrm{ex}} = 40\,\mathrm{pm\,W^{-1}}$ and $\beta_{\mathrm{re}} = -10\,\mathrm{pm\,W^{-1}}$) of the photothermal expansion and the thermo-optic effects are at the same order of magnitude, which collectively give stronger photothermal effects, which shorten the cavity length faster than what was observed in the experiments. This leads to the considerable discrepancy between simulation and experiments in the lower power regime. We note that the discussion about cavity responses with different photothermal parameters through their effects on effective detunings is limited to lower power regime. This is because when the intracavity power increases the photothermal effects excite the acoustic modes of the top mirror and induce amplified parametric oscillation, giving rise to the large variation of the acoustic displacement $x_{\mathrm{ac}}(t)$, which changes the intracavity intensity rapidly and further affects the photothermal displacements.

5.5.2 Optical spring

To further investigate the modification to the dynamics of the optomechanical system from the two different photothermal interactions and their combined effect, we solve the Jacobian matrix of the refined model (Eq. (5.15)-(5.20)), which is written as

$$M_{\mathrm{JR}} = \begin{bmatrix} -\kappa/2 + i\Delta_{\mathrm{eff}} & 0 & iG\alpha & iG\alpha & iG\alpha & 0 \\ 0 & -\kappa/2 - i\Delta_{\mathrm{eff}} & -iG\alpha^* & iG\alpha^* & iG\alpha^* & 0 \\ -\gamma_{\mathrm{ex}}\beta_{\mathrm{ex}}c\hbar G\alpha^*/2 & -\gamma_{\mathrm{ex}}\beta_{\mathrm{ex}}c\hbar G\alpha/2 & -\gamma_{\mathrm{ex}} & 0 & 0 & 0 \\ \gamma_{\mathrm{re}}\beta_{\mathrm{re}}c\hbar G\alpha^*/2 & \gamma_{\mathrm{re}}\beta_{\mathrm{re}}c\hbar G\alpha/2 & 0 & -\gamma_{\mathrm{re}} & 0 & 0 \\ 0 & 0 & 0 & 0 & 0 & 1/m_{\mathrm{ac}} \\ \hbar G\alpha^* & \hbar G\alpha & 0 & 0 & -m_{\mathrm{ac}}\omega_{\mathrm{ac}}^2 & -\gamma_{\mathrm{ac}} \end{bmatrix}. \quad (5.26)$$

By inserting different values of the parameters, the imaginary ($\Im\{eig(M_{\mathrm{JR}})\}$) and the real ($-2\Re\{eig(M_{\mathrm{JR}})\}$) parts of the eigenvalues of the matrix give different numerical results of cavity responses. Using the solution of the Jacobian matrix, we can then analyse the difference between the simulation results of the two sets of parameters used in Fig. 5.6 and in Fig. 5.8, which will give us a better understanding on why the set of parameters

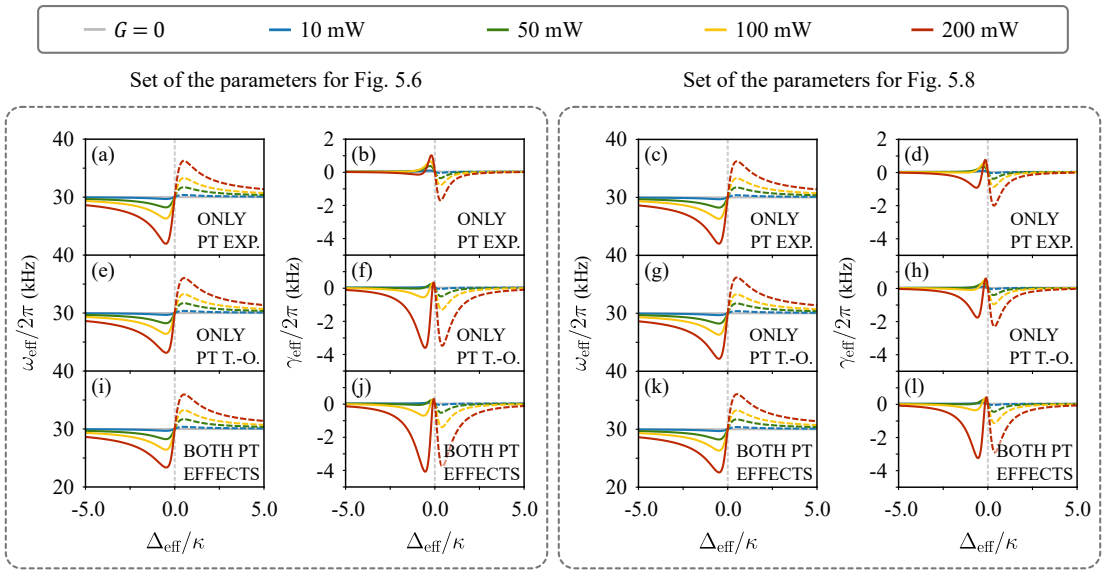

Figure 5.9: Numerical results of the oscillation frequencies and the damping rates of the optical resonator calculated by the refined model with different parameters of photothermal effects. (a)-(d) are the results simulated with only photothermal expansion ($\gamma_{\mathrm{re}} = \beta_{\mathrm{re}} = 0$), while (e)-(h) present the calculation with only thermo-optic effect ($\gamma_{\mathrm{ex}} = \beta_{\mathrm{ex}} = 0$). Simulation results of oscillation frequencies and the damping rates of the system as a function of the effective detuning with both photothermal expansion or thermo-optic effects are shown in (i)-(l). The nonzero parameters used in the refined model for the results in the left box are $\gamma_{\mathrm{ex}}/2\pi = 11\,\mathrm{Hz}$, $\beta_{\mathrm{ex}} = 120\,\mathrm{pm\,W^{-1}}$, $\gamma_{\mathrm{re}}/2\pi = 4000\,\mathrm{Hz}$, and $\beta_{\mathrm{re}} = -2\,\mathrm{pm\,W^{-1}}$. The simulation of the cavity response in time and frequency domains with the same parameters are shown in Fig. 5.6. In the right box, the nonzero parameters used for calculation are $\gamma_{\mathrm{ex}}/2\pi = 60\,\mathrm{Hz}$, $\beta_{\mathrm{ex}} = 40\,\mathrm{pm\,W^{-1}}$, $\gamma_{\mathrm{re}}/2\pi = 360\,\mathrm{Hz}$, and $\beta_{\mathrm{re}} = -10\,\mathrm{pm\,W^{-1}}$, which are the same parameters used for simulations in Fig. 5.8. The reference scenario with no optomechanical backaction ($G = 0$) is presented in solid light grey line. Optically unstable solutions are plotted in dashed lines, showing the inaccessible cases in steady state.

used in Fig. 5.8 gives a better simulation in high power regime even it gives a considerably worse simulation in the low power regime as discussed in the previous section.

The effective oscillation frequencies and the damping rates of the optical resonator are shown in Fig. 5.9. The numerical results of the oscillation frequencies and the damping rates of the optical resonator calculated by the refined model with parameters $\gamma_{\mathrm{ex}}/2\pi = 11\,\mathrm{Hz}$, $\beta_{\mathrm{ex}} = 120\,\mathrm{pm\,W^{-1}}$, $\gamma_{\mathrm{re}}/2\pi = 4000\,\mathrm{Hz}$, and $\beta_{\mathrm{re}} = -2\,\mathrm{pm\,W^{-1}}$ are shown in the left box. Figure 5.9(i) indicates that the frequency of the oscillation slowly increases as the scan goes closer to the resonance, which can also be seen in Fig. 5.6(c). And the simulation of the damping rates of the optical oscillator (see Fig. 5.9(j)) manifests amplification of the parametric oscillation during the scan. In the boxes on the right, with the same parameters used for simulations in Fig. 5.8(b)–(e), where $\gamma_{\mathrm{ex}}/2\pi = 60\,\mathrm{Hz}$, $\beta_{\mathrm{ex}} = 40\,\mathrm{pm\,W^{-1}}$, $\gamma_{\mathrm{re}}/2\pi = 360\,\mathrm{Hz}$, and $\beta_{\mathrm{re}} = -10\,\mathrm{pm\,W^{-1}}$, Fig. 5.9(k) and (l), respectively, show the oscillation frequencies and the damping rates of the optical resonator that are numerically calculated by the refined model. The difference between (i)–(j) and (k)–(l) can explain the difference between the simulations with different parameters. The increase in oscillation frequency

is more obvious in Fig. 5.8(d) than in Fig. 5.6(c). This feature is shown in the Fig. 5.9(i) and (k) as with the same effective detuning the parameters used for Fig. 5.8 give stronger modification of the oscillation frequency, shown in Fig. 5.9(k), than the parameters used for Fig. 5.6(c) (Fig. 5.9(i)). We also notice that the damping rate as a function of effective detuning is more negative in Fig. 5.9(j) comparing to that in Fig. 5.9(l), which results in a stronger amplification of the amplitude of the oscillation in Fig. 5.6(a) and a slower buildup of the oscillation in Fig. 5.8(b).

For two different sets of parameters, shown in the left and right boxes, we present the numerical calculations of the cavity dynamics with only thermal expansion and only thermal-optic effects. Panels (a)–(d) in Fig. 5.9 are the results simulated with only photothermal expansion ($\gamma_{\mathrm{re}} = \beta_{\mathrm{re}} = 0$), while panels (e)–(h) present the calculation with only thermo-optic effect ($\gamma_{\mathrm{ex}} = \beta_{\mathrm{ex}} = 0$). Another interesting phenomenon to note in our calculations is that the combination of the two independent photothermal effects gives an enhanced modification of the damping rate of the system response but a diminished change in oscillation frequency.

5.5.3 Search for the most optimal parameters

To further highlight the limitations of the refined model with two independent photothermal effects, we explore the values of the parameters close to the ones that give a better simulation in high power regime (Fig. 5.8(b)) to see if we can find good fits in the low power regime. Figure 5.10 show the effectiveness of the simulation with different relaxation rates (γ_{ex} and γ_{re}) and susceptivity coefficients (β_{ex} and β_{re}) of photothermal expansion and thermo-optic effects. The effectiveness of the simulation is calculated by the squared error Er of the simulation with the expression 10^{-20Er}. The black dot in (a)–(d) gives the point where $\gamma_{\mathrm{ex}} = 2\pi \times 60\,\mathrm{Hz}$, $\beta_{\mathrm{ex}} = 40\,\mathrm{pm\,W^{-1}}$, $\gamma_{\mathrm{re}} = 2\pi \times 400\,\mathrm{Hz}$, and $\beta_{\mathrm{re}} = -10\,\mathrm{pm\,W^{-1}}$, which are close to parameters that are used in the simulation shown in Fig. 5.8(b). To search for a good fitting with refined model at lower power around these parameters, we run the simulations with γ_{ex} ranging from $2\pi \times 10$ to $2\pi \times 300\,\mathrm{Hz}$, γ_{re} ranging from $2\pi \times 100$ to $2\pi \times 1000\,\mathrm{Hz}$, β_{ex} ranging from 10 to $150\,\mathrm{pm\,W^{-1}}$, and β_{re} ranging from -30 to $10\,\mathrm{pm\,W^{-1}}$. (a)–(d) presents the effectiveness of the simulations with the refined model when $\gamma_{\mathrm{ex}} = 2\pi \times 60\,\mathrm{Hz}$, $\gamma_{\mathrm{re}} = 2\pi \times 400\,\mathrm{Hz}$, $\beta_{\mathrm{ex}} = 40\,\mathrm{pm\,W^{-1}}$ and $\beta_{\mathrm{re}} = -10\,\mathrm{pm\,W^{-1}}$ respectively. The color bar gives the effectiveness of the simulation, with the color changes from blue to yellow, the squared error of the simulation gets smaller and the effectiveness of the simulation goes from 0 to 1. The plots of the effectiveness indicate that with one parameter given and the other three changing, we can find many good fitting values. When $\gamma_{\mathrm{ex}} = 2\pi \times 60\,\mathrm{Hz}$, the best fittings in lower power regimes are mainly dependant on β_{ex} and β_{re}, as shown in Fig. 5.10(a). With β_{ex} fixed to $40\,\mathrm{pm\,W^{-1}}$, the best fittings are more dependent on γ_{ex} and β_{re} (Fig. 5.10(c)). With a given γ_{re} (Fig. 5.10(b)) or β_{re} (Fig. 5.10(d)), best fittings fall onto the points that depend on all the other three parameters. Based on the error analysis of simulations results in Fig. 5.10, however, we can not

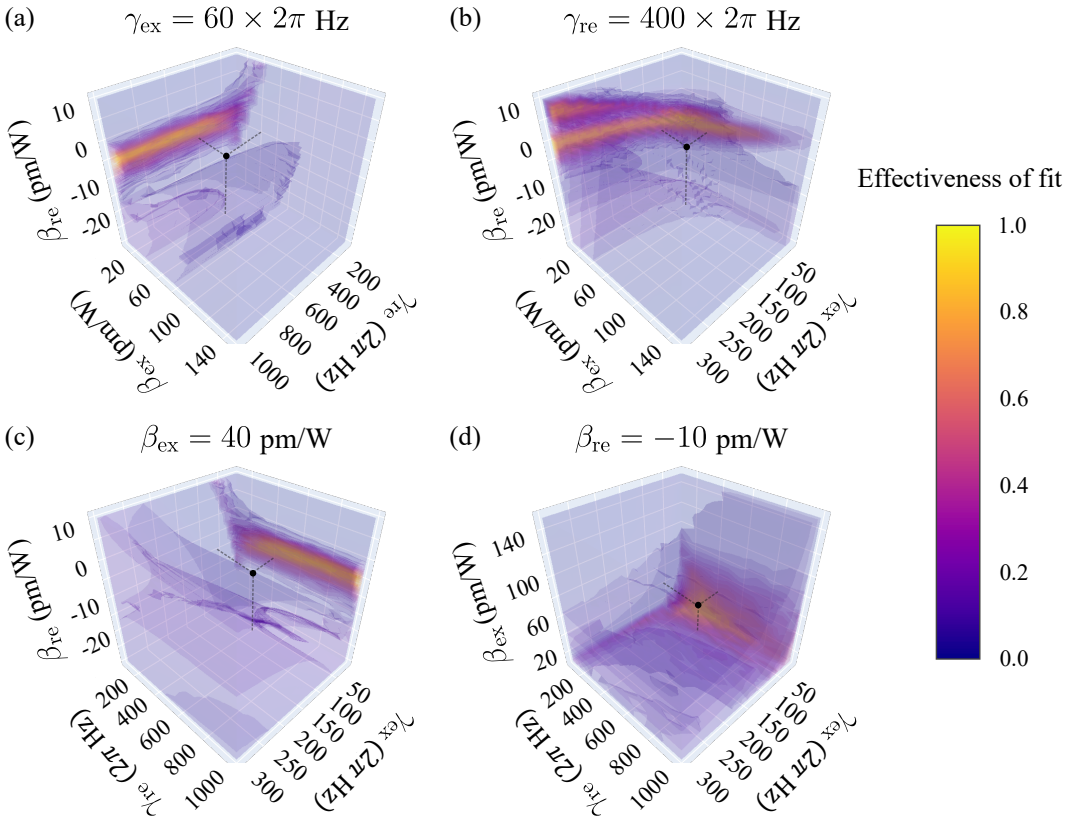

Figure 5.10: Effectiveness of simulation with 93 mW input power. (a)–(d) show the effectiveness of the simulation of the refined model with γ_{ex} range from $2\pi \times 10$ to $2\pi \times 300$ Hz, γ_{re} range from $2\pi \times 100$ to $2\pi \times 1000$ Hz, β_{ex} range from 10 to 150 pm W^{-1}, and β_{re} range from -30 to 10 pm W^{-1}. (a) gives the effectiveness of the simulations with $\gamma_{ex}/2\pi = 60$ Hz. (b) presents the effectiveness of the simulations with $\gamma_{re}/2\pi = 400$ Hz. (c) illustrates the effectiveness of the simulation when $\beta_{ex} = 40$ pm W^{-1}. The effectiveness of the simulation with the refined model when $\beta_{re} = -10$ pm W^{-1} is shown in (d). The effectiveness of the simulation is calculated by the squared error Er of the simulation with the expression 10^{-20Er}. The color bar gives the effectiveness of the simulation, with the color gets from blue to yellow, the squared error of the simulation gets smaller and the effectiveness of the simulation goes from 0 to 1. The black dots in (a)–(d) represent the point where $\gamma_{ex}/2\pi = 60$ Hz, $\beta_{ex} = 40$ pm W^{-1}, $\gamma_{re}/2\pi = 400$ Hz, and $\beta_{re} = -10$ pm W^{-1}, which are close to parameters that used in the simulation which gives the better results in high power regime, shown in Fig. 5.8(b). The cavity loss rate used in the simulation for lower power regime is $\kappa/2\pi = 658$ kHz.

find a good fitting in the low power regime close to the parameters used in Fig. 5.8(b). This indicates the imperfections of our model and implicates that the relaxation rates and susceptivity coefficients of photothermal effects may change with the input power, which suggests that more accurate simulation may require non-linear models for photothermal effects.

With discussions above, we show that by separating the photothermal expansion and the thermo-optic effects the refined model gives more reliable simulation results. Some smaller features of the simulation, such as the slowing buildup of the oscillation in the beginning of the scan, are still not perfectly matched to the experimental data. The parameters that can give good fitting in higher power regime fails in simulation of the cavity dynamics in lower power regime. This suggests a nonlinear correspondence between the photothermal effects and the intracavity power, leading to a further investigation of nonlinearity in photothermal effects.

5.6 Discussion on nonlinearity of photothermal effects

In this section, we will discuss the effect of adding a second order term into the photothermal effects in the model written as Eq. (5.15)-(5.20). One possible nonlinear model is for the thermal expansion and refractive index change of the coating materials to have a nonlinear temperature dependence [125]:

$$D_{\mathrm{I(II)}}(T) = \alpha^{(0)}_{\mathrm{exI(II)}} + \alpha^{(1)}_{\mathrm{exI(II)}} T + \alpha^{(2)}_{\mathrm{exI(II)}} T^2, \tag{5.27}$$

$$n(T) = \alpha^{(0)}_{\mathrm{re}} + \alpha^{(1)}_{\mathrm{re}} T + \alpha^{(2)}_{\mathrm{re}} T^2, \tag{5.28}$$

where constant parameters $\alpha^{(0)}_{\mathrm{ex}}$, $\alpha^{(1)}_{\mathrm{ex}}$ and $\alpha^{(2)}_{\mathrm{ex}}$ are the thermal expansion coefficients, and $\alpha^{(0)}_{\mathrm{re}}$, $\alpha^{(1)}_{\mathrm{re}}$, and $\alpha^{(2)}_{\mathrm{re}}$ are thermo-optic coefficients. n is the refractive index of the mirror materials that varies with the local temperature T. The thickness of part (I) (or (II)) of the coating of the top mirror (see Fig. 5.1(b)) is denoted as $D_{\mathrm{I(II)}}$. Thus, the susceptivity coefficients of photothermal expansion change to

$$\begin{aligned}
\mathcal{B}_{\mathrm{exI(II)}}(P_{\mathrm{opt}}) &= \frac{\partial D_{\mathrm{I(II)}}}{\partial P_{\mathrm{opt}}} P_{\mathrm{opt}} \\
&= \left(c_{\mathrm{I(II)}} \frac{\mathrm{d}D_{\mathrm{I(II)}}}{\mathrm{d}T} \frac{\mathrm{d}T}{\mathrm{d}P_{\mathrm{opt}}} \right) P_{\mathrm{opt}} \\
&= \left[c_{\mathrm{I(II)}} \left(\alpha^{(1)}_{\mathrm{exI(II)}} + 2\alpha^{(2)}_{\mathrm{exI(II)}} T(P_{\mathrm{opt}}) \right) \frac{\mathrm{d}T}{\mathrm{d}P_{\mathrm{opt}}} \right] P_{\mathrm{opt}} \\
&\approx c_{\mathrm{I(II)}} \alpha^{(1)}_{\mathrm{exI(II)}} \frac{\mathrm{d}T}{\mathrm{d}P_{\mathrm{opt}}} P_{\mathrm{opt}} + 2c_{\mathrm{I(II)}} \alpha^{(2)}_{\mathrm{exI(II)}} \left(\frac{\mathrm{d}T}{\mathrm{d}P_{\mathrm{opt}}} P_{\mathrm{opt}} \right)^2 \\
&= \beta^{(1)}_{\mathrm{exI(II)}} P_{\mathrm{opt}} + \beta^{(2)}_{\mathrm{exI(II)}} P^2_{\mathrm{opt}}.
\end{aligned} \tag{5.29}$$

Here, to simplify the deduction we use $c_{\mathrm{I}} = \eta_{\mathrm{ex}} (n_0 - n)$ and $c_{\mathrm{II}} = \eta_{\mathrm{ex}} n$ to replace the corresponding constants that are not of interest in Eq. (5.10). In the deduction, the

approximation $T(P_{\rm opt}) = (\mathrm{d}T/\mathrm{d}P_{\rm opt})\,P_{\rm opt}$ is applied. Similarly, because the two photothermal expansion terms share same relaxation rate $\gamma_{\rm ex}$, we can combine them into one term as

$$\begin{aligned}\mathcal{B}_{\rm ex}(P_{\rm opt}) &= \mathcal{B}_{\rm exI}(P_{\rm opt}) + \mathcal{B}_{\rm exII}(P_{\rm opt}) \\ &= \beta_{\rm ex,1}P_{\rm opt} + \beta_{\rm ex,2}P_{\rm opt}^2, \end{aligned} \tag{5.30}$$

where $\beta_{\rm ex,1} = \beta_{\rm exI}^{(1)} + \beta_{\rm exII}^{(1)}$ and $\beta_{\rm ex,2} = \beta_{\rm exI}^{(2)} + \beta_{\rm exII}^{(2)}$. The time derivative of the displacement of photothermal expansion effect hence reads

$$\begin{aligned}\dot{x}_{\rm ex} &= -\gamma_{\rm ex}\left[x_{\rm ex} + \mathcal{B}_{\rm ex}(P_{\rm opt})\right] \\ &= -\gamma_{\rm ex}\left(x_{\rm ex} + \beta_{\rm ex,1}P_{\rm opt} + \beta_{\rm ex,2}P_{\rm opt}^2\right). \end{aligned} \tag{5.31}$$

Similarly, we can write the time derivative of the displacement of thermo-optic effect:

$$\begin{aligned}\mathcal{B}_{\rm re}(P_{\rm opt}) &= \frac{\partial n}{\partial T}P_{\rm opt} \\ &= \eta_{\rm re}D_{\rm I}\frac{\mathrm{d}n}{\mathrm{d}T}\frac{\mathrm{d}T}{\mathrm{d}P_{\rm opt}}P_{\rm opt} \\ &= \eta_{\rm re}D_{\rm I}\left(\alpha_{\rm re}^{(1)} + 2\alpha_{\rm re}^{(2)}T(P_{\rm opt})\right)\frac{\mathrm{d}T}{\mathrm{d}P_{\rm opt}}P_{\rm opt} \\ &\approx \eta_{\rm re}D_{\rm I}\alpha_{\rm re}^{(1)}\frac{\mathrm{d}T}{\mathrm{d}P_{\rm opt}}P_{\rm opt} + 2\eta_{\rm re}D_{\rm I}\alpha_{\rm re}^{(2)}\left(\frac{\mathrm{d}T}{\mathrm{d}P_{\rm opt}}P_{\rm opt}\right)^2 \\ &= \beta_{\rm re,1}P_{\rm opt} + \beta_{\rm re,2}P_{\rm opt}^2. \end{aligned} \tag{5.32}$$

Thus, we have

$$\begin{aligned}\dot{x}_{\rm re} &= -\gamma_{\rm re}\left[x_{\rm re} - \mathcal{B}_{\rm re}(P_{\rm opt})\right] \\ &\approx -\gamma_{\rm re}\left(x_{\rm ex} - \beta_{\rm re,1}P_{\rm opt} - \beta_{\rm re,2}P_{\rm opt}^2\right). \end{aligned} \tag{5.33}$$

To simplify the simulation and only investigate the effect of adding a second order term to the photothermal susceptivity, we consider the model having only a single photothermal effect. The dynamic equations of motion thus are written as

$$\dot{a} = \left[-\kappa/2 + i(\Delta + G(x_{\rm th} + x_{\rm ac}))\right]a + \sqrt{\kappa_{\rm in}}a_{\rm in}, \tag{5.34}$$

$$\dot{a}^* = \left[-\kappa/2 - i(\Delta + G(x_{\rm th} + x_{\rm ac}))\right]a^* + \sqrt{\kappa_{\rm in}}a_{\rm in}^*, \tag{5.35}$$

$$\dot{x}_{\rm th} = -\gamma_{\rm th}(x_{\rm th} + \beta_{\rm th,1}P_{\rm opt}(a) + \beta_{\rm th,2}P_{\rm opt}^2(a)), \tag{5.36}$$

$$\dot{x}_{\rm ac} = p_{\rm ac}/m_{\rm ac}, \tag{5.37}$$

$$\dot{p}_{\rm ac} = -\gamma_{\rm ac}p_{\rm ac} - m_{\rm ac}\omega_{\rm ac}^2 x_{\rm ac} + \hbar G|a|^2. \tag{5.38}$$

Where $\beta_{\rm th,1}$ and $\beta_{\rm th,2}$ denote the first and second-order susceptivity coefficients of the joint photothermal effect. An example simulated by this model with an input power of 1.9 W is shown in Fig. 5.11(e). With this model, we can extend the oscillation duration in the

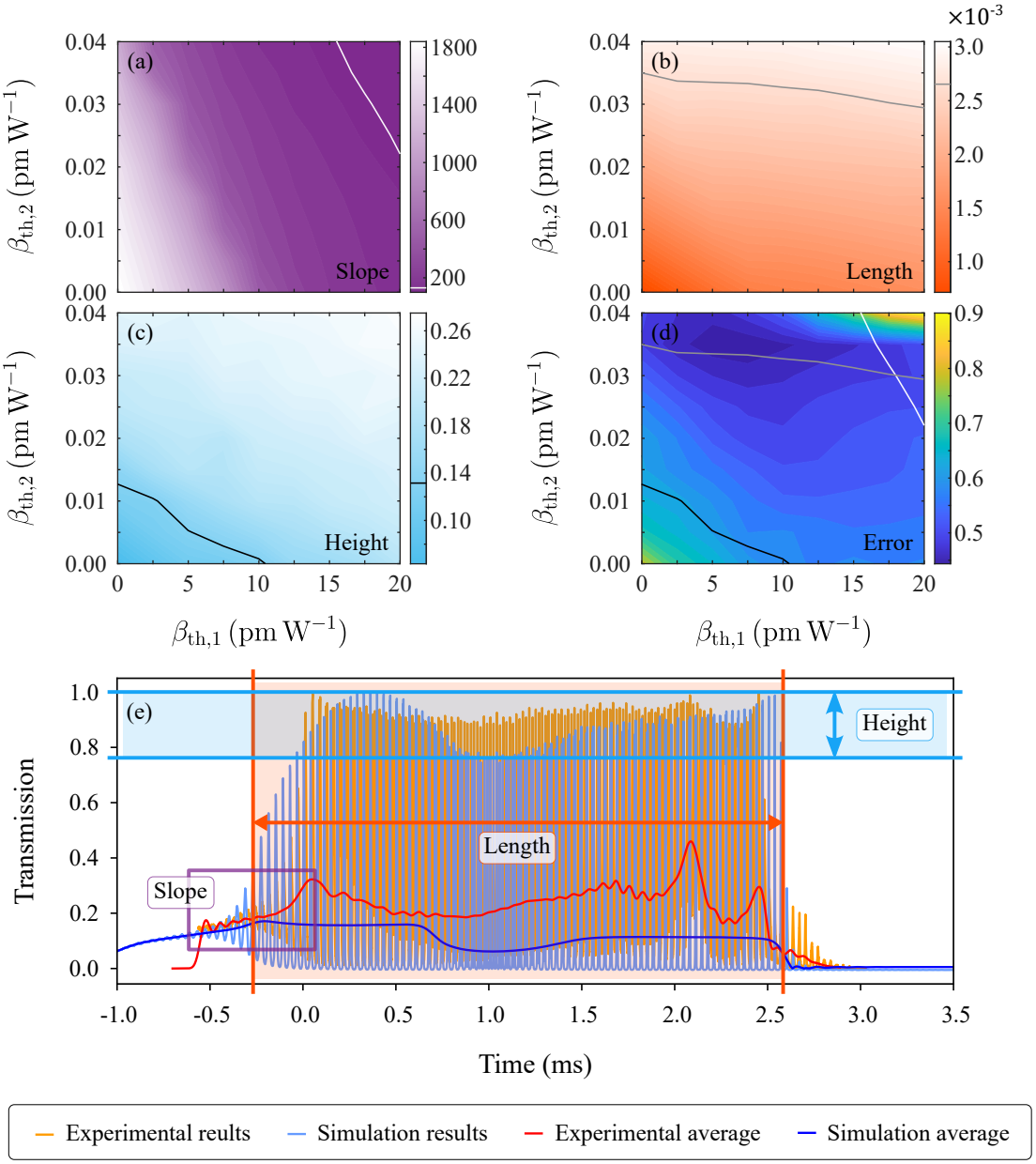

Figure 5.11: Analysis of the effectiveness of the model with joint nonlinear photothermal effect in higher power regime. (a)–(d) show the different methods to measure the difference between the simulation and experimental data (presented in (e)) as a function of the two photothermal susceptivities. (e) Comparison of simulation (light blue) and experimental (orange) results and their average, calculated by the low-pass Butterworth filter. (a) Average slope of ramping up of intensity during the self-locking phase, before parametric gain amplifies the oscillations to cross over the opposite side of the resonance, which gives strength of the amplification in parametric oscillation. Color bar from purple to white refers to an increasing slope. The white line is the slope of the experimental data (131.12 s^{-1}), included for reference. (b) Oscillation duration (length) of the simulation, where the color bar goes from coral to white with increasing length of oscillation. The grey line presents the value of the oscillation length of experimental data, 2.65 ms. The variation of the maximum of the peaks in the simulated oscillations (height) correspond to different $\beta_{th,1}$ and $\beta_{th,2}$, which are shown in (c). The calculated values of the variation from small to large are shown by sky blue to white in the color bar. The black curve gives the variation of 13.2% calculated from the experimental data. (d) Squared error of the averaged transmission. Other parameters used in the simulations are $P_{in} = 1.9$ W, $\kappa/2\pi = 735$ kHz, $v_{scan} = 1.86\,\mu$m s^{-1} and $\gamma_{th}/2\pi = 216$ Hz. In (e), we use $\beta_{th,1} = 7.5$ pm W^{-1} and $\beta_{th,2} = 0.035$ pm W^{-1}.

transmission during a down-ward scan, however, it also changes the shape of the cavity responses. The normalised experimental and simulated transmissions are presented in orange and light blue respectively. The average intensity of the transmission in experiment (red) and simulation (dark blue) calculated with the low-pass Butterworth filter are also shown. In the plot, it is clear that adding the nonlinear dependence of intracavity power into the photothermal effect term changes the simulation.

In order to quantify the effectiveness of the simulation, we calculate four quantities of the simulation and compare them to that of the experimental data. First, we investigate the slope of the initial part of the averaged transmission, which is given by the expression

$$slope = \frac{0.2 - 0.05}{t\{I = 0.2\} - t\{I = 0.05\}}, \tag{5.39}$$

where $t\{I = i\}$ is the time when the average intensity of the normalised transmission $I = i$. This gives the strength of the amplification in parametric oscillation, and a larger slope manifests as stronger amplification. In experimental results, the slope is $131.12\,\mathrm{s}^{-1}$. The slopes calculated from the simulation results with different $\beta_{\mathrm{th},1}$ and $\beta_{\mathrm{th},2}$ are shown in Fig. 5.11(a). The color bar from purple to white refers to the calculated slope from small to large, i.e., the strength of the amplification from small to large. The white contour in the plot is the calculated slope of the experimental data used as a reference to investigate the effectiveness of the simulation.

The second quantity that we use to measure the effectiveness is the oscillation duration (length) of the simulation, which is shown in Fig. 5.11(b). It is calculated by

$$length = t\{I = 0.05, end\} - t\{I = 0.1, start\}, \tag{5.40}$$

where $t\{I = 0.05, end\}$ is the time when the average intensity of the normalised transmission equals 0.05 in the last 1/4 of the oscillation, while $t\{I = 0.1, begin\}$ is the first time when the average intensity of the normalised transmission crossing 0.01 in the 1/4 of the oscillation. The color bar of the plot shows the oscillation duration obtained from simulation, going from coral to white with increasing length of oscillation. The contour line (grey) corresponds to 2.65 ms, presenting the value of the oscillation length of experimental data.

In Fig. 5.11(c), we show the third quantity, the variation of the maximum of the peaks in the oscillation:

$$height = 1 - \min\{peaks\}. \tag{5.41}$$

Note that in the simulations, we plot the normalised transmission intensity, normalised to the intensity on resonance. The smallest peak values of the oscillation is denoted by $\min\{peaks\}$. The calculated values of *height* from small to large are shown by sky blue to white in the color bar, where the black curve gives the variation of 0.13 calculated from the experimental data.

The last quantity we investigate is the squared error of the simulated average intensity of transmission, shown in Fig. 5.11(d), with smaller error, the color goes from yellow to blue. We also plot the curves with the values of $\beta_{\mathrm{th},1}$ and $\beta_{\mathrm{th},2}$ giving smallest errors of *slope*, *length* and *height* in white, grey and black. Note that other quantities could also defined to measure the effectiveness of the simulation. For example, the 'curvature' of the peaks at the beginning of the oscillations is very sharp for the experiment and very rounded for the simulation.

From the error analysis of the four quantities, it is clear that the slope of the beginning part of the averaged transmission is more dependent on the first order photothermal susceptivity $\beta_{\mathrm{th},1}$ (Fig. 5.11(a)). Larger $\beta_{\mathrm{th},1}$ and $\beta_{\mathrm{th},2}$ gives smaller values of the slope. The oscillation duration (Fig. 5.11(b)), however, is more dependant on the second order photothermal susceptivity $\beta_{\mathrm{th},2}$ when $\beta_{\mathrm{th},1}$ is big. With larger $\beta_{\mathrm{th},2}$, the oscillation duration gets longer. When $\beta_{\mathrm{th},1}$ and $\beta_{\mathrm{th},2}$ are both relatively small, the length depends on both first and second order photothermal susceptivity. The variation of the maximum of the peaks, shown in Fig. 5.11(c), is dependent on both $\beta_{\mathrm{th},1}$ and $\beta_{\mathrm{th},2}$. The squared error of the simulated average transmission (Fig. 5.11(d)) has similar dependence on $\beta_{\mathrm{th},1}$ and $\beta_{\mathrm{th},2}$ as the error of *length* of the simulation, that is because when the oscillation duration is too short or too long, the error calculated from the averaged curves becomes bigger compare to the errors induced by an inaccurate *slope* or *height*. Moreover, the best fits of $\beta_{\mathrm{th},1}$ and $\beta_{\mathrm{th},2}$ for *slope* (white line), *length* (grey line) and *height* (black line) in Fig. 5.11(d) are not overlapping. This indicates that adding the second order photothermal susceptivity in the model with only joint photothermal as nonlinearity is still not effective for simulating the cavity dynamics in high power.

5.7 Conclusion

In this chapter, we have presented the simulation of the heat transfer and the optical intensity in the mirror coating of our levitation system. With this, we separate the photothermal effects into two different independent components — photothermal expansion and thermo-optic effects. We gave detailed deduction of them and added them into the dynamic equations of motion. With this new model that has two different photothermal displacements, we present refined predictions that provide quantitative as well as qualitative agreement with the experimental result.

We also provided a discussion on the effectiveness of different models. The model with joint photothermal effect can give good fitting in lower power regime but fails to fit the experimental data at higher power when the parametric oscillation occurs. Adding nonlinearity into this model can extend the oscillation duration to the level that matches the experimental results. However, it changes other features of the simulated cavity response, hence can not give a reliable simulation either. With two photothermal effects, the model gives simulations at both lower or higher power that are consistent with the experiments.

Even though some small features of the cavity response are not well fitted, we have proved the necessity of separating the photothermal effects in the model.

With the detailed analysis and discussion, we have concluded that two photothermal effects are necessary in the model for simulating the dynamics of our optomechanical levitation system, especially in high power regime when different photothermal effects compete each other. The model with only a single photothermal effect is sufficient in the regime where one photothermal effect is dominated over the others or different photothermal effects share the same relaxation rate. The nonlinear correction in this single-photothermal-effect model doesn't show same advantages as the two-photothermal-effect linear model, instead adds unnecessary complexity and more fit parameters. Further investigations will consider nonlinearity of the two independent photothermal effects caused by other effects, such as the mode shift in the cavity, the bolometric interaction and photoacoustic effect.

Chapter 6

Conclusion and Future Work

This thesis explored photothermal nonlinearity in a linear optomechanical levitation system. A new model with two photothermal effects is theoretically presented to better simulate and understand the levitation system. A useful technique to achieve cancellation of photothermally induced instability in the system is also introduced. However, in order to reach the goal of stable optical levitation, more in-depth investigation in the causes and the consequences of photothermal effects in the levitation system is needed. Other possible proposals of the material and design of the levitation mirror are also worth of consideration.

6.1 Novel photothermally induced effects

In Chapter 5, we have given in-depth investigation and discussion of two photothermal effects — photothermal expansion and thermo-optic effects. These two effects are not only vital in the levitation system studied in this thesis, but also of interest to other similar optomechanical systems where high-intensity laser is used or high precision of the measurement is desired. However, there are still more novel photothermally induced effects yet waiting to be explored.

Theory of the possible photothermal effects and photothermally induced dynamics will be studied in the future, such as

1. the mode shift in the cavity due to the shape change of the mirror resulting from its local and unequal expansion,
2. the distortion of the mirror surface from the temperature gradients,
3. the bolometric interaction directly coupling photothermal absorption to the acoustic mode,
4. the dependence of cavity decay rate and input coupling rate on either acoustic or photothermal displacements.

Experimentally, another probe laser path will be set up and sent into the cavity for investigating the cavity evolution with the pump beam, which offers a way to monitor the

cavity response to the mechanical and photothermal interaction.

6.2 Stable optical levitation

Based on the technique presented in Chapter 4, inserting window into the cavity to modify the susceptivity coefficients of photothermal effects is a promising way to achieve cancellation of photothermally induced instability in our linear optical levitation system. Thus, more experiments on the cancellation of photothermally induced parametric amplification using inserted window with different materials or designs will also be conducted.

Another possible path to achieve optical levitation is using nano-structure in the levitation mirror [126]. With well designed structure, the laser shone onto the mirror can have diffracted beams to any wanted direction, even 90°. This suggests a new way to trap the mirror horizontally by only using the scattering light. Another advantage of a levitation mirror with nano-structure is its much lighter weight. Instead of using dielectric mirror coating acting as the Bragg reflector to achieve extremely high reflectivity, using a single grating can also achieve almost 100% reflectivity, with around 1/10 to 1/100 weight of the mirror we have now. Other proposals that may generate new optical levitation configurations, such as using two-dimensional materials as the levitation mirror, are also interesting to be explored.

Bibliography

[1] Markus Aspelmeyer, Tobias J Kippenberg, and Florian Marquardt. "Cavity optomechanics". In: *Reviews of Modern Physics* 86.4 (2014), p. 1391.

[2] James Clerk Maxwell. *A treatise on electricity and magnetism*. Vol. 1. Clarendon press, 1873.

[3] P Lebedev. "Experimental examination of light pressure". In: *Nuovo Cimento* 15.195 (1883), p. 195.

[4] Ernest Fox Nichols and Gordon Ferrie Hull. "A preliminary communication on the pressure of heat and light radiation". In: *Physical Review (Series I)* 13.5 (1901), p. 307.

[5] Arthur Ashkin. "Trapping of atoms by resonance radiation pressure". In: *Physical Review Letters* 40.12 (1978), p. 729.

[6] Arthur Ashkin. "Optical trapping and manipulation of neutral particles using lasers". In: *Proceedings of the National Academy of Sciences* 94.10 (1997), pp. 4853–4860.

[7] John Prodan et al. "Stopping atoms with laser light". In: *Physical review letters* 54.10 (1985), p. 992.

[8] Theodor W Hänsch and Arthur L Schawlow. "Cooling of gases by laser radiation". In: *Optics Communications* 13.1 (1975), pp. 68–69.

[9] DJ Wineland and HG Dehmelt. "Principles of the stored ion calorimeter". In: *Journal of Applied Physics* 46.2 (1975), pp. 919–930.

[10] Steven Chu et al. "Three-dimensional viscous confinement and cooling of atoms by resonance radiation pressure". In: *Physical review letters* 55.1 (1985), p. 48.

[11] Arthur Ashkin. "Applications of laser radiation pressure". In: *Science* 210.4474 (1980), pp. 1081–1088.

[12] Arthur Ashkin and JM Dziedzic. "Optical levitation in high vacuum". In: *Applied Physics Letters* 28.6 (1976), pp. 333–335.

[13] Arthur Ashkin and JM Dziedzic. "Feedback stabilization of optically levitated particles". In: *Applied Physics Letters* 30.4 (1977), pp. 202–204.

[14] Arthur Ashkin. "Atomic-beam deflection by resonance-radiation pressure". In: *Physical Review Letters* 25.19 (1970), p. 1321.

[15] Arthur Ashkin. "Acceleration and trapping of particles by radiation pressure". In: *Physical review letters* 24.4 (1970), p. 156.

[16] Arthur Ashkin and JM Dziedzic. "Optical levitation by radiation pressure". In: *Applied Physics Letters* 19.8 (1971), pp. 283–285.

[17] A Ashkin and JM Dziedzic. "Optical levitation of liquid drops by radiation pressure". In: *Science* 187.4181 (1975), pp. 1073–1075.

[18] Immanuel Bloch, Jean Dalibard, and Wilhelm Zwerger. "Many-body physics with ultracold gases". In: *Reviews of modern physics* 80.3 (2008), p. 885.

[19] Rebecca J Hopkins et al. "Control and characterisation of a single aerosol droplet in a single-beam gradient-force optical trap". In: *Physical Chemistry Chemical Physics* 6.21 (2004), pp. 4924–4927.

[20] Arthur Ashkin and JM Dziedzic. "Observation of light scattering from nonspherical particles using optical levitation". In: *Applied Optics* 19.5 (1980), pp. 660–668.

[21] Arthur Ashkin. "History of optical trapping and manipulation of small-neutral particle, atoms, and molecules". In: *IEEE Journal of Selected Topics in Quantum Electronics* 6.6 (2000), pp. 841–856.

[22] Vladan Vuletić and Steven Chu. "Laser cooling of atoms, ions, or molecules by coherent scattering". In: *Physical Review Letters* 84.17 (2000), p. 3787.

[23] NY Misconi. "On the rotational bursting of interplanetary dust particles". In: *Geophysical Research Letters* 3.10 (1976), pp. 585–588.

[24] Anthony F Bernhardt. "Isotope separation by laser deflection of an atomic beam". In: *Applied physics* 9.1 (1976), pp. 19–34.

[25] Po Jacquinot et al. "High resolution spectroscopic application of atomic beam deflection by resonant light". In: *Optics Communications* 8.2 (1973), pp. 163–165.

[26] JE Bjorkholm et al. "Observation of focusing of neutral atoms by the dipole forces of resonance-radiation pressure". In: *Physical review letters* 41.20 (1978), p. 1361.

[27] John E Bjorkholm et al. "Experimental observation of the influence of the quantum fluctuations of resonance-radiation pressure". In: *Optics letters* 5.3 (1980), pp. 111–113.

[28] Peter Hess and AC Boccara. *Photoacoustic, photothermal and photochemical processes at surfaces and in thin films*. Springer, 1989.

[29] Warren B Jackson et al. "Photothermal deflection spectroscopy and detection". In: *Applied optics* 20.8 (1981), pp. 1333–1344.

[30] M Bertolotti et al. "Analysis of the photothermal deflection technique in the surface reflection scheme: Theory and experiment". In: *Journal of Applied Physics* 83.2 (1998), pp. 966–982.

[31] Delong Zhang et al. "Depth-resolved mid-infrared photothermal imaging of living cells and organisms with submicrometer spatial resolution". In: *Science advances* 2.9 (2016), e1600521.

[32] Robert Furstenberg et al. "Chemical imaging using infrared photothermal microspectroscopy". In: *Next-Generation Spectroscopic Technologies V*. Vol. 8374. SPIE. 2012, pp. 293–302.

[33] Michel Pinard and Aurélien Dantan. "Quantum limits of photothermal and radiation pressure cooling of a movable mirror". In: *New Journal of Physics* 10.9 (2008), p. 095012.

[34] Liu Qiu et al. "Dissipative Quantum Feedback in Measurements Using a Parametrically Coupled Microcavity". In: *Prx Quantum* 3.2 (2022), p. 020309.

[35] Chunnong Zhao et al. "Compensation of strong thermal lensing in high-optical-power cavities". In: *Physical review letters* 96.23 (2006), p. 231101.

[36] M Afrin Badhan et al. "Analyzing elastic deformation of test masses in LIGO". In: *LIGO Document Control Center, T09004010-v1* (2009).

[37] VB Braginsky, ML Gorodetsky, and SP Vyatchanin. "Thermodynamical fluctuations and photo-thermal shot noise in gravitational wave antennae". In: *Physics letters A* 264.1 (1999), pp. 1–10.

[38] M De Rosa et al. "Experimental measurement of the dynamic photothermal effect in Fabry-Perot cavities for gravitational wave detectors". In: *Physical review letters* 89.23 (2002), p. 237402.

[39] Matthew Evans et al. "Observation of parametric instability in Advanced LIGO". In: *Physical review letters* 114.16 (2015), p. 161102.

[40] Jinyong Ma et al. "Observation of nonlinear dynamics in an optical levitation system". In: *Communications Physics* 3.1 (2020), pp. 1–10.

[41] VB Braginski¨, Anatoli B Manukin, and M Yu Tikhonov. "Investigation of dissipative ponderomotive effects of electromagnetic radiation". In: *Soviet Journal of Experimental and Theoretical Physics* 31 (1970), p. 829.

[42] VB Braginski and AB Manukin. "Ponderomotive effects of electromagnetic radiation". In: *Sov. Phys. JETP* 25.4 (1967), pp. 653–655.

[43] BD Cuthbertson et al. "Parametric back-action effects in a high-Q cyrogenic sapphire transducer". In: *Review of Scientific Instruments* 67.7 (1996), pp. 2435–2442.

[44] A Dorsel et al. "Optical bistability and mirror confinement induced by radiation pressure". In: *Physical Review Letters* 51.17 (1983), p. 1550.

[45] VB Braginsky, SE Strigin, and S Pr Vyatchanin. "Parametric oscillatory instability in Fabry–Perot interferometer". In: *Physics Letters A* 287.5-6 (2001), pp. 331–338.

[46] Benjamin P Abbott et al. "GW150914: The Advanced LIGO detectors in the era of first discoveries". In: *Physical review letters* 116.13 (2016), p. 131103.

[47] Yuxiang Liu et al. "Wide cantilever stiffness range cavity optomechanical sensors for atomic force microscopy". In: *Optics express* 20.16 (2012), pp. 18268–18280.

[48] John D Teufel et al. “Sideband cooling of micromechanical motion to the quantum ground state”. In: *Nature* 475.7356 (2011), pp. 359–363.

[49] Jean-Michel Courty, Antoine Heidmann, and Michel Pinard. “Quantum locking of mirrors in interferometers”. In: *Physical review letters* 90.8 (2003), p. 083601.

[50] Olivier Arcizet et al. “Beating quantum limits in an optomechanical sensor by cavity detuning”. In: *Physical Review A* 73.3 (2006), p. 033819.

[51] William Marshall et al. “Towards quantum superpositions of a mirror”. In: *Physical Review Letters* 91.13 (2003), p. 130401.

[52] Olivier Arcizet et al. “High-sensitivity optical monitoring of a micromechanical resonator with a quantum-limited optomechanical sensor”. In: *Physical review letters* 97.13 (2006), p. 133601.

[53] Tobias J Kippenberg and Kerry J Vahala. “Cavity opto-mechanics”. In: *Optics express* 15.25 (2007), pp. 17172–17205.

[54] Dustin Kleckner and Dirk Bouwmeester. “Sub-kelvin optical cooling of a micromechanical resonator”. In: *Nature* 444.7115 (2006), pp. 75–78.

[55] CM Mow-Lowry et al. “Cooling of a gram-scale cantilever flexure to 70 mK with a servo-modified optical spring”. In: *Physical review letters* 100.1 (2008), p. 010801.

[56] Olivier Arcizet et al. “Radiation-pressure cooling and optomechanical instability of a micromirror”. In: *Nature* 444.7115 (2006), pp. 71–74.

[57] Schwab Gigan et al. “Self-cooling of a micromirror by radiation pressure”. In: *Nature* 444.7115 (2006), pp. 67–70.

[58] TJ Kippenberg et al. “Analysis of radiation-pressure induced mechanical oscillation of an optical microcavity”. In: *Physical Review Letters* 95.3 (2005), p. 033901.

[59] Albert Schliesser et al. “Radiation pressure cooling of a micromechanical oscillator using dynamical backaction”. In: *Physical Review Letters* 97.24 (2006), p. 243905.

[60] JD Thompson et al. “Strong dispersive coupling of a high-finesse cavity to a micromechanical membrane”. In: *Nature* 452.7183 (2008), pp. 72–75.

[61] Thomas Corbitt et al. “An all-optical trap for a gram-scale mirror”. In: *Physical review letters* 98.15 (2007), p. 150802.

[62] Benjamin S Sheard et al. “Observation and characterization of an optical spring”. In: *Physical Review A* 69.5 (2004), p. 051801.

[63] PA Altin et al. “A robust single-beam optical trap for a gram-scale mechanical oscillator”. In: *Scientific Reports* 7.1 (2017), pp. 1–8.

[64] Jasper Chan et al. “Laser cooling of a nanomechanical oscillator into its quantum ground state”. In: *Nature* 478.7367 (2011), pp. 89–92.

[65] Jan Harms et al. “Squeezed-input, optical-spring, signal-recycled gravitational-wave detectors”. In: *Physical Review D* 68.4 (2003), p. 042001.

[66] Swati Singh et al. "All-optical optomechanics: an optical spring mirror". In: *Physical review letters* 105.21 (2010), p. 213602.

[67] Giovanni Guccione et al. "Scattering-free optical levitation of a cavity mirror". In: *Physical Review Letters* 111.18 (2013), p. 183001.

[68] MJ Collett and CW Gardiner. "Squeezing of intracavity and traveling-wave light fields produced in parametric amplification". In: *Physical Review A* 30.3 (1984), p. 1386.

[69] CW Gardiner and CM Savage. "A multimode quantum theory of a degenerate parametric amplifier in a cavity". In: *Optics communications* 50.3 (1984), pp. 173–178.

[70] Crispin Gardiner, Peter Zoller, and Peter Zoller. *Quantum noise: a handbook of Markovian and non-Markovian quantum stochastic methods with applications to quantum optics*. Springer Science & Business Media, 2004.

[71] Paul R Yoder Jr. *Opto-mechanical systems design*. CRC press, 2005.

[72] F Marino, M De Rosa, and F Marin. "Canard orbits in Fabry-Perot cavities induced by radiation pressure and photothermal effects". In: *Physical Review E* 73.2 (2006), p. 026217.

[73] Grover A Swartzlander et al. "Stable optical lift". In: *Nature Photonics* 5.1 (2011), pp. 48–51.

[74] Onofrio M Maragò et al. "Optical trapping and manipulation of nanostructures". In: *Nature nanotechnology* 8.11 (2013), pp. 807–819.

[75] Levi P Neukirch et al. "Multi-dimensional single-spin nano-optomechanics with a levitated nanodiamond". In: *Nature Photonics* 9.10 (2015), pp. 653–657.

[76] ATM Rahman and PF Barker. "Laser refrigeration, alignment and rotation of levitated Yb3+: YLF nanocrystals". In: *Nature Photonics* 11.10 (2017), pp. 634–638.

[77] Chris Timberlake et al. "Acceleration sensing with magnetically levitated oscillators above a superconductor". In: *Applied Physics Letters* 115.22 (2019), p. 224101.

[78] Erik Hebestreit et al. "Sensing static forces with free-falling nanoparticles". In: *Physical review letters* 121.6 (2018), p. 063602.

[79] Fernando Monteiro et al. "Optical levitation of 10-ng spheres with nano-g acceleration sensitivity". In: *Physical Review A* 96.6 (2017), p. 063841.

[80] Fernando Monteiro et al. "Force and acceleration sensing with optically levitated nanogram masses at microkelvin temperatures". In: *Physical Review A* 101.5 (2020), p. 053835.

[81] Bradley R Slezak et al. "Cooling the motion of a silica microsphere in a magneto-gravitational trap in ultra-high vacuum". In: *New Journal of Physics* 20.6 (2018), p. 063028.

[82] David C Moore, Alexander D Rider, and Giorgio Gratta. "Search for millicharged particles using optically levitated microspheres". In: *Physical review letters* 113.25 (2014), p. 251801.

[83] Gambhir Ranjit et al. "Zeptonewton force sensing with nanospheres in an optical lattice". In: *Physical Review A* 93.5 (2016), p. 053801.

[84] Martin Frimmer et al. "Controlling the net charge on a nanoparticle optically levitated in vacuum". In: *Physical Review A* 95.6 (2017), p. 061801.

[85] Francesco Ricci et al. "Accurate mass measurement of a levitated nanomechanical resonator for precision force-sensing". In: *Nano letters* 19.10 (2019), pp. 6711–6715.

[86] Thai M Hoang et al. "Torsional optomechanics of a levitated nonspherical nanoparticle". In: *Physical review letters* 117.12 (2016), p. 123604.

[87] Derek F Jackson Kimball, Alexander O Sushkov, and Dmitry Budker. "Precessing ferromagnetic needle magnetometer". In: *Physical review letters* 116.19 (2016), p. 190801.

[88] Tobias Westphal et al. "Measurement of gravitational coupling between millimetre-sized masses". In: *Nature* 591.7849 (2021), pp. 225–228.

[89] Felix Tebbenjohanns et al. "Quantum control of a nanoparticle optically levitated in cryogenic free space". In: *Nature* 595.7867 (2021), pp. 378–382.

[90] Lorenzo Magrini et al. "Real-time optimal quantum control of mechanical motion at room temperature". In: *Nature* 595.7867 (2021), pp. 373–377.

[91] Felix Tebbenjohanns et al. "Motional sideband asymmetry of a nanoparticle optically levitated in free space". In: *Physical Review Letters* 124.1 (2020), p. 013603.

[92] Nikolai Kiesel et al. "Cavity cooling of an optically levitated submicron particle". In: *Proceedings of the National Academy of Sciences* 110.35 (2013), pp. 14180–14185.

[93] J Millen et al. "Cavity cooling a single charged levitated nanosphere". In: *Physical review letters* 114.12 (2015), p. 123602.

[94] Nadine Meyer et al. "Resolved-sideband cooling of a levitated nanoparticle in the presence of laser phase noise". In: *Physical review letters* 123.15 (2019), p. 153601.

[95] M Serlin et al. "Intrinsic quantized anomalous Hall effect in a moiré heterostructure". In: *Science* 367.6480 (2020), pp. 900–903.

[96] Yoshihiko Arita et al. "Dynamics of a levitated microparticle in vacuum trapped by a perfect vortex beam: three-dimensional motion around a complex optical potential". In: *JOSA B* 34.6 (2017), pp. C14–C19.

[97] Loıc Rondin et al. "Direct measurement of Kramers turnover with a levitated nanoparticle". In: *Nature nanotechnology* 12.12 (2017), pp. 1130–1133.

[98] Francesco Ricci et al. "Optically levitated nanoparticle as a model system for stochastic bistable dynamics". In: *Nature communications* 8.1 (2017), pp. 1–7.

[99] TM Ostermayr et al. "A transportable Paul-trap for levitation and accurate positioning of micron-scale particles in vacuum for laser-plasma experiments". In: *Review of Scientific Instruments* 89.1 (2018), p. 013302.

[100] O Brzobohatỳ et al. "Experimental demonstration of optical transport, sorting and self-arrangement using a ¡®tractor beam¡¯". In: *Nature Photonics* 7.2 (2013), pp. 123–127.

[101] Tomáš Čižmár et al. "Optical conveyor belt for delivery of submicron objects". In: *Applied Physics Letters* 86.17 (2005), p. 174101.

[102] Muddassar Rashid et al. "Precession motion in levitated optomechanics". In: *Physical review letters* 121.25 (2018), p. 253601.

[103] Fernando Monteiro et al. "Optical rotation of levitated spheres in high vacuum". In: *Physical Review A* 97.5 (2018), p. 051802.

[104] Yoshihiko Arita, Michael Mazilu, and Kishan Dholakia. "Laser-induced rotation and cooling of a trapped microgyroscope in vacuum". In: *Nature communications* 4.1 (2013), pp. 1–7.

[105] Stefan Kuhn et al. "Full rotational control of levitated silicon nanorods". In: *Optica* 4.3 (2017), pp. 356–360.

[106] C Gonzalez-Ballestero et al. "Levitodynamics: Levitation and control of microscopic objects in vacuum". In: *Science* 374.6564 (2021), eabg3027.

[107] Charles P Blakemore et al. "Search for non-Newtonian interactions at micrometer scale with a levitated test mass". In: *Physical Review D* 104.6 (2021), p. L061101.

[108] J Millen et al. "Nanoscale temperature measurements using non-equilibrium Brownian dynamics of a levitated nanosphere". In: *Nature nanotechnology* 9.6 (2014), pp. 425–429.

[109] Tongcang Li et al. "Measurement of the instantaneous velocity of a Brownian particle". In: *Science* 328.5986 (2010), pp. 1673–1675.

[110] Jan Gieseler et al. "Nonlinear mode coupling and synchronization of a vacuum-trapped nanoparticle". In: *Physical review letters* 112.10 (2014), p. 103603.

[111] Benjamin A Stickler et al. "Probing macroscopic quantum superpositions with nanorotors". In: *New Journal of Physics* 20.12 (2018), p. 122001.

[112] James Bateman et al. "Near-field interferometry of a free-falling nanoparticle from a point-like source". In: *Nature communications* 5.1 (2014), pp. 1–5.

[113] Rainer Kaltenbaek et al. "Macroscopic quantum resonators (MAQRO)". In: *Experimental Astronomy* 34.2 (2012), pp. 123–164.

[114] Oriol Romero-Isart. "Quantum superposition of massive objects and collapse models". In: *Physical Review A* 84.5 (2011), p. 052121.

[115] Yuta Michimura and Kentaro Komori. "Quantum sensing with milligram scale optomechanical systems". In: *The European Physical Journal D* 74.6 (2020), pp. 1–14.

[116] Yuta Michimura et al. "Optical levitation of a mirror for reaching the standard quantum limit". In: *Optics express* 25.12 (2017), pp. 13799–13806.

[117] CC Gan, CM Savage, and SZ Scully. "Optomechanical tests of a Schrödinger-Newton equation for gravitational quantum mechanics". In: *Physical Review D* 93.12 (2016), p. 124049.

[118] Jinyong Ma. "Photothermal nonlinearity in optical cavities and optomechanical systems". PhD thesis. Research School of Physics, ANU College of Science, The Australian National University, 2020.

[119] SV Dhurandhar et al. "Stability of giant Fabry–Perot cavities of interferometric gravitational-wave detectors". In: *Applied optics* 36.22 (1997), pp. 5325–5334.

[120] Massimo Cerdonio et al. "Thermoelastic effects at low temperatures and quantum limits in displacement measurements". In: *Physical Review D* 63.8 (2001), p. 082003.

[121] Kumarasiri Konthasinghe et al. "Self-sustained photothermal oscillations in high-finesse Fabry-Perot microcavities". In: *Physical Review A* 95.1 (2017), p. 013826.

[122] Jiayi Qin et al. "Cancellation of photothermally induced instability in an optical resonator". In: *Optica* 9.8 (2022), pp. 924–932.

[123] M Evans et al. "Thermo-optic noise in coated mirrors for high-precision optical measurements". In: *Physical Review D* 78.10 (2008), p. 102003.

[124] Chakravarti V Madhusudana. "Thermal Constriction Resistance". In: *Thermal Contact Conductance*. Springer, 2014, pp. 9–23.

[125] Hongchun Gao et al. "Investigation on the thermo-optic coefficient of silica fiber within a wide temperature range". In: *Journal of Lightwave Technology* 36.24 (2018), pp. 5881–5886.

[126] Ognjen Ilic and Harry A Atwater. "Self-stabilizing photonic levitation and propulsion of nanostructured macroscopic objects". In: *Nature Photonics* 13.4 (2019), pp. 289–295.